Laboratory for Atmospheric and Space Physics

University of Colorado
Boulder, Colorado

Earth Observing System
SOlar Radiation and Climate Experiment
(EOS SORCE)

Algorithm Theoretical Basis Document
(Draft)

Document No. 20560-T6-0006   Date: April 4, 2000

Prepared by _____Christopher K. Pankratz_____ Date _____

Approved by _____ Date _____

Approved by _____ Date _____

Approved by _____ Date _____

Approved by _____ Date _____

Revisions				
Rev	Description of Change	By	Approved	Date
A	Add May 1999 ATBD Review Revisions. Add TIM Instrument	All		March 2000

Contents

List of Figures

List of Tables

1 Introduction

1.1 Purpose of this Document

This Algorithm Theoretical Basis Document (ATBD) describes the algorithms used to produce all data levels of solar total and spectral irradiance for the SORCE instrument complement. This document provides the scientific motivation and goal of the SORCE mission, a brief introduction to the instruments and a detailed discussion of the theoretical and mathematical algorithms utilized in the production of scientific results. It is not designed to serve as the only reference to the SORCE instruments, data and their algorithms. Other documents will be generated to explain, in much greater detail than presented here, instrument design and operation, instrument calibration, and the ground data system. These related documents should be consulted to complement the information contained here.

1.2 Scope

This document describes those algorithms required to generate solar spectral and total irradiance data sets from direct observations of the Sun from space. The appendices attached to this document provide a more detailed description of the content and format of the SORCE data products. The algorithms are described as they are known during the design phase of the instruments. Future changes in instrument design and results of laboratory calibration and testing may incur modifications to parts of certain algorithms

1.3 Applicable Documents

A number of documents presently exist or are being developed to complement this ATBD and are listed below:

Table 1: Related NASA Documents
1999 EOS Reference Handbook
1997 EOS Data Products Handbook

Table 2: Related LASP Documents	
SORCE Mission Requirements Document (MRD): Rev B	Doc. # 20560-T6-0003
SORCE Instrument Requirements Traceability Matrix	Doc. # TBD
SORCE Contamination Control Document	Doc. # 20560-T6-0002
SORCE Product Assurance Implementation Plan	Doc. # 20560-T6-0001
SORCE PROCPAR	Doc. # 20560-T6-0004
SORCE Integration and Test Plan	Doc. # TBD
Total Irradiance Monitor DSP and CGCI Interface Design Document	Doc. # 20568-T5-0201
Solstice Grating Drive DSP and CGCI Interface Design Document	Doc. # 20568-T5-0101
DSP Software Design for the Solstice Grating Drive	Doc. # 20568-T5-0102
DSP Software Design for the Total Irradiance Monitor	Doc. # 20568-T5-0202
SORCE Operations Concept Document	Doc. # TBD
SORCE Instrument Calibration Plan (In Development)	Doc. # TBD
SORCE Science Data System Requirements Definition Doc	Doc. # TBD

1.4 Contributing Authors

Gary Rottman	Principal Investigator
Thomas N. Woods	Project Scientist and XPS Instrument Scientist
George Lawrence	TIM/SIM Instrument Scientist
William McClintock	SOLSTICE Instrument Scientist
Greg Kopp	TIM Instrument Scientist
Jerald Harder	SIM Instrument Scientist
Judith Lean	SORCE Co-Investigator
Martin Snow	Stellar Analyst
Christopher K. Pankratz	Ground System Manager
Barry G. Knapp	Science Processing S/W Engineer/Analyst

2 Overview and Background Information

2.1 Introduction

The Sun is the dominant direct energy source to the Earth's climate system. A generally accepted value for the total solar irradiance arriving at the top of the Earth's atmosphere is 1366 Wm^{-2} with an uncertainty of ± 2 Wm^{-2} providing a globally averaged value of 342 Wm^{-2}. This external energy input, minus the Earth's planetary albedo, is balanced by a global infrared emittance corresponding to an average Earth-atmosphere temperature of 255 K. The external energy input from the Sun in combination with surface and atmospheric processes, including the effects of clouds, aerosols, water vapor and other greenhouse gases, equilibrate to a global mean surface temperature of 288 K (15°C). Model estimates which include feedback effects arising from changes in water vapor, cloud cover and sea ice/snow estimate that an increase of 2% in solar irradiance produces a 4° C surface temperature increase [Hansen *et al*., 1994].

A continuous record of total solar irradiance exists now for more than twenty years from space-based observations, shown in Figure 1. Evident in this combined record is an 11-year cycle with peak-to-peak amplitude on the order of 0.1% and variations a factor of 2 to 3 greater on monthly time scales associated with the passage of sunspots over the disk. TSI variability apparently occurs over essentially all time scales observed thus far, from minutes (p-mode oscillations) to the 11-year solar cycle.

The measurements made by individual radiometers providing the data of Figure 1 exhibit a spread (about $\pm 0.5\%$) that is much larger than the solar 11-year or rotational cycles, and a large fraction of this spread is in fact of instrumental rather than solar origin. The individual TSI datasets in Figure 1 from 1978 to the present time include observations made by ERB on Nimbus-7, ACRIM-I on SMM and ACRIM-II in UARS, ERBS on the ERBE satellite, the SOVA on EURICA, and VIRGO on SOHO [Kyle *et al*., 1993, Willson, 1994, Fröhlich, 1994, Lee, 1995, and Fröhlich, 1996]. These data were all recorded with ambient temperature sensors, each of which has its own individual instrumental error budget, typically on the order of 0.2 to 0.3% (2000 to 3000 ppm). The ERBS, ACRIM-II, and Virgo continue to make observations; and the EOS/ACRIM or ACRIMSAT was launched in December 1999 - near the peak in the upcoming solar cycle #23.

Willson [1997] combined the two ACRIM data sets of Figure 1 using their overlap with the ERB data and his analysis suggests a net increase of solar radiation between solar minima in 1986 and 1996 (note: only two solar minima have actually been observed thus far). The estimated increase of 0.04% would induce non-negligible climate change if it persists for a sufficient number of solar cycles and if the climate system

feedbacks reached their full equilibrium response to the forcing. However, the analysis is controversial since instrumental drifts detected in the Nimbus 7 data [Chapman *et al*., and Lee *et al*.] may not have been fully accounted for in the analysis. As well, models of the TSI variability based on sunspot and faculae influences are able to reproduce much of the TSI variability in Figure 2, but not the upward trend between solar minima that Willson's analysis infers [Fröhlich and Lean, 1998].

Because of selective absorption and scattering processes in the Earth's atmosphere, the climate system responds in distinct ways to solar energy inputs in different spectral regions. The Earth's atmosphere absorbs completely solar radiation in the ultraviolet (UV) spectrum at wavelengths shortward of 315 nm. This radiation becomes the dominant direct energy input to the middle atmosphere and plays a major role in the physical processes there — including the photochemistry, dynamics, temperature, composition and structure. It is critical for both the formation and destruction of ozone. Even small changes in the incoming solar UV radiation produce commensurate changes in middle atmosphere parameters. Longer wavelength visible and near infrared radiation penetrates to the lower atmosphere and to the Earth's surface. When averaged over the globe, roughly half of the incoming solar radiation is either absorbed in the atmosphere or scattered back into space, the remaining half being absorbed at the surface. Since atmospheric scattering and absorption processes are all wavelength-dependent, it is essential to understand the variation of the Sun's radiation as a function of wavelength to properly understand the physical processes by which solar irradiance variability may influence climate. Solar ultraviolet radiation comprises less than 1% of TSI, yet may account for 30% of its 11-year cycle variation. From a combination of observations and model calculations Kiehl and Trenberth [1996] suggest that approximately 20% of the TSI is absorbed principally by clouds, stratospheric ozone and other minor constituents, and tropospheric water vapor - all processes that are strongly wavelength dependent.
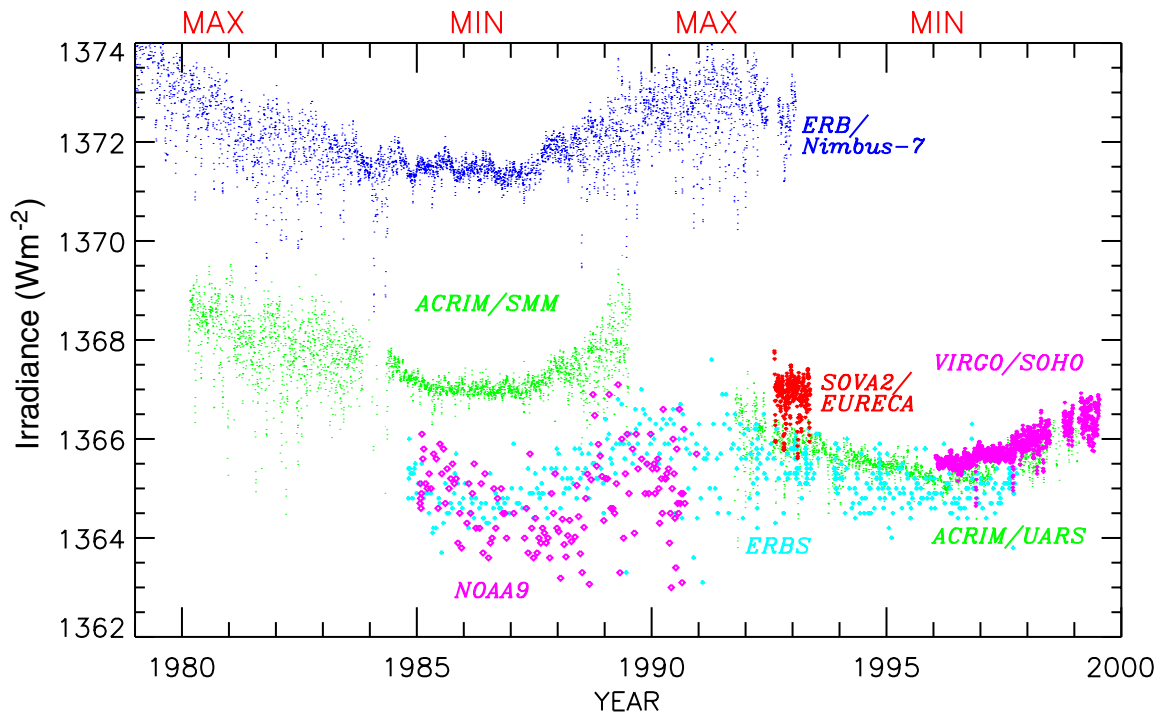
Figure 1: Record of TSI Measurements

Only in the UV portion of the solar spectrum are present observations sufficient to provide an understanding of the 11-year cycle amplitudes and variability mechanisms. At wavelengths longer than 400 nm the 11-year variability is small and remains undetected by all earlier observations. Starting in the

1950's observations began, first with sounding rockets and later with longer-duration satellite missions. Achieving precise and accurate measurements in space has proven difficult, and early UV spectral irradiance observations had accuracies no better than tens of percent, or perhaps a factor of two. More recent measurement programs have improved, and since 1991 the SOLSTICE and SUSIM instruments on UARS have elucidated solar UV irradiance variations, now thought to be less than 10% at wavelengths longward of 150 nm. and less than 1% longward of 300 nm.

Figure 2 shows the solar irradiance between 120 and 2000 nm where the spectrum is displayed with an effective spectral resolution of 1 nm. This spectrum has the general characteristic of a continuum spectrum throughout, with many absorption features, both lines and absorption edges, and at the shorter wavelengths superposed with emission features. In consideration of the Sun as the source of this emission, the longest wavelengths originate low in the photosphere, and progressing toward shorter wavelengths the emission originates higher and higher in the solar atmosphere, until at the very shortest wavelengths the emission is dominantly from the chromosphere with a few higher temperature lines originating in the solar transition region. Appendix A provides a discussion of recent LASP observations of solar irradiance and describes the present understanding of solar variability, especially in the ultraviolet.
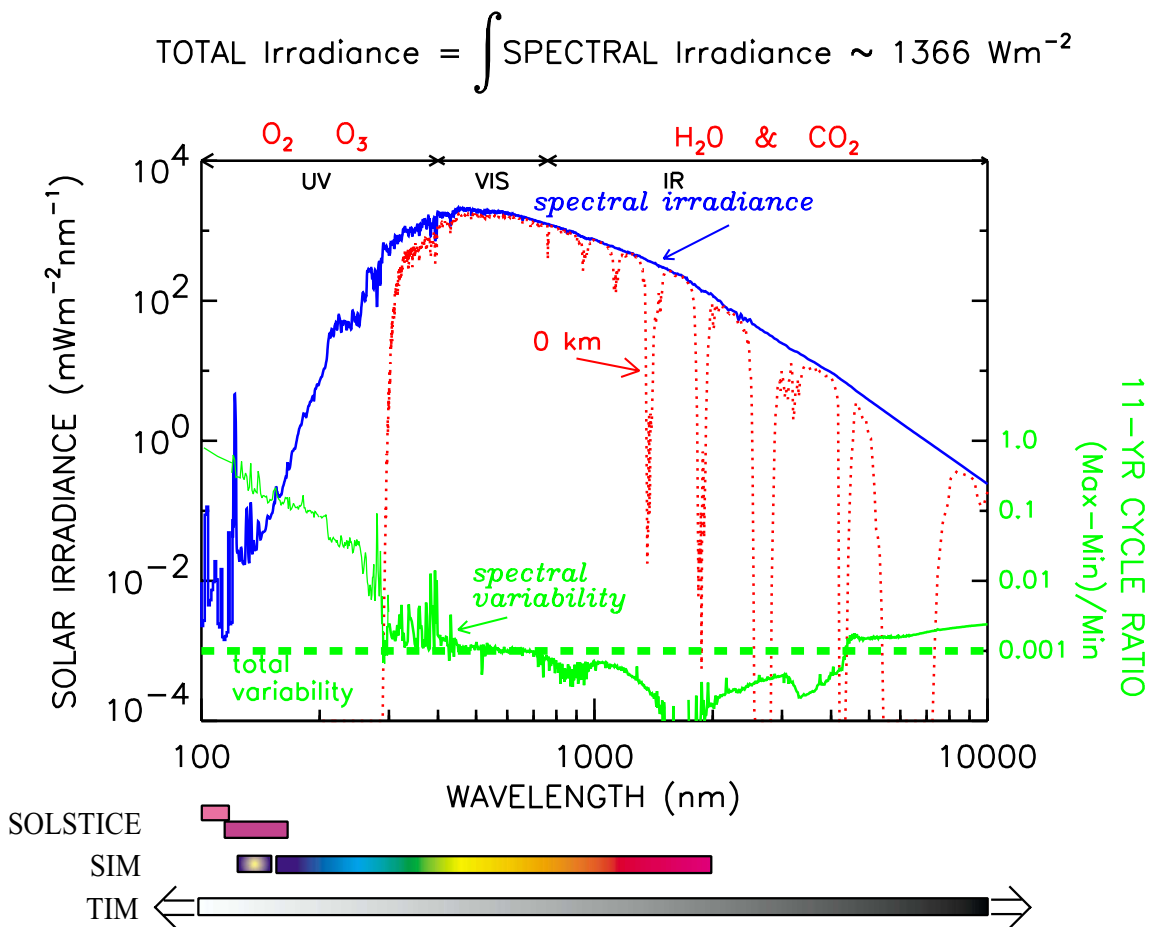
Figure 2: Solar Irradiance and Solar Cycle Variability

2.2 Science and Mission Goals and Objectives

The overall goal of SORCE is the measurement of solar irradiance and the specification of its variability with high accuracy, precision and stability, for global change applications. The specific science objectives that must be accomplished in order to achieve the goal are comprehensive, and address issues including measurement accuracy, spectral coverage and resolution, temporal resolution, and the timeliness of the data delivery of the scientific community. These objectives derive from needs of the user community, but also from the scientific imperative of establishing a long-term solar data set that achieves state-of-the-art radiometric standards and capabilities. Using present technology and the resources available to the SORCE project, the solar irradiance measurements will have unsurpassed accuracy and long-term stability, thereby facilitating new knowledge and understanding of the Sun and its influence on our atmosphere and climate.

The SORCE observations attempt to reconcile scientific priorities within both the solar and atmospheric communities. As a specific example, the measurement requirement for the spectral resolution of the SORCE instruments derives from both the need for solar scientists to specify and understand irradiance variability and the knowledge required by atmospheric scientists of the radiative processes in the atmosphere. Subgroup of scientists exist in both communities desiring higher spectral resolution than SORCE will achieve, yet there is no straightforward technique to meet their needs and still achieve the high radiometric accuracy which is essential for both solar variability and climate change studies, and is the primary science goal of SORCE. It is our hope that the somewhat lower spectral resolution SORCE observations, perhaps combined with other ground-based or modeled spectral information, will be able to satisfy the needs of these scientists.

The time resolution of the *SORCE* data is another example of how we have established a measurement requirement that will address the needs of most, but perhaps not all, users. Day (24 hour) or orbit (90 minute) boundaries are logical choices for an inherent time resolution of the SORCE data. We have selected a standard time interval of six hours for the highest level SORCE data reported, and we anticipate that this cadence will satisfy most users — they may in fact prefer a value of only once per day. On the other hand, certain studies may request higher time resolution, or perhaps they may seek a solar measurement coincident with a specific time. Responding to such special requests the SORCE Science Team will provide these data, usually retrieved from the Level-2 data set.

The Science Objectives of SORCE:

1. Specify daily total solar irradiance (TSI) with a combined standard uncertainty of less than 100 ppm (0.01%) based on SI units, and a relative accuracy of 0.001%/yr. Relate the *SORCE* observations to all concurrent and previous observations attempting to understand and eliminate the bias between the various data sets, thereby continuing the long-term historical record.

2. Specify daily solar ultraviolet irradiance, 120 to 300 nm, with a spectral resolution of 1 nm. Achieve an absolute accuracy of better than ±5%, and a precision and long-term relative accuracy of ±0.5%. Use the solar/stellar comparison technique to relate the solar irradiance to the ensemble average flux from a number of bright, early-type stars. (Using the same stars now observed by the UARS SOLSTICE will provide a direct, and unambiguous comparison of the SORCE and UARS observations.)

3. Make the first precise measurements of the visible and near infrared solar spectral irradiance suitable for future climate studies. Obtain daily measurements of solar spectral irradiance between 0.2 and 2 μm, with a spectral resolution ($\Delta\lambda/\lambda$) of at least 1/30, an absolute accuracy of ±0.1% (1σ), and a precision and relative accuracy of better than ±0.01%/year.

4. Validate and understand the reasons for the observed irradiance data in terms of solar variability, and assess how the variable irradiance affects our atmosphere and climate. Use this knowledge to improve estimates of past and future solar behavior and climate response.

The Mission Goals of SORCE:

1. Successfully operate and obtain data from the SORCE spacecraft for a period of 5 years, and process and analyze all engineering data to ensure the health and safety of the spacecraft and instruments.

2. Within 24 hours of data capture, process all science data with the associated instrument and spacecraft engineering data to derive the Level 3 science data products. Calibrate the data for all SORCE instruments, converting instrument signals to standard geophysical units (W/m^2 or $W/m^2/nm$).

3. Characterize the operation of SORCE instruments, analyze and correct the science data as appropriate for changing instrument performance. Provide validated data to the scientific community in a timely fashion, and collaborate with users to ensure that these data are used in an appropriate and conscientious manner, with special emphasis on conveying information on data quality and uncertainty.

4. Obtain a complete observation set with SORCE on at least ten of the fifteen spacecraft orbits per calendar day. The Level 3 data are 4/day values representing the appropriately weighted mean of the Level 2 orbit-by-orbit measurements. The higher time resolution data are available to meet secondary science objectives, for example, studying the passage of faculae and sunspots across the solar disk.

5. Validate the SORCE data against other simultaneous space observations (if they are available), against previous observations, and against our best known models of solar radiation.

6. Through the development and operation phase of SORCE, refine and improve our understanding of the instruments and the data they return.

2.3   Instrument Characteristics

The primary goal for the SORCE mission is the specification of solar total and spectral irradiance and its variability with high accuracy, precision and stability. To achieve this goal, and the associated science objectives, the SORCE mission consists of five separate optical devices — one four-channel cavity radiometer called the Total Irradiance Monitor (TIM); three spectrometers, one called the Solar Irradiance Monitor (SIM) and two (redundant) copies of the Solar Stellar Irradiance Comparison Experiment (SOLSTICE); and one photometer array called the XUV Photometer System (XPS).

Figure 3 schematically distinguishes the three types of instruments. The right panel illustrates the concept used to measure the total irradiance, or radiative flux density, using an entrance aperture followed by a detector sensitive to all wavelengths of the solar spectrum. The middle figure illustrates a generic spectrometer using an entrance slit, a dispersing element, followed by an exit slit and finally a detector to record an isolated wavelength of the solar spectrum. Finally, the right-hand panel shows a basic photometer design with an aperture, a filter to isolate a fixed range of wavelengths, followed by a detector. All three measurement approaches require knowledge of the aperture area, the throughput of the instrument, and the sensitivity of the detector in order to convert the raw signals into irradiances. The spectral approaches also require knowledge of the spectral bandpass (exit slit width for the spectrometer and effective filter bandwidth for the photometer)
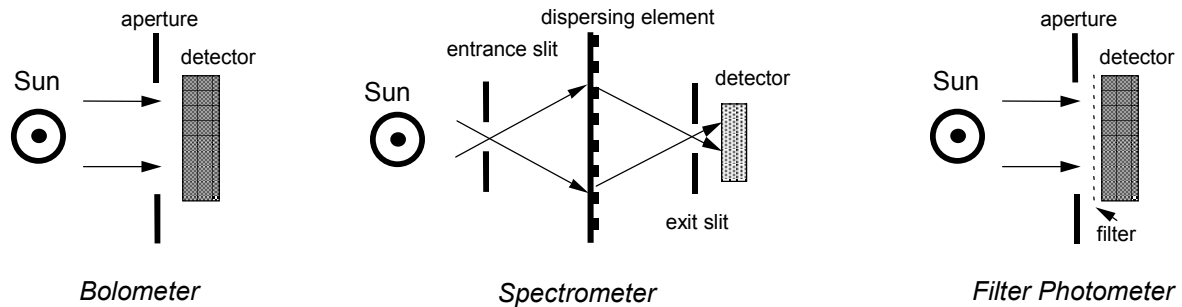
Figure 3: SORCE Instrument Concepts

The TIM is a newly developed instrument that uses the approach of phase-sensitive detection with a balanced electrical substitution radiometer (ESR) detector system to measure total solar irradiance. In TIM, four identical, conical cavities are paired and autobalanced through an AC, digital, feedback loop.

The SIM is also new developed, and uses a prism as the single optical element and an (ESR) as the primary detector to measure near-UV, visible and infrared spectral irradiance. Somewhat like the TIM, SIM also uses an absolute detector — a miniature version of the Electrical Substitution Radiometer (ESR). In order to establish and correct for changes in instrument (prism) response, SIM makes use of both redundant optical channels and incorporates a self-calibrating optical system.. This instrument has a measurement requirement of 0.1% absolute accuracy and long-term relative precision of 0.01% per year.

The SOLSTICE instrument package is a derivative of the UARS SOLSTICE G- and F-channels, and in combination they measure the solar UV irradiance from 115 to 300 nm with a spectral resolution of 0.1 to 0.2 nm. The SOLSTICE instrumentation on SORCE constitute a continuation of the SOLSTICE solar-stellar comparison technique, as first demonstrated in the UARS SOLSTICE mission. The two ultraviolet channels of SORCE are similar to the UARS SOLSTICE, in that they have the unique ability to observe bright stars using the same optics and detectors employed for the solar observations. In this way the stars become calibration standards against which the Sun is measured. UARS SOLSTICE has demonstrated that the stellar comparison technique is highly reliable and works quite well for recognizing changes in the instrument response at about the 1% level, and moreover, that the direct comparison of the solar irradiance to the stellar flux is established at the 1% level. This level of precision and relative accuracy is quite adequate for solar measurements where the variability is on the order of, or exceeds a couple of percent. That is, it is satisfactory for solar measurements at ultraviolet wavelengths below about 300 nm.

XPS is the shortest wavelength instrument. It measures the very energetic EUV and soft x-ray flux, where the solar variability exceeds a factor or two. Its precision and relative accuracy requirements are therefore on the order of ±10%. XPS is very similar to the filter photometers that have been flown on LASP's sounding rocket programs for the past seven years, are presently flying on the SNOE satellite, and have now been delivered for the SEE instrument on NASA's TIMED program.

The spectral coverage of the three spectrometer channels are not fully redundant, but each channel slightly overlaps the spectral range of the adjacent channel for purposes of data validation.

Table 3: SORCE Instrument Capabilities				
Instrument	Spectral Range	Spectral Resolution	Absolute Accuracy	Relative Accuracy (per year)
TIM	All	NA	100 ppm (1σ)	10 ppm
SIM	200 – 2000 nm	1.3-34 nm	0.03 %	0.01 %
SOLSTICE	115-320 nm	0.1-0.2 nm (solar) 1.1-2.2 nm (stellar)	3-5 %	0.5 %
XPS	1-35 nm	5 nm	12%	4%

2.3.1   TIM Instrument

The Total Irradiance Monitor (TIM) will provide an absolute accuracy of 100 parts per million (ppm) (1σ) in total solar irradiance, a long-term relative accuracy of 10 ppm per year, and a noise level of 1 ppm. In operation, TIM directly faces the Sun during the daylight portion of each orbit to measure irradiance (radiant flux density or incident radiant power per area). The instrument consists of four Electrical Substitution Radiometers (ESRs) employing modern, state-of-the-art electronics and materials. One ESR is dominantly used as the active Sun sensor. Intermittent use of the other identical ESRs enables diagnostic detection of long-term sensor degradation and provides instrument redundancy. The housing (see cut-away drawing in Figure 4) provides thermal stability and acts as a heat sink for the ESRs, which have a well-characterized thermal conductive path to the housing
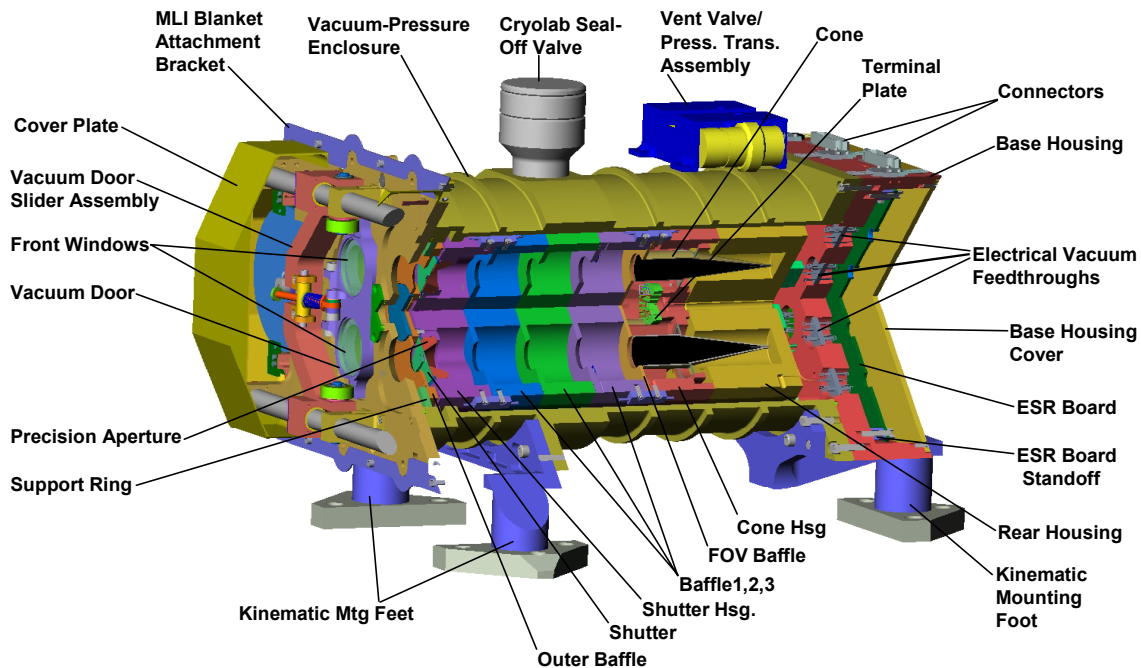
Figure 4: Cutaway of TIM instrument shows two of the four ESRs. Light entering the instrument from the left through precision apertures is absorbed by the ESRs, causing temperature changes used to determine the incident power.

A precision aperture, diamond turned to an edge radius < 1 μm determines the area of the solar flux accepted by the TIM. Baffles, located behind the precision aperture, shield the measurement cavity from Earth albedo and other off-axis radiation.

Uncertainty in aperture area is the largest contributor to the TIM's absolute accuracy budget. The apertures share a temperature sensor with 0.1°C absolute accuracy and 0.001°C resolution, so thermal variations in aperture size can be corrected to their ground-calibrated value.

Open/close shutters in front of the precision apertures regulate light input to the cones. The TIM shutters, one for each cone, are driven by brushless torque motors. The shutter temperature changes are monitored to 0.005°C. The optical labyrinth seals at the edges of the shutter are light tight to 1 ppm.

A summary of the TIM operational parameters is given in Table 4.

Table 4: TIM Instrument Properties	
Parameter	Value
Wavelength Range	All
Absolute Accuracy	100 ppm (1 σ)
Relative Accuracy (drift)	10 ppm per year
Size (instrument)	34.732 long x 30.312 wide x 20.671 high [cm]
Size (electronics)	26.16 long x 21.84 wide x 6.10 high [cm]
Mass	6.634 kg instrument, 2.8 kg electronics
Power	14 W
Design Lifetime	6 yrs
FOV	±2° without vignetting, ±6° cut-off
Pointing Requirement	±10 arcmin for ±100 ppm change
Precision Aperture Size	0.5 cm^2
Shutter Frequency	0.01 Hz
Typical Cone Reflectivity	50 ppm
ESR Temperature	30°C

2.3.1.1 Electrical Substitution Radiometers

Electrical power is applied to the highly-absorptive ESR cone to maintain a constant temperature. Periodically a shutter opens over a precision aperture allowing sunlight to fall incident on the inside of a cone (as in the left panel of Figure 3). A measured reduction in electrical power now compensates for the increase in absorbed radiant energy. Conversely, when the shutter is closed again and no light is being absorbed by the ESR, the electrical power must once again be supplied to maintain the same ESR temperature. This changing electrical power is "equivalent" to the changing incident radiant power, and thereby provides an accurate measure of the irradiance.

TIM's ESR cones are made from 1 mm thick electro-deposited 99.99% pure silver for high thermal diffusivity. The cone interiors and the heat sink have diffuse black surfaces. The specular paint used on other cavity detectors (eg., ACRIM), has been rejected because it is unstable and more sensitive to dust. Instead, the TIM uses diffuse nickel phosphorous (NiP) black, which is a highly absorptive and robust surface and is described in section 2.3.1.2. The average absorption of the cone is denoted by α. Flight cones have a measured visible reflectance $(1-\alpha)$ of roughly ±50 ppm. For determining solar variability, the crucial criteria for the sensor black are knowledge and stability of α rather than absolute blackness.

The cones are maintained within 0.001°C of their nominal operating temperature using thermistors as sensors for an electrical bridge circuit. The thermistors require high resolution but not high absolute accuracy, since they are needed only to sense changes from a nominal temperature to control the feedback loop for electrical substitution heater power. Four silver electrode spinel chip thermistors are soldered to each cone near its central support structure. Intermediate synthetic diamond chips provide both electrical insulation and outstanding thermal coupling between the cone and the thermistors. The thermistors have high sensitivity to thermal changes and have a –4%/°C Temperature Coefficient of Resistance (TCR).

When the ESR's shutter is opened, a measured reduction in heating of the cone compensates for the increase in absorbed radiant power. The change in electrical power that gives precisely the same cone temperature as that provided by the incident light is a measure of the radiant power. A portion nearest the tip of each cone is heated by a wire-wound precision 520 Ω resistor, encased in the walls of the cone. In the construction of the heater, an attempt is made to match the distribution of heater power and absorbed radiant power. If the electrical power were applied with the same distribution as the absorbed radiation, the electrical and radiant power would be exactly equivalent. In the TIM ESR cone design the power replacement equivalence factor differs from unity largely because of the delay differences in conducting heat from the rear of the cone to the central thermistors. The non-equivalence effects are reduced by making the walls of the cones thicker, by matching the heater distribution to the radiation distribution (as with the wire-wound resistor), and by increasing the thermal diffusivity of the cone (thus our selection of silver). The differential delays can be characterized by measurements versus shutter frequency. The long-term stability of the replacement equivalence depends on the finesse of the thermal interfaces, so all thermal joints are solid or soldered.

In TIM the four ESRs are arranged around a central hub (see Figure 5) whose temperature is stabilized to 0.005°C. This design provides a large thermal mass with a ≈400-second time constant, giving a low-conductivity path for heat dissipation from the cone. In the thermal design, we have used gold plated heat sinks instead of multi-layer insulation, to insure stable and finite settling time and to avoid contamination. The temperature control (heaters and thermistors) and the cone mounting are centered to prevent generation of thermal gradients. The model calculations include the time dependence of the temperature changes due to the mounting and due to the incoming solar radiation.
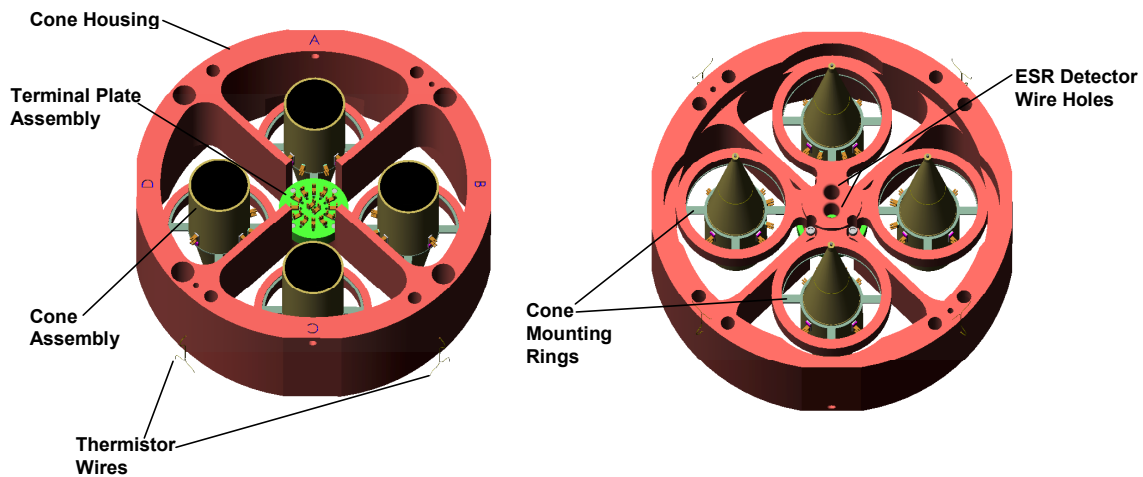
Figure 5: TIM internal cavity mounting. TIM's cavities are cantilevered from a common hub on low-conductivity mounting rings to reduce thermal noise.

2.3.1.2   NiP Black

The specular paint cavity design has been rejected for TIM because it is unstable and too sensitive to dust. Instead, diffuse NiP black, also called NIP, Ball, and NBS black, is used for the absorptive surfaces of the ESRs. Nickel phosphorous is an ultra-black coating that has a very high radiation absorption capacity due to its morphological structure. This material is described in the U.S. patent by C. E. Johnson [1980].

Ni-P black is created by plating surfaces with Nickel Phosphorus (NiP) and etching to produce a metallic, highly conductive, optically stable, absorptive surface as shown in Figure 6. Because this surface is metallic, it is extremely robust to vibration and radiation. Unlike absorptive paints, Ni-P black contains no organic molecules, which are prone to photolysis over time with exposure to solar UV.
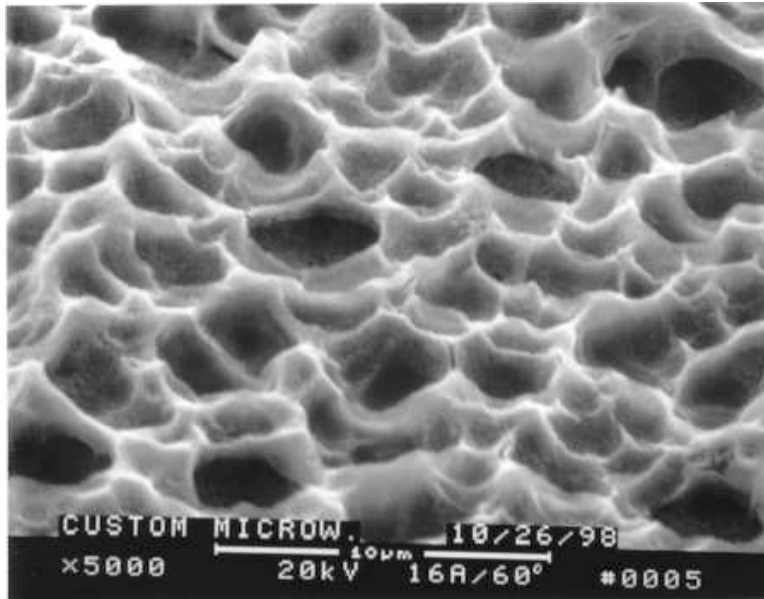
Figure 6: A scanning electron microscope image of a sample Ni-P black surface shows the rough surface that gives the material its highly absorptive properties. The cavity indentations are nearly as deep as they are wide, providing "light traps" for incident photons.

2.3.1.3　　Phase Sensitive Detection

In its normal operational mode, the TIM shutter for an ESR is cycled 50% open and 50% closed with a 100-second period throughout the orbit. We analyze only the variations in cone replacement heater power in-phase with the shutter at this fundamental frequency. This "phase sensitive detection" suppresses the instrument's susceptibility to the radiative thermal background, as well as to time-varying fluctuations in temperatures, and facilitates a non-cooled, radiometer with high accuracy and low noise.

Each cavity, with its thermistor, forms a bolometer to detect incoming radiation. An AC, digital, feedback loop controls bolometer heating via the precision wire-wound resistors. The electronics consist of the difference temperature sensing bridge, a bridge error amplifier, precision voltage sources, and a DSP-implemented servo loop for actively balancing the bridge, as shown in Figure 7. The thermistor temperature sensors on each of the two bolometers form two legs of the bridge with the opposing load resistors set to 0.76 of the operating resistance of the thermistors. This bridge configuration stabilizes the bias heating power against ambient temperature changes. Any differential bolometer temperature unbalances the bridge and the resulting error signal is amplified, digitized, demodulated, filtered, and then fed back to the cone heater from a 16-bit pulse width modulator digital-to-power converter. Normal operations is feed-forward and will provide a heater power via ground command that anticipates (to <1%) the shutter position, thereby keeping the cone temperature near constant. Comparing the active bolometer cone to the second reference cone, shielded from light, eliminates sensitivity to common mode thermal variations.
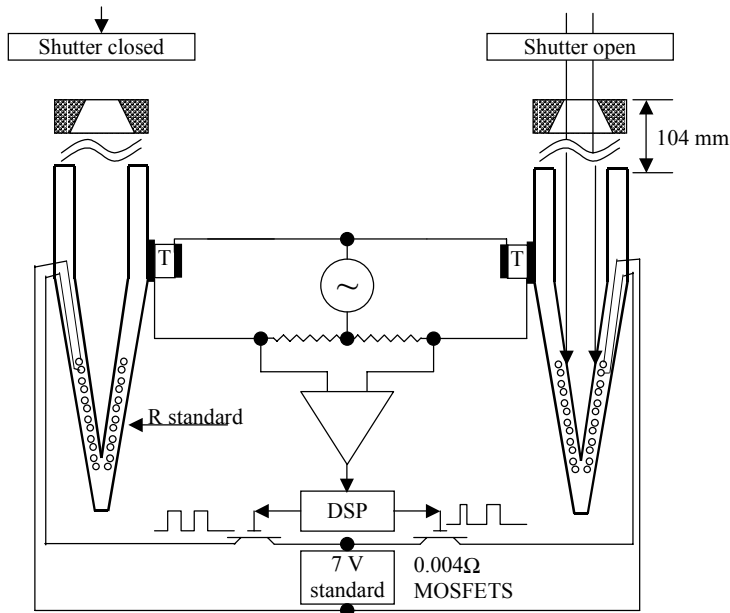
Figure 7: Schematic of the TIM servo system. Thermistors T on the cones detect differential temperature changes. The servo system and DSP change the power on one of the cones to keep the temperature constant. The standard voltage is switched through low resistance switches to the standard heater resistances on the cones.

2.3.1.4   In-Flight Calibration Corrections

The expected sensitivity to various effects is tabulated in Section 3.1.7.1. We perform several corrections to bring the sensitivity to the desired 100 ppm (1σ) absolute accuracy.

Other spaceflight instruments will provide a means of cross-checking or calibrating TIM. In particular, occasional Shuttle Hitchhiker flights of an identical TIM instrument may indicate long-term changes in the SORCE/TIM sensitivity. More importantly, the Hitchhiker flights provide a means of checking calibration of TIM before and after launch. We are building three nominally identical TIM instruments, with the intent that one fly on SORCE, the second is a mobile unit to provide cross-calibrations with other instruments and for short-duration flight opportunities, and the third will be retained as a "witness" unit, sealed in a laboratory environment. The mobile unit will fly as a Hitchhiker payload to provide intermittent, simultaneous measurements with SORCE/TIM, and then be returned to the lab where re-characterization of the mobile unit may indicate a change on the SORCE flight instrument.

SORCE will likely overlap with other spacecraft missions performing TSI measurements. SOHO/VIRGO and the UARS/ACRIM II and ACRIMSat/ACRIM III should still be operational after SORCE launch. Comparison of simultaneous TSI measurements will provide cross-checks between these instruments. The VIRGO data, taken from a heliocentric orbit, does not have the day/night effects of the Earth-orbiting spacecraft, and may provide a means of diagnosing SORCE orbital effects.

There are no other SORCE instruments providing cross-calibrations with TIM, because it does not have the spectral capabilities that the others do. An integration over wavelength of the SIM irradiances should be consistent with the TIM irradiance measurement; however, TIM has higher accuracy than SIM for TSI, so discrepancies would most likely be in the lower-resolution SIM data. Most of TIM's in-flight calibration corrections thus come from either duty-cycling identical, redundant cones or from diagnostic measurements of instrument parameters.

2.3.1.4.1 Duty-Cycling

Having four identical ESRs in the same housing provides a two-fold advantage: it provides redundancy in case of failure of a unit, and it provides a means of diagnosing degradation by allowing duty cycling between the various channels. Nominally, one ESR operates continuously while the others' shutters remain closed. We plan to run ESR-A 100%, ESR-B 1%, and ESR-C 0.1 % of the time. Degradation that scales with exposure to sunlight or use will primarily affect the active ESR. Intermittent use of other ESRs monitors trends in the degradation of the dominant one, and facilitates corrections to each instrument's sensitivity. Parameterization of such corrections is discussed in Section 3.1.6.3.

We expect these corrections to be small for TIM for the following two reasons:

1. *NiP Black is robust.* As described in Section 2.3.1.2, this absorptive surface is caused by etching into the ESR cone interior surface, making the resulting surface mechanically robust.

2. *Phase sensitive detection reduces sensitivity to long-term drifts.* TIM analyzes only for changes in electrical power supplied to each ESR at and in phase with the shutter frequency. This reduces the instrument's sensitivity to long-term thermal drifts and degradations even before comparison to redundant ESRs.

3. The flight electrical standards are stable to a few ppm.

2.3.1.4.2 Diagnostic Instrument Parameters

Additional corrections are provided by monitors on TIM or by making diagnostic measurements.

Photodiodes mounted near the front of the heat sink, out of the optical beam but facing backward into the cone, monitor the reflectivity of the cones to detect changes in absorptivity. The Si photodiode current is approximately 20 nA, and can monitor changes in the ~50 PPM cone reflectivity to 1% accuracy, providing a correction resolved to <1 PPM.

We calibrate pointing sensitivity by performing periodic (approximately once per week) field of view maps by offset pointing the spacecraft ±15° about the sun vector. A platinum thermometer on the primary aperture plate, thermistors on each shutter, and at three locations on the heat sink provide thermal housekeeping. The shutter's thermal emission and reflection contribute directly to the detected signal, since they are in phase with the shutter cycle. Of special concern are thermal variations at the shutter frequency; these are corrected using "dark" (empty space) calibration measurements taken during the nighttime portion of each orbit, interpolating between dark and sunlit temperatures.

Electronic noise and thermal noise total less than 1 ppm. The major DC background is from thermal emission and is largely removed by the shuttering process. By far the largest contributions to thermal noise are the temperature gradients transmitted though asymmetries in the physical mounting of the ESR cones. These asymmetries are measured by thermistors on opposite sides of the cylindrical housing. Most important, the mounting points of two cones in a pair must have temperature changes at the shutter frequency of <50 μK. This temperature difference is reduced by mounting the primary and reference cones at the same point. The physical supports have low thermal mass and are physically short to keep the parasitic thermal time constants small. This attention to thermal design is critical in achieving the desired noise and accuracy of the TIM.

2.3.2 SIM Instrument

The SIM is a variant of the prism spectrometer first described by Fèry in 1910 [Fèry 1910, Warren *et al*, 1997]. This instrument will measure the solar spectral irradiance 4 times per day between 0.2 μm to 2.0 μm covering about 95% of the total solar irradiance. SIM will have an absolute accuracy of 300 ppm (±1σ) and with a noise level (precision) <100 ppm. The primary detector for this instrument is an Electrical Substitution Radiometer (ESR). A closed-loop controller using a CCD as a focal plane position encoder provides a relative wavelength error (δλ/λ) of < 130 ppm. Long-term relative accuracy of the instrument is maintained by duty cycling two independent spectrometers and directly measuring the prism transmission for each. Figure 8 shows a ray trace of the prism spectrometer and Figure 9 shows an optical layout of one SIM channel. The original concept for SIM is described by Rottman *et al.* [1998] and Harder *et al.* [2000] describe the radiometric measurement equation for this instrument.

Table 5: SIM Instrument Properties	
Wavelength Range (nm)	200-2000
Resolution (nm)	1.3-34
Spectrometer f/#	f/16
Sun Viewing f/#	f/115
Prism Aperture (mm)	25×18
Focal Length (mm)	400
Prism Vertex Angle	34.5°
Front Surface Radius (mm)	435.3
Back Surface Radius (mm)	445.4 (aluminized)
Prism Transmission Over λ	78% to 85%
Slit Sizes (mm)	7×0.3
Scan Range in Focal Plane (mm)	71
Optical Aberrations at Exit Slit (μm)	5
Diffraction Correction (%)	0.3-2.2
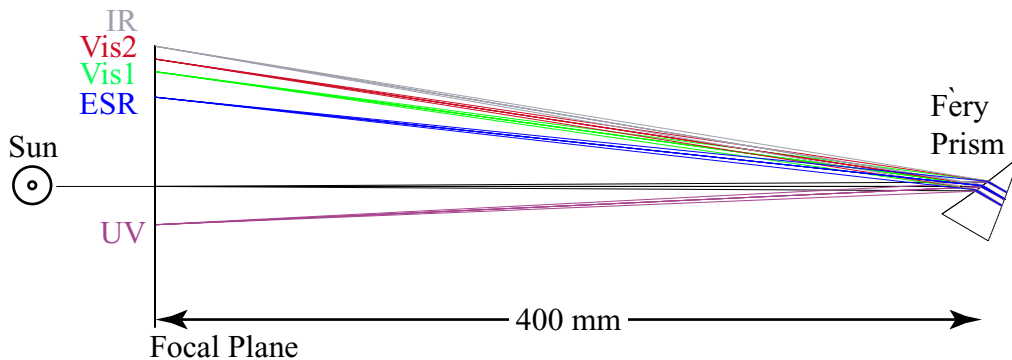
Figure 8: Ray trace of the SIM prism spectrometer

14
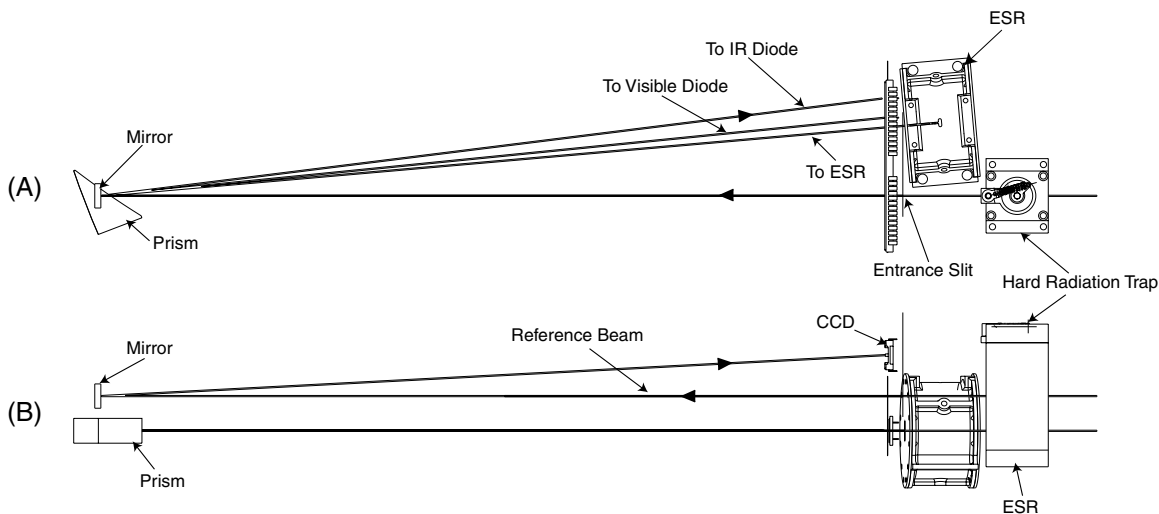
Figure 9: SIM Optical Layout

2.3.2.1   **Optical performance**

For normal operation, sunlight enters the 0.3 x 7 mm entrance slit as a f/115 beam directed to the Fèry prism 400 mm from the slit. Figure 10 shows the resolving power ($\lambda/\Delta\lambda$) as a function of wavelength; the resolving power varies from 390 at 250 nm to 75 at 2000 nm, with a minimum of 33 at 992 nm. A shutter located in front of the entrance slit modulates the incoming light beam at about 0.1 Hz, in practice the shutter frequency is selected to minimize ESR detector noise. The prism has a concave front surface and a convex, aluminized rear surface that produces a dispersed and focused spectrum on the same plane as the entrance slit. The ESR is located behind an exit slit in the focal plane and is suitable for measurement over the full spectral range 250 to 2000 nm. Nevertheless, the precise measurement of the ESR is slow (~10 seconds) and requires some finite amount of dwell time. The SIM therefore includes four secondary diode detectors each capable of a more rapid response time but restricted to a more limited spectral range and by lower absolute accuracy.   N-on-p silicon diodes are used for the UV (200-300 nm) and visible (280 to 1100), a p-on-n silicon diode is used for a second visible channel (300-1100 nm), and an InGaAs is used for the IR channel (80-1700 nm). The photodiodes have a noise floor ~10^5 below that of the ESR and are insensitive to thermal infrared radiation. However, they are not absolute detectors and lack the stability and absolute accuracy of the ESR. The photodiodes are therefore calibrated against time averaged ESR signals to reduce noise. Each photodiode current is read by low voltage offset, trans-impedance amplifier. The four output signals are multiplexed and read by the ESR DSP unit; data are sampled once every 0.01 seconds and are decimated by the DSP by the same multiplier used for the ESR.

The prism-drive has actuation range of ±3°, the ESR and the four additional focal plane diodes are located in the focal plane to allow complete coverage of the spectrum in overlapping bands. Figure 11 shows the wavelength coverage of each detector as a function of prism rotation angle. Each curve is annotated to give the location of the detector exit slits with respect to the entrance slit at y=0.   Using the dispersive properties of the instrument and the area of the entrance slit, the radiant power that impinges on the detectors is calculated. Figure 12 shows a LOWTRAN-modeled irradiance spectrum after passage through the SIM exit slit and incident at the ESR as a function of wavelength and prism rotation angle. The ESR detector has a 1 nW-offset noise performance, and can therefore measure solar irradiance at 300 nm with a   single measurement signal-to-noise ratio of about 1000.

Table 5 summarizes the optical design of the Fèry prism spectrometer. The prism is fabricated from Suprasil 300 [Hereaus Amersil, Inc.]. This fused silica material has a low OH concentration (<1 ppm by mass) that gives it a smooth transmission function in the NIR. It also has outstanding radiation hardness

($>10^8$ Rad); tests of fused silica on the Long Duration Exposure Facility showed only a slight, washable, degradation [Harvey *et al.* 1992]. The index of refraction of Suprasil 300 is calculated from the Sellmeier Equation to ±30 ppm. The index of refraction has a temperature dependence of 10-15 ppm, so the prism temperature will be regulated to ±2° C with 0.04° C knowledge of variations [Malitson 1965].

A hard radiation trap (HRT) protects the prism against degradation from ionizing solar radiation. This device will insert a fused silica window in front of the entrance slit to filter out UV radiation (λ<180 nm). The window is retracted for the precise absolute irradiance measurements, but is placed in the optical train for instrument tests and other solar observations.
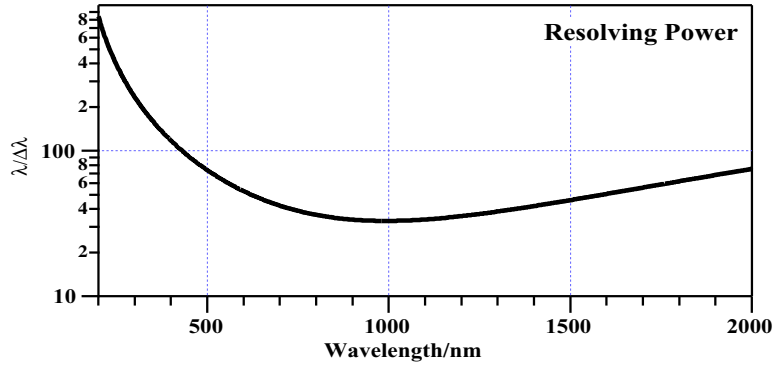
Figure 10: SIM Resolving Power
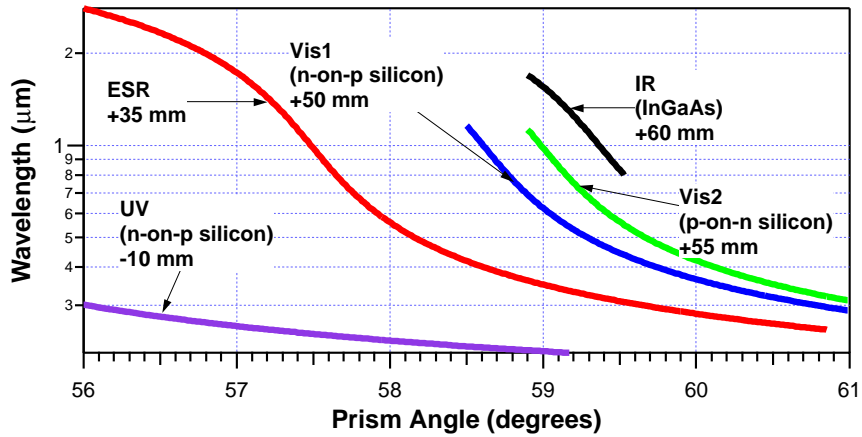
Figure 11: SIM Spectral Coverage

16

Prism Rotation Angle (degrees)
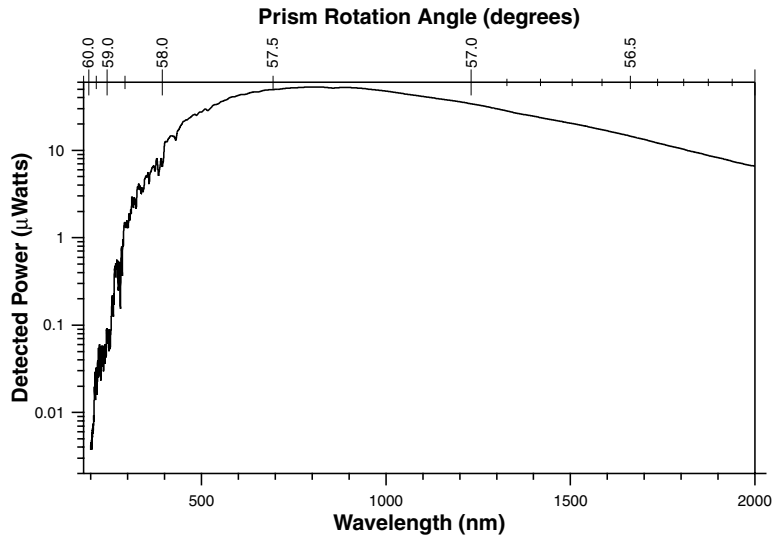
Figure 12: Sample SIM Spectrum

2.3.2.2 Prism Drive

The solar spectral intensity varies dramatically over the SIM spectral range. At the SIM resolution the structure in the spectrum requires precise stability and location of the prism position. At certain wavelengths this precision is less important (smoothly varying spectrum) whereas at other wavelengths the gradient is large and position requirement is extreme. The prism drive achieves 0.3-μm precision by rotating the prism on a flex bearing with a flex-suspended voice coil motor. Closed-loop control of prism rotation uses a small concave mirror located on the prism table to focus a second, reference solar beam back to the focal plane and onto a 12,000 element (78 mm active length) linear CCD (Thomson TH7834C). The CCD sensor at the focal plane compensates for motion and deflection of the optical bench.

2.3.2.3 Electrical Substitution Radiometer

The ESR optical head, shown in Figure 13, consists of dual bolometers each at the center of an optical quality isolation hemisphere, which reflects light back onto and thermally shields the detectors. Each bolometer consists of a 1.5 x 10 x 0.3 mm CVD (Chemical Vapor Deposit) diamond strip that is blackened with nickel phosphorous on the side that absorbs radiation from the spectrometer. Nickel phosphorous is described in Section 2.3.1.2. Two temperature sensing bridge thermistors are placed at both ends of the bolometer so that the servo system regulates the average temperature of the strip ends. Replacement heat is supplied by an integral 100 kΩ thin film resistor deposited on the backside of the diamond wafer**.** The bolometers are positioned with a low thermal conductivity Kapton support system. The hemispherical surfaces are diamond-turned in an aluminum block, nickel-plated, polished, and then aluminized to give a mirror surface. The ESR housing is gold plated for thermal isolation.

Figure 14 shows an electrical block diagram for the operation of the ESR. Incoming solar radiation is modulated at 0.1 Hz by a shutter and then passes through the spectrometer (entrance slit – prism – exit slit) and impinges on the active bolometer. Light absorbed by the active bolometer generates a temperature difference between the active and reference elements. The two bolometers along with the bridge resistors form a precision balanced AC bridge system that is excited at 100 Hz. The bridge error signal due to the temperature difference is amplified and filtered at the 100 Hz excitation frequency. This signal is then band-limited and passed to a DSP (digital signal processor) where it is sampled every 0.01 seconds. In the DSP, the signal is synchronously demodulated and filtered with a PID (Proportional Integral Differential) loop filter. The output of the PID loop filter is converted to a heating power by the pulse width modulated digital-to-analog converter (PWM DAC), thus completing the feedback loop. The 100 samples per second

data are decimated by a presettable factor, packetized with information on the prism drive status and photodiode output, and added to the spacecraft telemetry stream.

a) ESR

b) Bolometer Detail
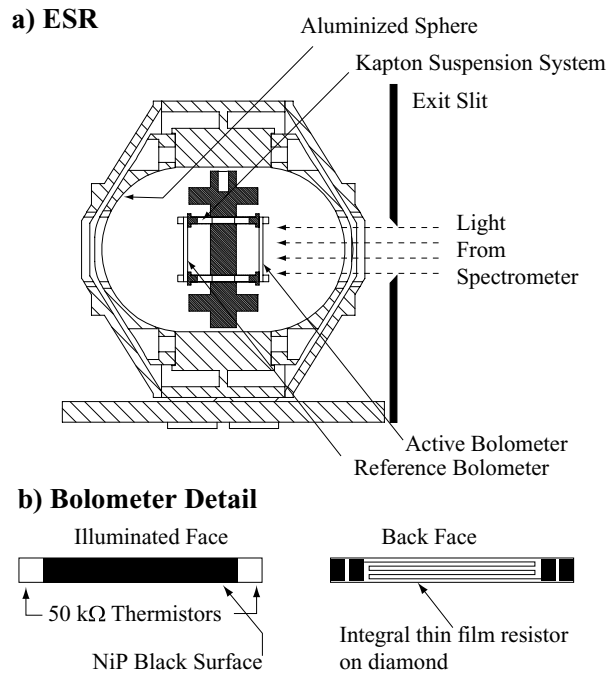
Figure 13: ESR Design
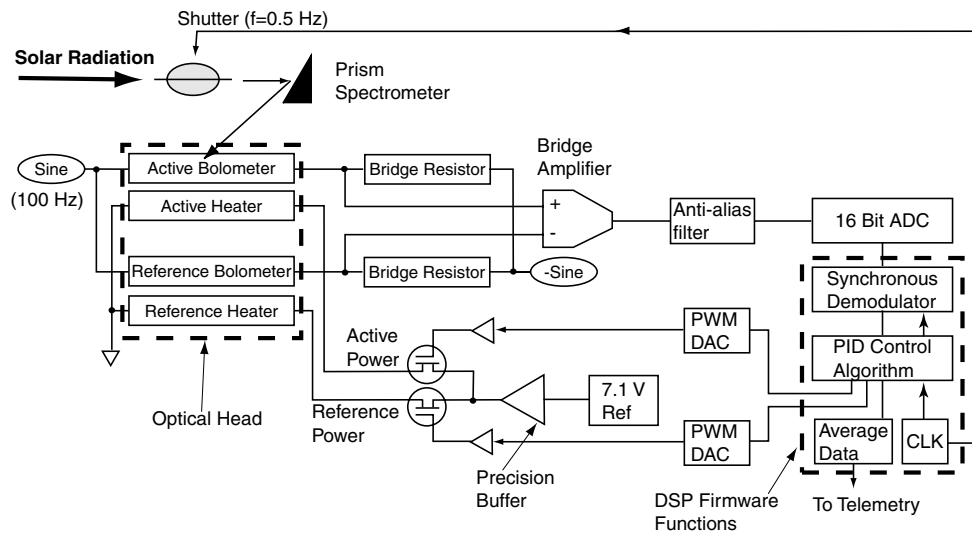
Figure 14: Electrical Diagram for SIM ESR Operation

2.3.2.4   SIM Science Operation Modes

The SIM instrument uses four modes of operation to acquire science data.

1) <u>ESR operation</u>. A table of 20-30 CCD pixel locations (wavelengths) is up-loaded to the DSP where it is maintained locally. The operation consists of stepping to a CCD location specified in the table, operating the shutter at a fixed frequency (nominally 0.1 Hz synchronous with ESR data sampling), and measuring the irradiance at this position for a fixed number of shutter cycles. The prism drive is then

stepped to the next position and the process is repeated until the end of the table is reached. The pre-selected wavelengths correspond to local maxima and minima in the solar spectrum to provide the most reproducible spectral irradiance measurement. About 3,000 seconds are needed to complete this table, and typically two full orbits are used to complete the operation. Alternate tables and modifications to the default table can be generated and up-loaded to the spacecraft.

2) Photodiode fast scan mode. Because photodiodes have a fast response time compared to the ESR, the prism drive can be operated in a scanning mode where the prism is stepped 3 times per slit width at a scan rate of 100 μm/s. The fast scan has the advantage of capturing the full solar spectrum in a short time period to avoid 1/f noise contributions from distorting the spectrum. Approximately 700 steps (seconds) are needed to cover the full 200-1700 nm range of the photodiode suite; subranges can be measured by loading start position, step size and number of steps in to the wavelength controller. The steep portions of the solar spectrum are benchmarks for wavelength registration. The radiant sensitivity of the photodiodes will be calibrated at the pre-selected ESR measurement points and a cubic spline function is used to generate the full functional dependence. At least one fast scan and 15-20 table entries in the ESR operation are performed in a nominal 45-minute observation period.

3) Fixed wavelength operation mode. For instrument diagnostics and studies of short-term solar variability the wavelength drive can be held at a specific value for pre-selected time periods. This mode will give ESR data and photodiode data at their separate and adjacent wavelengths. There is no daily requirement for the instrument to be operated in this mode, and it will be scheduled only as needed.

4) IR Scan Mode. The InGaAs photodiode gives limited coverage of the solar spectrum in the infrared part of the spectrum, so the ESR will be operated in the 1.5-to-2.0 μm region with the ESR operating in the step-stop-integrate mode with 100 μm steps to sample the spectrum. This mode will produce the infrared spectrum in 1 orbit and will be performed on a daily basis. Data from the photodiodes will be collected and analyzed during this mode as well.

There is a requirement for four absolute ESR/fast scan measurements and one extended IR measurement per day. The remaining seven orbits will be devoted to fast scans and ESR measurements with the HRT in place. This will allow us to continue to measure the solar spectrum without exposing the system to excessive radiation damage. HRT calibrations will be conducted, each consisting a fast scan with the HRT in place compared to one with the filter out of the optical train. Fixed wavelength operations and additional alignment maneuvers (such as cruciform scans and field of view mappings) will also be performed with the HRT in place.

2.3.3 SOLSTICE Instruments

The key assumption of the SOLSTICE technique is that the UV irradiance of an early-type star is extremely stable. For the SOLSTICE comparisons only normal, main-sequence, early-type stars are selected. Pathological stars, such as rapidly rotating and magnetic stars, are not used. Stellar theory predicts that the UV flux from bright, early-type stars should be stable to better than 1% in the UV spectral region over a time span of 10,000 years [Mihalas and Binney, 1981]. The same stellar theory predicts that the visible flux from solar-type stars should be stable to better than 1% over a time span of 1,000 years, and such theory is consistent with recent findings of solar variability of about 0.1% over the past couple of solar cycles [Willson, 1984; Hickey *et al.*, 1987].

If the SOLSTICE were limited to a single star for its calibration, the technique would be suspect. However, a clear advantage is that a large number of stars is selected, and it is the ensemble average of these stars that is used to derive the trends in the instrument response. For UARS the final selection of stable stars has been based on repeated observations throughout the long-duration mission (1991 to the present) and stars that

were found to vary excessively compared to the other stars in the ensemble have been eliminated. This same set of stars will be used for the SOLSTICE on the SORCE mission.

The SOLSTICE technique relies on the assumption that any long-term drift measured in the ensemble average of stellar observations provides a direct and accurate estimate of the drift of the instrument response, known to better than 1%. The UARS observations show that the stellar reference technique works at wavelengths shorter than about 250 nm; however, at longer wavelengths the very low stellar signals increases the uncertainty in the long-term trends to a larger value of about 2%. The SORCE SOLSTICE instrument has been modified at these longer wavelengths to provide a sensitivity enhancement of about 1000 for the stellar observations. This higher throughput is accomplished by inserting a pair of neutral density filters in the light path for solar observations and removing them for stellar observations. This approach requires an additional filter transmission correction in the data processing.

The accurate comparison of the Sun to the standard stars will also provide a mechanism by which the SORCE irradiance observations can be directly and reliably compared back to the UARS measurements. Likewise both the UARS and SORCE SOLSTICE solar observations can be directly compared to all future solar measurements if the same set of standard stars is used to adjust the "native" sensitivity scales of the various instruments.

In the visible, stars are typically twelve orders of magnitude less bright than the Sun. At ultraviolet wavelengths, the Sun's brightness drops significantly because of its relatively low effective temperature. This is not the case for much younger stars with temperatures four to five times higher than the Sun. For these stars the emission peaks in the ultraviolet and the ratio of their emission to that of the Sun is only five to eight orders of magnitude. Figure 15 illustrates the typical ratio of the irradiance of the Sun to that of a bright early-type star, in this case α-Canis Majoris with an effective temperature near 10,000° K. The approximately 10^8 ratio seen in Figure 15 is accommodated with a single optical-detector system by interchanging entrance and exit slits to increase the effective instrument sensitivity by a factor of 2×10^5- 4×10^5 and by increasing observation time by a factor of 10^2 -10^3.
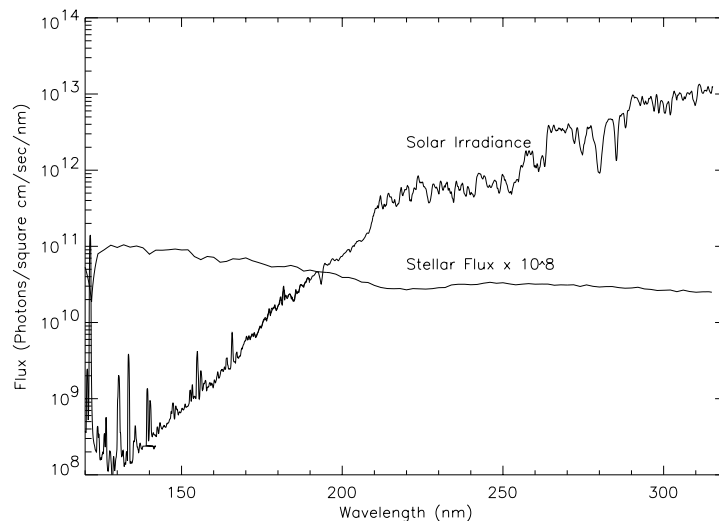
Figure 15: Comparison of solar and stellar irradiance from a typical bright early-type star.

The stars and their relative observation priorities (10 = highest priority) for UARS SOLSTICE are listed in Table 6. Additional dark sky regions used by UARS SOLSTICE to determine the in-flight dark count rates for each detector are also listed in Table 7. All bright, early-type stars were assigned a priority ranking

based on type, known variability and clear field of view, and only the highest ranking stars were selected for routine observation.

2.3.3.1 Instrument Components

The opto-mechanical configuration of the SOLSTICE instruments for the SORCE mission is based on the design of the UARS SOLSTICE instrument, but modified to meet new SORCE SOLSTICE requirements. UARS SOLSTICE employs a single mechanical housing which contains three separate spectrometers: the G, F, and N-channels which measure the wavelength ranges 115-190 nm, 170-320 nm, and 280-420 nm respectively. For SORCE the N-channel wavelength capability has been enhanced dramatically with the SIM instrument, which uses a self-calibrating optic and an absolute detector. The remaining F and G-channels have been combined in a configuration consisting of a pair of fully redundant spectrometers, each capable of measuring both solar and stellar irradiance in both the Far UV (FUV, 115-185 nm) or the Middle UV (MUV, 170-320 nm) wavelength ranges. This design approach insures that SOLSTICE will meet the extended operational lifetime requirements of the SORCE mission. Nominally, one instrument will be used primarily for FUV measurements and the other for MUV measurements. The mode-interchange capability of the instruments provides the added benefit of redundancy in the case of a failure and the ability to duty cycle and cross-calibrate the two channels

Table 6: UARS SOLSTICE Calibration Stars

Star Name	RA (2000)		Dec (2000)		V Mag	Spec Type	Priority	Calibration[†]
ε Per	3	57.8	40	0	2.90	B0.5 III	2	a,b,g
α Cma	6	45.1	-16	43	-1.46	A1 V	10	a,b,g
κ Vel	9	22.1	-55	1	2.50	B2 IV-V	2	b
α Leo	10	8.4	11	58	1.35	B7 V	7	a,b,e
δ Cen	12	8.4	-50	43	2.60	B2 IVne	4	a,b
α Cru	12	26.6	-63	7	1.35	B0.5 IV + B1 V	9	b
α Vir	13	25.1	-11	10	0.97	B1 IV + B2 V	9	b,d,e,f
η Uma	13	47.5	49	15	1.86	B3 V	7	a - e,h
ζ Cen	13	55.5	-47	17	2.55	B2.5 IV	7	a,b
β Cen	14	3.8	-60	22	0.61	B1 III	7	a,b
γ Lup	15	35.1	-41	10	2.78	B2 IV	3	a,b
δ Sco	16	0.3	-22	37	2.32	B0.5 IV	2	a,b
τ Sco	16	35.9	-28	13	2.82	B0 V	4	a,b
α Lyr	18	36.9	38	47	0.03	A0 Va	2	a,b,c
σ Sgr	18	55.3	-26	18	2.02	B2.5 V	3	a,b
α Pav	20	25.6	-56	44	1.94	B2.5 V	4	a,b
α Gru	22	8.2	-46	58	1.74	B7 IV	2	a,b,d
α PsA	22	57.7	-29	37	1.16	A3 V	2	a,b

Table 7: UARS SOLSTICE Calibration Dark Regions

Region	RA (2000)		Dec (2000)		Priority	Calibration
1	0^h	0.0^m	71°	0'	8	–
2	0	48.0	-80	0	6	–
3	3	44.0	28	0	10	–
4	4	28.1	-18	48	6	i
5	7	20.0	-84	0	10	–
6	8	16.0	32	0	10	–
7	9	56.1	-43	0	10	–
8	10	56.0	74	48	7	i
9	14	44.0	85	0	10	–
10	15	40.0	-57	0	10	–
11	15	48.0	-11	0	10	–
12	17	44.0	35	0	10	–
13	20	5.9	-20	0	10	b
14	21	44.0	33	0	10	–

[†] (a) TD-1 [Jamar *et al.*, 1976; Macau-Hercot *et al.*, 1978]; (b) Voyager [Holberg *et al.*, 1982]; (c) rocket [Bohlin *et al.*, 1974]; (d) Apollo 17 [Henry *et al.*, 1975]; (e) rocket [Bless *et al.*, 1976]; (f) rocket [Brune *et al.*, 1979]; (g) rocket [Woods *et al.*, 1985]; (h) IUE [Bohlin *et al.*, 1980]; (i) shuttle UVX [Tennyson *et al.*, 1987].

Figure 16 shows an optical layout for a single SOLSTICE spectrometer. Light enters the spectrometer through an entrance aperture, which is selected for either solar observations (a 0.1 mm x 0.1 mm square) or for stellar observations (a 16.0 mm diameter circle) using a two-position mechanism. A plane mirror folds the beam to a diffraction grating mounted in a precision single-axis gimbal. Rotating the gimbal to a specified angle causes the grating to diffract a small wavelength band of the original beam toward a second plane mirror. This mirror again folds the beam and reflects it toward a steerable ellipsoidal camera mirror. When the solar entrance aperture is selected, it is at one of the conjugate foci of the ellipse and a demagnified image of the entrance aperture is formed at the second conjugate. Light from that image then passes through a narrow (0.0375 mm wide x 6 mm tall) exit slit located in the focal plane and impinges upon the input window of a photomultiplier detector. For the stellar mode of operation, the entrant light is collimated when it passes the 16.0 mm diameter entrance aperture. The camera mirror then forms an image in the stellar focal plane where light passes through a wide (0.75 mm wide x 6 mm tall) exit slit before it strikes the photomultiplier tube. The solar and stellar focal planes are separated by approximately 20 mm. This difference is accommodated by using another two-position mechanism that places either the solar or stellar exit slit at the appropriate distance from the vertex of the camera mirror. The exit plane of SOLSTICE contains a selectable pair of solar-stellar exit slit assemblies.
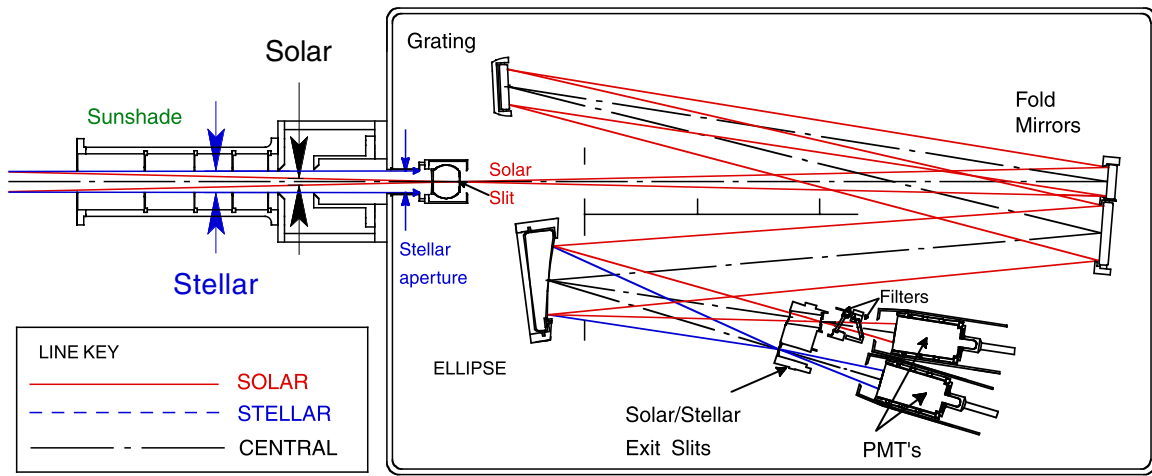
Figure 16: The SOLSTICE spectrometer configuration showing the placement of the optical elements, slit and filter mechanisms, and detectors. The mechanisms, which rotate the diffraction grating and the camera mirror are not shown in the figure.
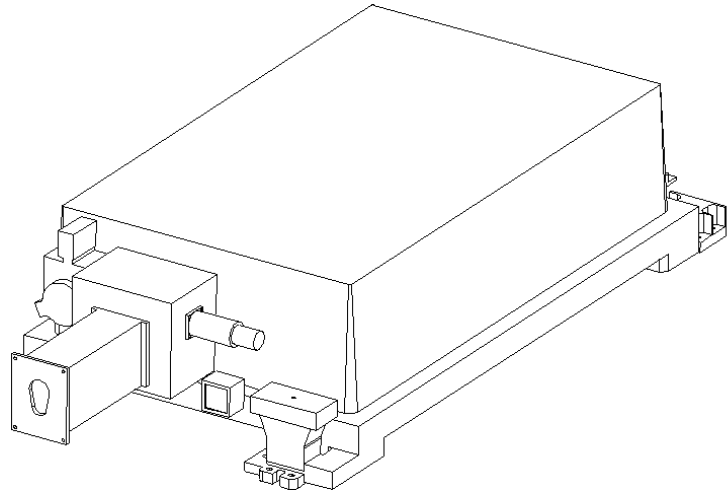
Figure 17: Assembled View SOLSTICE Instrument

Light is steered from one detector assembly to the other by rotating the camera mirror about its vertex through a 4° angle. During nominal solar observations long-wavelength light (λ>250 nm) that passes through the inboard exit slit is attenuated by a factor of 10^2 with a pair of ND-1 neutral density filters (each with an approximately 10% transmission). These filters can be individually inserted and removed from the light beam using a pair of independent two-position mechanisms. This capability improves the radiometric accuracy of the short-wavelength MUV solar spectrum (170 – 200 nm) and of data obtained from stars, and provides a technique for calibrating the transmission of each filter during flight. Table 8 summarizes the spectroscopic performance parameters for each SOLSTICE spectrometer.

Table 8: SOLSTICE Instrument Properties

Parameter	FUV Configuration	MUV Configuration
Wavelength Range	115-185 nm	170-320 nm
Grating Ruling Density	3600 grooves/mm	1800 grooves/mm
Solar Entrance Slit	0.1 mm x 0.1 mm	0.1 mm x 0.1 mm
Solar Exit Slit	0.0375 mm x 6 mm	0.0375 mm x 6 mm
Solar Bandpass	0.1 nm	0.2 nm
Stellar Entrance Aperture	16 mm Dia	16 mm Dia
Stellar Exit Slit	0.75 mm x 6 mm	0.75 mm x 6 mm
Stellar Bandpass	1.1 nm	2.2 nm
Detector Window	MgF_2	Fused silica
Detector Photocathode	Cesium Iodide (CsI)	Cesium Telluride (CsTe)

The SOLSTICE detectors measure the intensity of electromagnetic radiation that is incident on their input windows by converting individual photons into electrical pulses. After the photons enter the photomultiplier tube they are absorbed in a layer of photoemissive material, called the photocathode, that is deposited on the inside of the window. In the process of being absorbed a fraction of the photons (typically 10%) eject electrons that are accelerated into a multiplier structure. The multiplier produces an output charge pulse with approximately 5×10^5 electrons for each entering photoelectron. Finally, a charge sensitive amplifier attached to the detector output converts the electron charge pulse into an electrical signal. Each photoelectron event that exceeds a preset threshold produces a single output pulse. This mode of photomultiplier tube operation is referred to as photon-counting because the detector measures the arrival of individual photons. The amplification process for a single output pulse requires approximately 6×10^{-8} seconds to execute, and the amplifier ignores additional electron pulses generated during that interval. This 'electronic dead time', which determines the upper limit for the detector count rate as discussed in Section 3.1.2.3.3, is small enough to allow the MUV detector to operate within specification while observing the sun over the entire SOLSTICE wavelength range using a single ND-1 filter. Thus, it will be possible to accurately measure the transmission of the individual filters using a pair of closely spaced solar spectra, one taken through one filter and the other taken through both filters.

2.3.3.2 Improvements on the UARS SOLSTICE Design

SORCE SOLSTICE includes additional modifications that will improve its absolute and relative accuracy and the precision compared to UARS SOLSTICE. These include:

1. Ultra-stable high voltage power supplies and temperature regulation for the photomultiplier tube assemblies reduce both the magnitude and uncertainty of $G(V,T)$ (the temperature and voltage dependent gain correction (Equations 3.1.2.3.2 and 3.1.7.3.3b and Section 3.1.2.3.4)).

2. Real time monitors of solar and stellar position in the instrument Field of View (FOV) reduce the uncertainty in applying the $f_{FOV}(\theta,\phi)$ and $f_{Degradation}(\theta,\phi)$ corrections (Equations 3.1.2.3.1 and 3.1.7.3.3c and Section 3.1.2.3.5)) to each observation. The real time monitor also reduces the uncertainty in the correction that must be applied to the wavelength scale when stars are observed at angles $(\theta, \varphi) \neq (0, 0)$ (Equation 3.1.7.3.3c).

3. Larger, more spatially uniform detector photocathodes reduce the magnitude and uncertainty in applying the $f_{FOV}(\theta,\phi)$ correction to each observation (Equations 3.1.2.3.1 and 3.1.7.3.3c and Section 3.1.2.3.5).

4. Improvements to the diffraction grating control system reduce the magnitude of σ_λ^2 (Equation 3.1.7.3.3b) and permit individual spectra to be co-added to decrease the uncertainty in both stellar and solar signal Equation 3.1.7.3.3b).

5. Comparing results from redundant detector-grating combinations made during in-flight goniometric measurements of both the sun and stars will decrease the uncertainty in determining $f_{FOV}(\theta,\phi)$ and $f_{Degradation}(\theta,\phi)$ (Equations 3.1.2.3.1 and 3.1.7.3.3a and Section 3.1.2.3.6).

Recently NIST has upgraded the SURF II facility by improving the spatial uniformity and absolute knowledge of its output irradiance. The uncertainty in the irradiance of SURF III, $\sigma_{E_{Std}}^2$ (Equation 3.1.7.3.6c), is less than 1% over the entire SOLSTICE wavelength range.

2.3.3.3 Operational Modes

SOLSTICE observations are typically constructed using two operational modes:

1. *Scan Timed* in which the detectors accumulate counts for a fixed integration period. At the end of each integration period the grating steps to a new position. A step can be either clockwise or counter clockwise.

2. *Fixed Timed* in which the detectors count for a fixed integration time. The grating does not move at the end of the integration period.

A typical solar spectrum consists of a series of 2048 measurements using *Scan Timed* mode with an integration time of between 0.1 sec and 1.0 sec and the spacing between wavelength steps set to cover the entire wavelength range (See Table 8). Stellar observations are usually made using *Fixed Timed* mode with a typical total integration time sufficient to capture on the order of 10^4 counts.

Immediately after instrument check-out but before first solar observations, the SOLSTICE base line on-orbit performance will be established for both pairs of detectors by observing selected stars. The results from those measurements and the ground calibration will be used to select one spectrometer as nominal FUV and the other as nominal MUV. Initially, redundant detectors will be used with a 7% duty cycle (one orbit per day) for solar observations and a 50% duty cycle for stellar observations. The SORCE science team may revise this nominal duty cycle strategy based on measurements of in flight instrument degradation.

2.3.4 XPS Instrument

The SORCE XUV Photometer System (XPS) is a package of twelve silicon XUV photodiodes for measuring the XUV and EUV irradiance from 1 to 35 nm. Each photodiode has a thin-film filter to provide an approximately 5 nm spectral bandpass. These thin film filters are deposited directly onto the photodiode to avoid using delicate metal foil filters which are difficult to handle, prone to develop pin holes, and degrade with time.
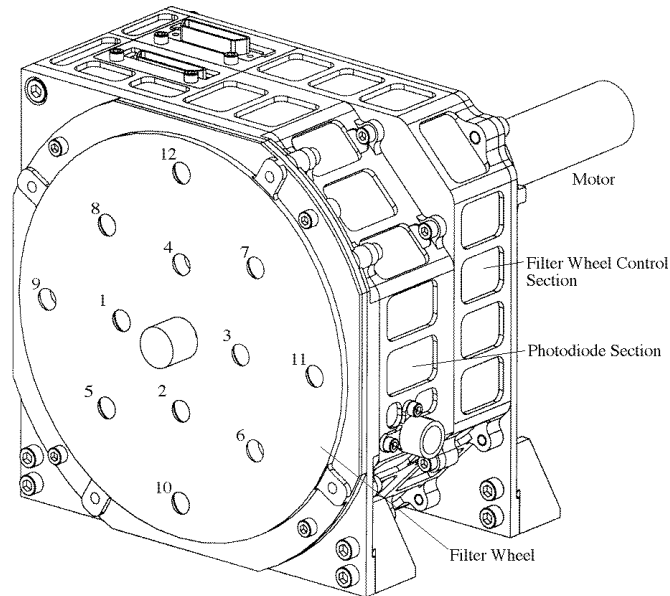
Figure 18: XPS Instrument – Assembled View

Specifications for the XPS are given in Table 9. The solar pointing requirement of 0.1° is very relaxed because the XPS is a photometer system with a wide field of view (FOV). The SORCE spacecraft will provide better than 1 arc minute pointing accuracy and will control the thermal environment to within the operating temperature range of the instruments.

Table 9: XPS Instrument Properties	
Wavelength Range	1-35 nm
Number of XUV Diodes	9
Typical Bandpass	5 nm
Mass	2.7 kg
Power Consumption	6.7 Watts
Operating Temperature	-10 to 50 °C
Pointing Accuracy	0.25°
Field of View	12°

2.3.4.1 Instrument Components

The XPS instrument includes 12 XUV photometer assemblies (Figure 19) which are packaged in the photodiode section of the XPS (Figure 18). The other section of the XPS is the filter wheel control section. Because the XUV photodiodes also have a signal contribution from the bright visible spectrum, a filter wheel that contains fused silica windows along with blank (dark) and clear apertures is required for XPS. The filter wheel control section contains electronics to control the filter wheel motor and the Geneva gears. A shaft passes through the photodiode section to a filter/aperture wheel at the front of the XPS.

The electronics for each photodiode are simple and include only a current amplifier and a voltage-to-frequency (VTF) converter. The VTF converter was chosen over an analog-to-digital (A/D) converter because the VTF converter provides a much wider dynamic range with significantly lower power

consumption. The interface from the VTF converters to a microprocessor is a 32-bit digital counter for each photodiode.
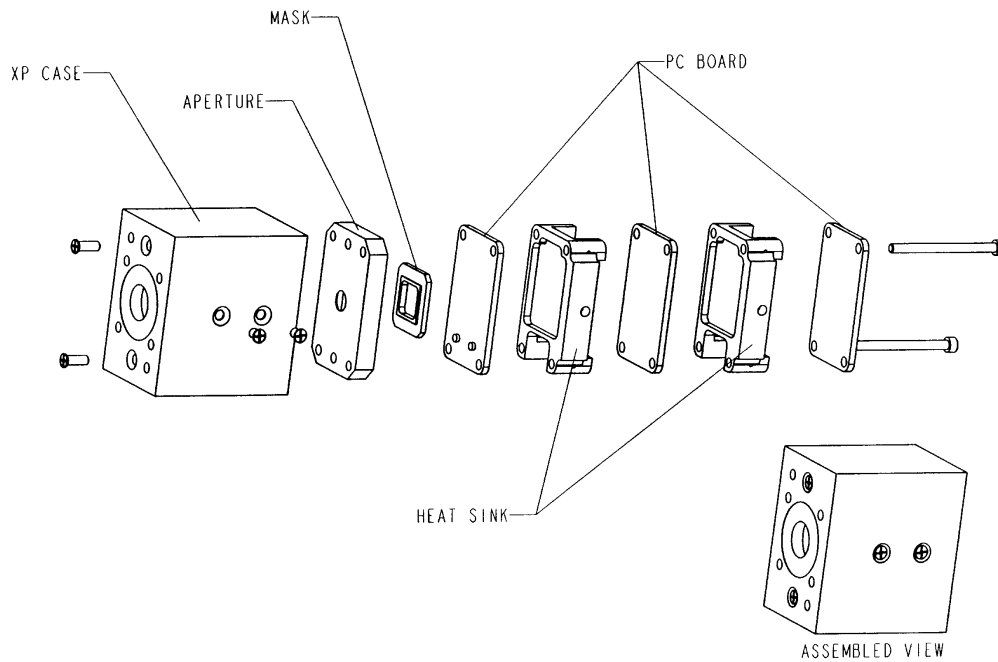
Figure 19: Single XUV Photometer Assembly

R. Korde of International Radiation Detectors has developed silicon XUV photodiodes with thin film filters to have low-noise and good long-term stability [Korde and Geist, 1987; Korde *et al.*, 1988; Korde and Canfield, 1989; Canfield *et al.*, 1989; Canfield *et al.*, 1994]. These XUV photodiodes have been adopted by the National Institute for Standards and Technology (NIST) as XUV standard detectors.
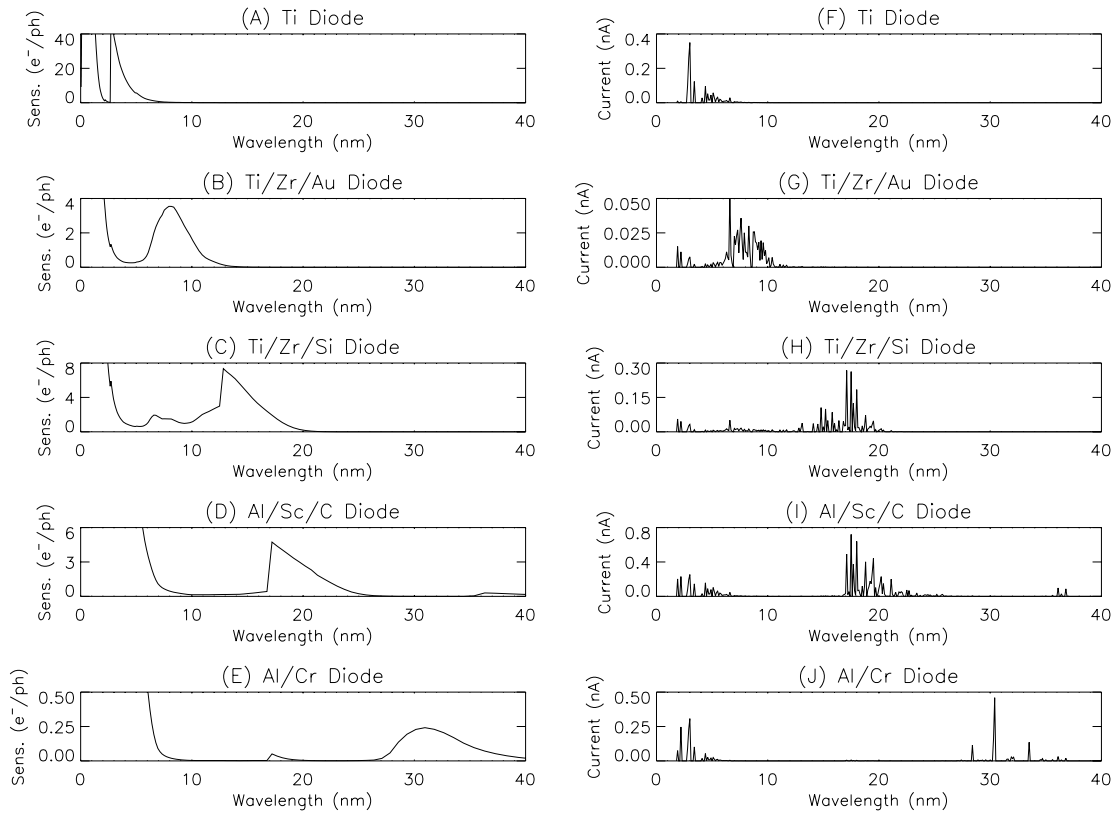
Figure 20: Sensitivity and Expected Current for the SORCE XUV Photometers. Panels A-E show the sensitivity, and Panels F-J show the expected current during solar maximum conditions, both as a function of wavelength. The coatings are (1) Ti 5000 Å, (2) Ti/Zr/Au 200/1500/1000 Å, (3) Ti/Zr/Si 200/2000/1000 Å, (4) Al/Sc/C 1500/500/500 Å, and (5) Al/Cr 2000/1000 Å.

There are several suitable metals for use as filters, and the use of multiple coatings on the same diode provides a way of narrowing the bandpass of each diode. Powell *et al.* [1990] discuss thin film filters suitable for this wavelength range. In addition to selecting a filter for its bandpass, one must also select a filter that can block the solar visible radiation by a factor of 10^{12} or better; otherwise, the XUV Photometer signal would be dominated by the solar visible radiation instead of the XUV radiation. Previous LASP projects have flown the following XUV photodiode filters: Ti, Ti/Zr/C, Al/Sc/C, Al/C, Sn, Al/Sn, Ti/Zr/Au, Ti/Zr/Si, Al/Cr, Ti/Pd, Al/Nb/C, and Al/Mn. The detector sensitivities for the silicon photodiodes of the five filters planned for SORCE are shown in Figure 20. These five filters are designed to have a bandpass of about 5 nm over the range 0 to 35 nm, a visible light blockage of at least 10^{12}, and a solar XUV signal between 1 and 10 nA. The estimated response of these XUV photometers to solar radiation is also shown in Figure 20. The XUV photometer with the Ti filter measures the irradiance below 6 nm. The photometer with the Ti/Zr/Au filter measures the 6 to 12 nm region. The photometer with the Ti/Zr/Si filter measures the 12 to 20 nm region. The Al/Sc/C filter is designed to eliminate the bright solar He II 304 Å emission so that the 17 to 25 nm region can be measured. Finally, the photometer with the Al/Cr filter measures the 25 to 35 nm solar irradiance. The additional filtered photometer is a bare XUV photodiode with Acton Lyman-α filters for a redundant measurement of the important Lyman-α irradiance.

28
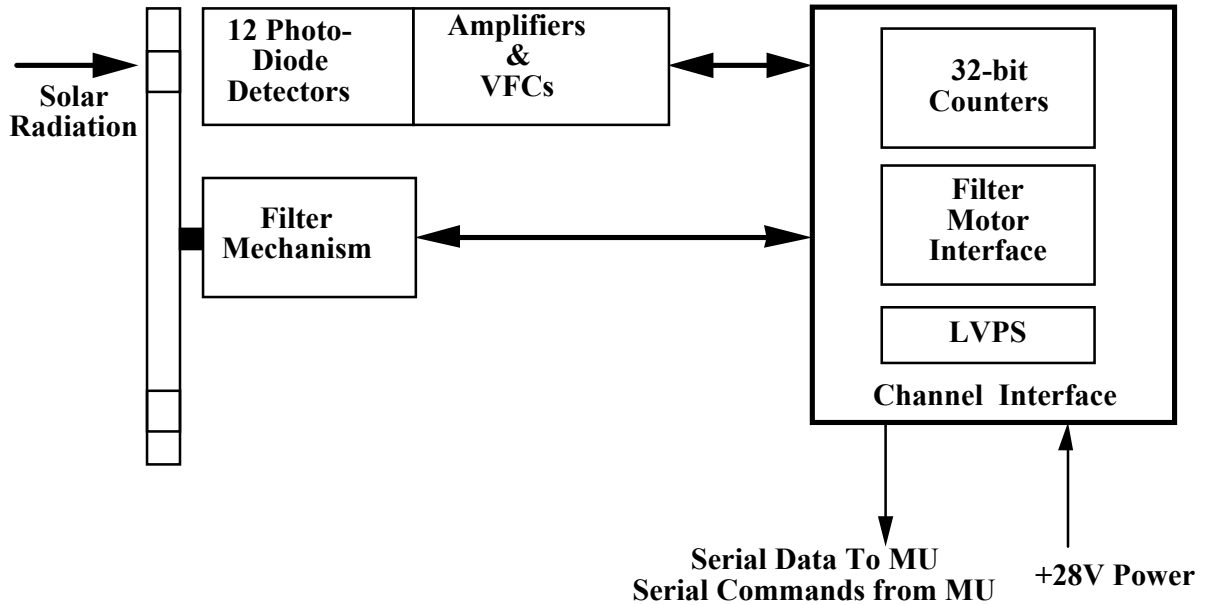
Figure 21: Block Diagram of the SORCE XPS

2.3.4.2   Operational Modes

This set of twelve XUV photometers is packaged together with a common filter wheel mechanism, which can rotate a closed aperture, a fused silica window, or an open aperture in front of any given photometer. The fused silica windows on this filter wheel permit accurate subtraction of the background signal, if any, from visible and near UV light. While nine of the XUV photometers have thin film filters for making solar XUV irradiance measurements, the other three photometers are bare silicon photodiodes to be used in tracking the transmission of the fused silica windows.   Of the nine filtered XUV photometers, one photodiode is a bare XUV photodiode with Acton Lyman-α filters for a redundant measurement of the important Lyman-α irradiance. A typical measurement cycle for the XUV photometers is to measure the dark signal with a closed aperture, to measure the background signal with the window, and then to measure the solar XUV radiation with an open aperture. For in-flight calibration purposes, three of the nine XUV photometers are redundant and will be used with a lower duty cycle (approximately once per week) for tracking instrument degradation.

The 12 XUV Photometers (XPs) are grouped into 3 sets. Each set of 4 XPs is arranged in a circle for use with the filter wheel mechanism. The filter wheel, which has 3 different rings of filters for the 3 sets of XPs, has 8 positions : 5 blocked for dark measurements, 1 clear for solar XUV measurements, and 2 with fused silica windows for solar visible background measurements (Table 10).   An observation run is a sequence of measurements from 5 consecutive filter wheel positions, normally starting and ending with dark measurements. XP #1-4 are grouped in the inner ring. XP #5-8 are grouped in the middle ring. XP #9-12 are grouped in the outer ring. XP#2, 6, and 10 are redundant XPs as part of the in-flight calibration plan. XP#4, 8, and 12 are bare photodiodes for measuring the fused silica window transmission during each observation run.   Except when making redundant photodiode measurements, one normally uses filter position #6 for the minimum amount of time to get a window transmission calibration.

Table 10: XPS Observation Summary

Observation Modes: C = Clear, D = Dark, F1 = Filter 1, F2 = Filter 2

Clear = solar XUV measurement including visible & dark signals

Filter 1 or 2 = solar visible measurement including dark signal

XP #	Coating	$\Delta\lambda$ (nm)	Pos 1	Pos 2	Pos 3	Pos 4	Pos 5	Pos 6	Pos 7	Pos 8
1	Ti/C	0-7	D	C	D	F2	D	C	D	F1
2	Ti/C	0-7	D	F1	D	C	D	F2	D	C
3	Al/Sc/C	17-27	D	C	D	F1	D	C	D	F2
4	Bare	Vis	D	F2	D	C	D	F1	D	C
5	Al/Nb/C	17-21	D	C	D	F2	D	C	D	F1
6	Mo/Au	5-12	D	F1	D	C	D	F2	D	C
7	Mo/Si/C	4-18	D	C	D	F1	D	C	D	F2
8	Bare	Vis	D	F2	D	C	D	F1	D	C
9	Al/Cr	27-37	D	C	D	F2	D	C	D	F1
10	Al/Mn	25-34	D	F1	D	C	D	F2	D	C
11	Ly-α	121.6	D	C	D	F1	D	C	D	F2
12	Bare	Vis	D	F2	D	C	D	F1	D	C

2.4   Heritage

2.4.1   Instrumentation

The instruments on SORCE bring with them varying degrees of heritage, and likewise the algorithms that process the data are at varying degrees of development. The SOLSTICE spectrometers are straight derivatives of the UARS SOLSTICE instruments, and the knowledge and understanding of the instruments operation and performance are quite robust. The algorithms that process the UARS data are well developed and are now being updated and ported forward to modern data base systems and software architecture.

The heritage for the XPS derives from sounding rocket experiments [Woods and Rottman, 1990; Woods *et al.*, 1998a], Student Nitric Oxide Explorer (SNOE) [Solomon *et al.*, 1996], and the TIMED Solar EUV Experiment (SEE) [Woods *et al.*, 1998b].

In contrast to the SOLSTICE and XPS instruments, the SIM and TIM instruments are new developments for SORCE. These state-of-the-art instruments employ large doses of new technology, especially in the Electrical Substitution Radiometers (ESR). The performance and characterization of the instruments is in mid-development, and most data processing routines are presently being built, adjusted and refined in the laboratory. This document describes present understanding of the data algorithms that will be required, but improvements will be made as a better understanding is acquired.

2.4.2   Science Data Production

LASP software engineers have extensive experience with modern object-oriented software engineering practices, methodologies, and tools, as well as with state-of-the-art scientific, numerical, and astronomical software libraries and packages. A significant portion of the SORCE processing software will consist of reusable algorithms and code already developed for other LASP projects (UARS SOLSTICE, SNOE, and TIMED). In particular, the SORCE SOLSTICE data reduction algorithms and science processing system will be nearly identical to those used for UARS SOLSTICE; much of the UARS SOLSTICE Fortran code implementing the science data reduction algorithms will be imported without significant modification into the SORCE science processing system.

3 Algorithm Description

3.1 Theoretical Description

3.1.1 Physics of the Problem

The total solar irradiance, E, is the radiant flux density at the top of the atmosphere, and is defined mathematically as:

$$E = \frac{d\Phi}{dA} \qquad\qquad 3.1.1.1$$

Likewise, the spectral irradiance, E_λ, is the radiant flux per unit area, but at wavelength λ per unit wavelength interval, $d\lambda$; and defined mathematically as:

$$E_\lambda = \frac{d^2\Phi}{dAd\lambda} \qquad\qquad 3.1.1.2$$

where $d^2\Phi$ is the element of incident flux and $d\lambda$ and dA are elements of wavelength and area respectively. The SI units of spectral irradiance are W/m^3, although alternate units may also be used (e.g., $W/m^2/nm$, photons/cm^2/s/nm or photons/cm^2/s/Å).

Considering the instrument concepts given in Figure 3, as solar radiation falls on one of the SORCE instruments, the aperture (precision aperture for TIM, entrance slit for the spectrometers, and filter aperture for the photometer) defines the area element, dA, of Equation 3.1.1.2. The element of wavelength, $d\lambda$, is established from the width of the exit slit (with appropriate dispersive relationships derived for the gratings and prisms) in the case of the spectrometers and from the effective bandwidth of the filters used in the photometers. In addition, as the photons encounter the various optical elements there are loss terms for each — mirror reflectivities, grating efficiencies, filter and prism transmissions, and finally the detector efficiencies — that must be accounted for in Equation 3.1.1.2.

3.1.2 Conversion from Instrument Signal to Irradiance

There are four similar, yet distinct algorithms to convert from instrument signal to incident solar radiation — one for each of the SORCE instruments. Each algorithm is tailored for specific optical elements and detectors of that instrument. Yet each algorithm utilizes a fundamentally similar measurement equation, and common correction terms in this equation are discussed here. The instrument-specific algorithms are detailed in the following sub-sections.

Equations 3.1.1.1 and 3.1.1.2 have three terms, which represent the incident photon power Φ, and the entrance aperture element dA and spectral bandpass $d\lambda$ over which this energy is distributed. For example, the aperture is defined by the precision aperture for TIM, the entrance slit for the spectrometers, and the filter aperture for the photometer. The spectral bandpass is established from the width of the exit slit (with appropriate dispersive relationships derived for the gratings and prisms) in the case of the spectrometers and from the effective bandwidth of the filters used in the photometers. In addition, as the photons encounter various optical elements there are associated loss terms — mirror reflectivities, grating efficiencies, filter and prism transmissions, and finally the detector efficiencies — that must be accounted for in determining incident power. Furthermore, SORCE reports the irradiances for a non-moving observer at 1 AU from the Sun, so the measured values are corrected for the motion and position of the spacecraft.

The relation between the incident photon power and the measured detector value, DN, can be expressed as

$$\text{detector signal} = \text{(photon power) x (instrument efficiencies) x (position/velocity corrections)} \qquad 3.1.2.1$$

or, more specifically,

$$DN(\lambda,\theta,\varphi) = \Phi(\lambda,\theta,\varphi) \cdot R(\lambda) \cdot Tr(\lambda) \cdot f_{FOV}(\theta,\varphi) \cdot f_{AU} \cdot f_{Doppler}(\lambda) \cdot f_{Degradation}(\lambda) \qquad 3.1.2.2$$

where

R is the detector responsivity, converting power units to detector signal units,

Tr is the transmission of the optical system,

$f_{FOV}(\theta,\varphi)$ is the sensitivity of the instrument to incidence angle,

f_{AU} is the correction for spacecraft distance to the Sun,

$f_{Doppler}$ is the correction for spacecraft velocity relative to the Sun, and

$f_{Degradation}$ accounts for changes in instrument response with time through the mission.

This gives the generic measurement equation

$$E_\lambda = \frac{DN(\lambda,\theta,\varphi)}{R(\lambda) \cdot Tr(\lambda) \cdot f(\theta,\varphi) \cdot f_{AU} \cdot f_{Doppler}(\lambda) \cdot f_{Degradation}(\lambda) \cdot dA \cdot d\lambda} \qquad 3.1.2.3$$

Corrections for position and velocity are common to all instruments, and are detailed in Section 3.1.5. All other parameters are instrument-specific, and are described in the following sub-sections.

3.1.2.1   Irradiance Conversion — TIM

3.1.2.1.1   Phase Sensitive Detection

The TIM is a shuttered radiometer with the shutter running with a 0.01 Hz square wave. The output data numbers follow the square wave with changes in the TIM digital-to-power converter's 16-bit unsigned data numbers, DN_I, proportional to changes in the solar irradiance. The cavity temperatures vary only a few mK during a shutter cycle; so system temperature vs. power relations are linear to better than 1 ppm. We thus replace the time dependence of the temperature field and the power flow with a complex Fourier series in harmonics of the shutter fundamental. We then use the in-phase signal at the shutter fundamental to determine the irradiance, requiring characterization of the radiometer to a few ppm at only one frequency and one phase. The advantages of this approach over the traditional time-domain algorithms include:

a)   The shutter frequency is selected for minimum system noise.
b)   The time convolutions become multiplications of complex numbers, replacing convolutions over time. This allows the instrument to be characterized.
c)   We can reject the out-of-phase component, mostly a first-order effect. The in-phase component mostly has effects to second order.

The time series data numbers are subject to a phase sensitive detection on the ground. Phase sensitive detection consists of multiplication of the time varying signal by a local oscillator at the reference frequency, then low pass filtering to remove noise and the harmonics of the reference frequency. The low pass filter that we have chosen is the convolution of four cycle-wide pulses. The incoming time series, DN_I, with N points per cycle, is processed to provide the complex output series $\boldsymbol{DN_J}$ as follows.

$$\boldsymbol{DN_J} = \frac{2}{N^4} \sum_{M=J-N+1}^{J} \sum_{L=M}^{M+N-1} \sum_{K=L-N+1}^{L} \sum_{I=K}^{K+N-1} e^{i2\pi I/N} DN_I \qquad 3.1.2.1.1$$

This filter consists of multiplication by the complex sinusoid at the shutter frequency, then low-pass filtering with four repeated box-car running averages. This algorithm, with its normalization, must be applied to all the data numbers from the replacement heater DAC, and also (as needed) to the shutter waveform. The timing of the center of gravity is left unchanged. The four filters have zero response at the harmonics of the shutter frequency, and the repeat of four is adequate to reject baseline drift. We denote the time series data numbers as DN_I, and the phase-detected data numbers with **bold face DN_J**. The transformed data numbers $\boldsymbol{DN_J}$ are highly over-sampled, and can be decimated in the final product.

3.1.2.1.2   The Measurement Equation

The signal flow diagram Figure 22 relates the corrected solar irradiance E_0 to the observed (Fourier Transformed) Digital Data numbers $\boldsymbol{DN}$.

$$
\boxed{E_0,\ \text{Total Solar Irradiance}}
$$

E_0, Total Solar Irradiance
f_{AU}, Inverse Square Factor
$f_{Doppler}$, Doppler Factor
$\boldsymbol{\Psi}$, Waveform transmit at shutter freq
A_P, Aperture transmission
α, Cavity absorptance
$\boldsymbol{Z_R}$, Thermal Impedance: Radiation
Thermistor: Summing Junction
$\boldsymbol{Z_H}$, Thermal Impedance: Heater
dP/dDN, Standard Digital Watt
$\boldsymbol{-G/(Z_H\,dP/dDN)}$, Servo Gain
$\boldsymbol{DN_F}$, Feed forward

$\boldsymbol{DN}$, Data

Σ
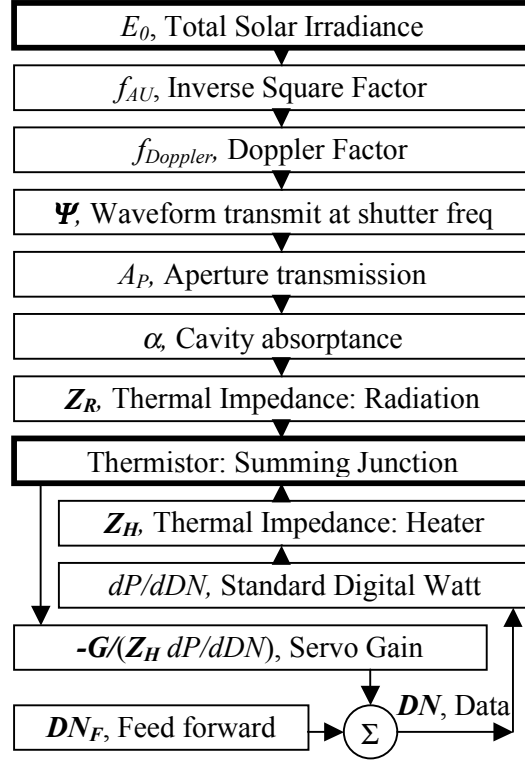
Figure 22: Signal flow diagram for TIM. The bold numbers and the arrows are complex phasors proportional to power changes. The boxes are multiplicative transfer functions: output/input. Junctions of arrows are summing points.

Writing the implicit equation of Figure 22 and solving for the irradiance gives the basic measurement equation 3.1.2.1.2.

$$
E_0 = real\left\langle \frac{V^2}{MR_H'}\, \frac{\left\{ -\left(\boldsymbol{DN_{Sun}} - \boldsymbol{DN_K}\right)\left(1 + 1/\boldsymbol{G}\right) + \left(\boldsymbol{DN_F} - \boldsymbol{DN_{KF}}\right)/\boldsymbol{G}\right\}}{f_{AU}\, f_{Doppler}\, \boldsymbol{\Psi}\, A_P\, \alpha\left(\boldsymbol{Z_R}/\boldsymbol{Z_H}\right)f_{FOV}\left(\theta,\phi\right)} \right\rangle.
\qquad 3.1.2.1.2
$$

where $\boldsymbol{DN_{Sun}}$ are the data numbers from observations of the Sun and $\boldsymbol{DN_K}$ are from observations of dark space. The data numbers $\boldsymbol{DN_F}$ and $\boldsymbol{DN_{FK}}$ are the digital feed-forward values applied during the solar and dark observations, respectively. $\boldsymbol{G}$ is the servo open loop gain at the shutter fundamental. In equation 3.1.2.1.2, V is the standard voltage that is duty-cycle switched into the standard resistor R. The pulse width counter has a full count of $M \equiv 64000$ so that DN/M is the duty cycle of the pulses, proportional to changes in average power. The (bold) data numbers $\boldsymbol{DN}$ and the shutter transmission factor $\boldsymbol{\Psi}$ are the complex Fourier components, at the shutter fundamental, of the observed time series of data numbers DN as defined in equation 3.1.2.1.1.   The complex thermal impedances $\boldsymbol{Z_R}$ and $\boldsymbol{Z_H}$ are the Kelvin/Watt thermal impedances to the thermistor from the radiative input and the heater input, at the shutter fundamental.

The following sections discuss and expand each of the factors of equation 3.1.2.1.2.

3.1.2.1.3   DAC Calibration Factor — $V^2/(MR)$

The data numbers produced by the servo system are converted by a precision duty-cycle type Digital-to-Analog Converter (DAC) to the replacement power. The changes in the substituted electrical power are proportional to the duty cycle and the V^2/R power, corrected for the lead resistances.

$$\frac{dP}{dDN} = \frac{V^2}{M R'_H}$$
<div align="right">3.1.2.2.3A</div>

where V is the value of the precision, buffered, standard voltage. The integer M≡64000 is the full scale (100% duty cycle) count. R'_H is the effective heater resistance at the regulated operating temperature. R'_H includes lead corrections both inside and outside of the optical head as well as the on-resistance of the MOSFET switch in the pulse width modulator circuitry.
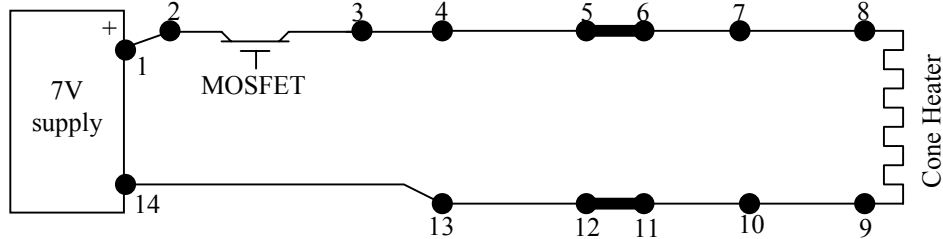
Figure 23: Standard Watt Pulse Width Modulator Hardware. The numbered nodes are measurable points in the circuit. See Table 11 for their usage and the required resistances and voltages.

Nodes	Symbol	Definition
		Table 11: Definitions of Nodes and resistances in the Pulse Width modulator
1-2	$R1$	Trace Resistance, power node to MOSFET
2-3	$R2$	MOSFET on resistance plus trace to test point
3-4	$R3$	Trace Resistance, MOSFET to turret
4-5	$R4$	Wire resistance turret to feedthrough
5-6	$R5$	Feedthrough resistance
6-7	$R6$	Vacuum wire resistance, feedthrough to hub
7-8	$R7$	#32 wire resistance, hub to cone terminal
8-9	R_{CONE0}	Resistance, cone heater, at ambient temperature T0
9-10	$R9$	#32 wire resistance, cone terminal to hub
10-11	$R10$	Vac wire resistance, hub to feedthrough
11-12	$R11$	Feedthrough resistance
12-13	$R12$	Wire resistance feedthrough to turret
13-14	$R13$	Trace resistance, turret to star ground
14-1	V	7V power supply voltage, test connector
1-4,13-14	T_{PWB}	Temperature of the printed wiring board near the traces.
5-6,11-12	T_{CASE}	Case, or vacuum enclosure temperature
7,10	T_{HUB}	Hub temperature, side thermistor temperature
8,9	T_{CONE}	Operating Cone temperature, regulated to 30°C
All	T_0	Circuit temperature during the resistance measurements
Define	R_{TRACE}	R1+R3+R13
3-14	R_{TEST}	Loop resistance measured from the test connector at T_0
4-5,12-13	R_{JUMP}	R4+R12, jumpers, board to feedthroughs

In a simplified notation, the equivalent heater resistance is:

$$R'_H = \frac{(R1 + R2 + R3 + R4 + R5 + R6 + R7 + R_{CONE} + R9 + R10 + R11 + R12 + R12 + R13)^2}{R_{CONE} + (R7 + R9)/2}$$
<div align="right">3.1.2.1.3B</div>

It is understood in Equation 3.1.2.1.3B that each resistance is corrected by temperatures from telemetry. It is assumed here that half of the power generated in the #32 wire lead resistances, R7 and R9, flows to the cavity.

3.1.2.1.4   Data Numbers — *DN*

Data numbers D in bold are the phase-fundamental-filtered values as defined in Equation 3.1.2.1.1. The four sets of data numbers in equation 3.1.2.1.1 are:

DN_S are the transformed data numbers from observations of the Sun, while the transformed feed-forward data numbers are digitally commanded to be DN_F. In eclipse by the earth, TIM will make measurements of dark space. These dark measurements provide the offset knowledge for TIM's radiometric scale. DN_K are the transformed data numbers from observations of dark space, while the transformed feed-forward data numbers are digitally commanded to be DN_{FK}. The feedforward values need only be transformed once, on the ground. The observational values DN_S and DN_K need to transformed as a time series.

3.1.2.1.5   Solar Distance (Inverse Square) Correction — f_{AU}

This is the inverse square correction so that the measurements refer to the solar irradiance that would be seen at a distance of one astronomical unit (AU). This correction is described in section 3.1.5.

3.1.2.1.6   Doppler Correction — $f_{Doppler}$

This is the Doppler correction for the radial velocity of the satellite to the Sun and is described in section 3.1.5.

3.1.2.1.7   Shutter Waveform Factor — Ψ

Ψ is the complex transform of the shutter waveform as defined in 3.1.2.1.2. It is a phasor, calculated using the same Fourier transform algorithm as used on the data numbers. The real part of Ψ is within one ppm of $2/\pi$. The deviations from $2/\pi$ depend on the standard deviation σ of the derivative of the shutter rise-time, and the timing error, Δt in the 50% duty cycle. A parameterized model of the real part of Ψ is given by equation 3.1.2.1.7.

$$2/\pi \Rightarrow \frac{2}{\pi}\left(1 - \frac{\sigma^2\omega^2}{2} - \frac{\Delta t^2\omega^2}{8}\right) \qquad 3.1.2.1.7$$

The shutter transmission factor Ψ is very close to the nominal $2/\pi$. The measured Fourier transform of the shutter waveform is $\Psi = (1 - 2\times10^{-7} - 1257\times10^{-6}i)2/\pi$. The only large deviation from $2/\pi$ is essentially an out-of-phase (imaginary) component.

3.1.2.1.8   Entrance Aperture— A_P

A_P is the aperture effective area, corrected from the calibration temperature to the (regulated and measured) heat sink temperature.

$$A_P = A_{PCAL}\left(1 + 2\alpha_{Al}\left[T_{SINK} - T_{CAL}\right]\right) \qquad 3.1.2.1.8$$

where T_{SINK} is the sink temperature from housekeeping, T_{CAL} is the calibration temperature, and α_{Al} is the thermal expansion coefficient of aluminum. The parameters A_{PCAL} and T_{CAL} are not subject to change in flight, except by second guessing the ground witnesses.

3.1.2.1.9   Bolometer Absorption — $\alpha=1-\rho$

The cavity absorption α is one less the cavity reflection ρ at the center of the pointing field of view. The cavity absorption is averaged over the solar spectrum., Except for possible updates from the ground witness

program, duty-cycle corrections, or reflectance monitors, this value is assumed constant in time and fixed at the pre-launch calibration value.

The pre-launch calibration includes the variation of ρ with pointing offset. However, these variations, together with variations in the equivalence ratio, are calibrated in flight during cruciform scans and raster scans of the Sun.

3.1.2.1.10   Equivalence Ratio — Z_R/Z_H

The theory of nonequivalence is described in Hengstberger [1989]. The equivalence ratio is the ratio of electrical to absorbed radiant power that gives the same temperature at an ESR's thermistor. In our case, with phase sensitive detection at the shutter frequency, the equivalence ratio is the ratio of two complex thermal impedances. In Figure 22, we see that the thermal impedances $\mathbf{Z}_R$ and $\mathbf{Z}_H$ are the transfer functions to the thermistor from radiant and heater power, respectively. The symbols $\mathbf{Z}_R$ and $\mathbf{Z}_H$ in bold face denote the phasor transfer functions at the shutter fundamental frequency. The equivalence ratio is determined by pre-launch characterization.

The equivalence ratio is theoretically determined based on a parameterized model of the heat flow in the radiometer. The parameters of the model are experimentally determined, but their usage in the model is entirely theoretical. The model independently calculates the thermal impedances $\mathbf{Z}_R$ and $\mathbf{Z}_H$ and then divides the complex number $\mathbf{Z}_R$ by the complex number $\mathbf{Z}_H$. Using thermal transfer theory, one calculates the thermistor response from a unit power input at a general position $\vec{X}$ on the bolometer cavity. The ratio of temperature response to power input at position $\vec{X}$ is the Green function impedance $Z(\vec{X})$. Given the normalized distributions $f_R(\vec{X})$ and $f_H(\vec{X})$ of absorbed radiation and heater power, we can calculate the equivalence ratio.

$$\frac{Z_R}{Z_H} = \frac{\int f_R(\vec{X}) Z(\vec{X}) d^3 \vec{X}}{\int f_H(\vec{X}) Z(\vec{X}) d^3 \vec{X}} \qquad\qquad 3.1.2.1.10$$

3.1.2.1.11   Servo Loop Gain — G

The servo open-loop gain $\mathbf{G}$ is the end-to-end complex gain of the control loop at the shutter fundamental. The loop gain is known from circuit analysis and pre-flight calibrations, but will be periodically re-calibrated in flight. A test amplitude $\mathbf{DN_{FTEST}}$ is added to the loop by ground command at the feed forward junction as shown in Figure 22. The fundamental response at the output is $\mathbf{DN}_{TEST}$ and the loop gain is calculated as:

$$\mathbf{G} = -1 + \frac{\mathbf{DN}_{FTEST}}{\mathbf{DN}_{TEST}} \qquad\qquad 3.1.2.1.11$$

3.1.2.1.12   Field of View (FOV) Correction – $f_{FOV}(\theta,\phi)$

The sensitivity of TIM depends on the location of Sun within the instrument field of view, given by pointing angles θ and ϕ. The field of view factor $f_{FOV}(\theta,\phi)$ in the denominator of the measurement equation is equal to one on axis, and is used to transfer the on-axis characterization to the actual solar position within the FOV. Although we determine the variation of response vs. the pointing angles in pre-launch tests, the most accurate data come from the periodic cruciform and raster scans in flight. Since the pointing precision of the SORCE spacecraft is sub-arc minute and the basic noise of TIM is < 1 ppm, we expect that the empirical method will add little uncertainty to the measurements.

For TIM and SIM, the sensitivity to pointing effects is actually in α, $\mathbf{Z}_H/\mathbf{Z}_R$, and the cosine-theta aperture factor. These individual effects are accounted for by the single correction factor $f_{FOV}(\theta,\phi)$.

3.1.2.2 Spectral Irradiance Conversion — SIM

The optical, electrical, and thermal analyses of the SIM instrument can be combined to give the radiometric measurement equation using the ESR as the primary detector:

$$E_\lambda = \frac{[V^2/MR_H]\mathbf{DN_{heater}}}{[f_{AU}][f_{Doppler}][f_{FOV}(\theta,\phi)]\mathbf{\Psi}]Tr(\lambda,f_{Degradation})][A_p(\lambda)\Delta\lambda][\alpha(\lambda)][F(\delta\lambda)][-\mathbf{G}/(1+\mathbf{G})][\mathbf{Z_R}/\mathbf{Z_H}]}$$

$$3.1.2.2.1$$

The terms in the numerator of Equation 3.1.2.2.1 give the measured Joule heating. The denominator shows the modifications that we must make to the solar spectral irradiance, E_λ, to balance the equation. These terms represent in-flight correction factors and pre-flight calibration characterization parameters. The description of the SIM ESR follows the notation of the TIM ESR. The quantities in equation 3.1.2.2.1 that are in bold text are phasor quantities and quantities in plain text are scalars or measured time series quantities.

3.1.2.2.1 Joule Heating Terms — V^2/MR_H

The substituted electrical power is proportional to the duty cycle and the V^2/R power. Equivalently :

$$V^2/(M\,R_H) = HeaterPower/DataNumber \qquad M=64000 \qquad 3.1.2.2.2$$

where V is the in-flight precision voltage standard, and R_H is the effective heater resistance including lead corrections. The integer 64000 assumes operation at 100% duty cycle.

DN_{heater} represents the Fourier transform of the raw data numbers filtered to include only the fundamental term. The phase sensitive detection method described in Section 3.1.2.1.1 for the TIM instrument is applied to the SIM ESR measurement as well.

3.1.2.2.2 Solar Distance Correction — f_{AU}

The solar distance correction is the inverse square correction of the irradiances to one AU. See section 3.1.5 for details.

3.1.2.2.3 Doppler Correction — $f_{Doppler}$

The Doppler correction, f_{AU}, corrects for the radial velocity of the satellite to the Sun. To account for the Doppler effect in the spectrum, a correction to the measurement equation is made for both wavelength and amplitude, see section 3.1.5 for details.

For spectral irradiance, $1-\beta$ is a 23 ppm correction if the spacecraft is moving 7 km /s. This corresponds to an immeasurably small wavelength shift in the focal plane. For example, at 500 nm where the dispersion is 0.04 mm/nm, the moving and rest focal plane positions will differ by 1×10^{-6} mm; this is to be compared to the positioning accuracy of the prism drive, which is 3×10^{-4} mm

3.1.2.2.4 Shutter Waveform correction—Ψ

The shutter waveform factor, Ψ, is a phasor and is parameterized the same way as the TIM shutter (see Section 3.1.2.1.7).

3.1.2.2.5 Prism Transmission — $Tr(\lambda,t)$

The prism transmission, $Tr(\lambda,f_{Degradation})$, is a function of wavelength, and is changed by the gradual exposure to hard solar radiation over time, $f_{Degradation}$. This exposure is expected to be small (<0.5%) owing to the radiation hardness of Suprasil 300 and contamination control. The prism transmission appears as a

first order term in equation 3.1.2.2.1 so the change from the preflight prism transmission must be measured explicitly during the course of the mission. This topic is described in section 4.1.2.2.

3.1.2.2.6   Entrance aperture spectral bandwidth product — $A_P(\lambda)\Delta\lambda$

Entrance aperture spectral bandwidth product, $A_p(\lambda)\Delta\lambda$, is derived from two terms. $A_P(\lambda)$ is the entrance slit effective area at wavelength λ, corrected for slit temperature and diffraction.

$$A_p(\lambda)=A_{pcal}(\lambda)\{1+2\alpha(T_{slit}-T_{cal})\} \qquad 3.1.2.2.6$$

T_{Slit} is the temperature of the entrance slit, T_{cal} is the calibration temperature, and α is the thermal expansion coefficient of the slit material. The net effect of diffraction is to decrease the effective slit width by 3.242λ. This topic is discussed by Lawrence, *et al.* [1998].

The resolution of the instrument at λ is derived from the optical properties of the prism, the geometry of the spectrometer, and the entrance/exit slit widths. The dispersion of the instrument, *disp*, is given by:

$$disp = dx / d\lambda = f(dn / d\lambda)(d\theta / dn) \qquad 3.1.2.2.7$$

where f is the focal length, θ the prism deviation angle, and n the index of refraction. The index of refraction of fused silica is known to 30 ppm, and is expressed in the standard Sellmeier form [Malitson 1965]:

$$n^2 - 1 = \sum_{i=1}^{3} \frac{K_i \lambda^2}{\lambda^2 - L_i} \qquad 3.1.2.2.8$$

The K_i and L_i are experimentally determined constants of the material. The term $d\theta/dn$ can be calculated from the geometry of the prism, but owing to the spherical surfaces of the Féry prism, ray trace analysis is used to produce more accurate values.

The resolution can be calculated with knowledge of the widest slit width (either the entrance or the exit slit):

$$\Delta\lambda = slitWidth_{max} / disp \qquad 3.1.2.2.9$$

The actual instrument point-spread function and dispersion will be determined with atomic lamps and lasers with a beam divergence of ½°.

3.1.2.2.7   Bolometer Absorption — $\alpha(\lambda)$

Bolometer absorption, $\alpha(\lambda)$, is determined by the reflectance $\rho(\lambda)$ of the nickel phosphorous surface on the bolometer and the reflectance $r(\lambda)$ of the spherical mirror surrounding it. The fraction of light eventually absorbed by the bolometer is given by:

$$\alpha(\lambda) = [1-\rho(\lambda)]/[1-r(\lambda)\rho(\lambda)]$$

For the ESR, $1-\alpha$ varies from 600 to 1000 ppm with an uncertainty of 30 ppm.

3.1.2.2.8   Wavelength Shift Correction — $F(\delta\lambda)$

The ensemble wavelength correction, $F(\delta\lambda)$, is derived from all the known sources of spectral shift and stretch ($\delta\lambda$) and must be applied in data processing. The three principal sources of $\delta\lambda$ are spacecraft pointing errors, thermally induced changes in the location of optical components, and thermally induced changes in the index of refraction of fused silica. The spacecraft will provide ±0.5 arc-minute pointing knowledge, and wavelength errors induced by pointing can be modeled by prism ray tracing and preflight off-axis pointing measurements. The temperature of critical components (such as the CCD, the optical bench and the focal plane) will be monitored and used as correction factors in data processing. As mentioned in Section 2.3.2.1, the prism temperature is monitored and the index of refraction temperature coefficient applied to the wavelength scale. After these changes are made to the wavelength scale, a final comparison of the spectrum is made against a standard solar spectrum to check the validity of the derived wavelength scale.

3.1.2.2.9   Servo Loop Gain — G

The discussion in Section 3.1.2.1.11 applies to the SIM ESR electronics.

3.1.2.2.10   Equivalence Ratio — Z_R/Z_H

The discussion of Section 3.1.2.1.10 applies the SIM radiometer.

3.1.2.2.11   Field of View (FOV) Correction – $f_{FOV}(\theta,\phi)$

The discussion of Section 3.1.2.1.12 also applies to the SIM radiometer.

3.1.2.2.12   Photodiode Radiometric Equation

A radiometric measurement equation for each of the photodiodes can be written analogously to the ESR equation:

$$E_\lambda = \frac{\dfrac{20}{65536}(DN_{photodiode} - DN_{dark})}{f_{AU}\, f_{Doppler}\, f_{FOV}(\theta,\phi) Tr(\lambda, f_{Degadation})[A_p(\lambda)\Delta\lambda] F(\delta\lambda) G_{amp} S(\lambda,T,t)} \qquad 3.1.2.2.10$$

The photodiode detectors are not absolute detectors, and we will use the ESR to continuously measure their performance in flight. The absolute uncertainty budget for the SIM instrument depends on the ESR stability and calibration, not the photodiode calibration. The factors f_{AU}, $f_{Doppler}$, $Tr(\lambda, f_{\backslash Degradation})$, $[A_p(\lambda)\Delta\lambda]$, $F(\delta\lambda)$ have already been described in other parts of section 3.1.2.2. $DN_{photodiode}$ and DN_{dark} are the signal and background data numbers reported by the 16 bit analog-to-digital converter on the DSP unit. The factor 20/65536 gives the voltage corresponding to the least significant bit (305 µvolts). The transimpedance amplifier gain, G_{amp}, (units of volts/ampere) is measured preflight, and the temperature sensitivity is determined by the temperature coefficient of resistance of the feedback resistor ($\approx$ 50 ppm). $S(\lambda,T,t)$ is the radiant sensitivity of the photodiode in amps/watt and is a function of wavelength, temperature, and time. The n-on-p gate structure photodiode will cover the 200-600 nm region with a temperature coefficient of responsivity (TCR) of <0.25%/°C. The p-on-n photodiode is for the 400-1100 nm region with a TCR <0.25%/°C for 400-900 nm, <0.75%/°C for 900 to 1000 nm, and <1.5%/°C in the 1000 to 1100 nm regions. The InGaAs diode is for the 700 to 1700 nm region, and has a TCR <±0.1%/°C for 700 to 1550 nm, and <1.0%/°C for the 1550 to 1700 nm region. The temperature is monitored to ±0.04° on the photodiode ceramic chip carrier and will be used to correct the temperature dependence in data analysis. As mentioned in section 2.3.2.1, the ESR will be used to calibrate the long-term variations in the diode radiant sensitivity.

3.1.2.3   Spectral Irradiance Conversion — SOLSTICE

The basic equation for converting detector output counts to irradiance values is identical for both solar and stellar observations:

$$E_{AU}(\lambda) = \frac{C(\lambda,\tau,Dc,Sl)}{R_C(\lambda)\cdot f_{FOV}(\theta,\phi)\cdot A_{Entrance}\cdot \Delta\lambda \cdot Tr_{Filter1}(\lambda)\cdot Tr_{Filter2}(\lambda)\cdot f_{Degradation}(\lambda,\theta,\phi)\cdot f_{AU}\cdot f_{Doppler}} \qquad 3.1.2.3.1$$

$$C(\lambda,\tau,D,Sl) = \frac{S(\lambda)\cdot N(\tau)\cdot G_{PMT}(T,V) - Dc - Sl(\lambda)}{\Delta t} \qquad 3.1.2.3.2$$

where $C(\lambda,\tau,Dc,Sl)$ is corrected instrument count rate at wavelength λ, which is computed by correcting the observed detector signal counts ($S(\lambda)$) for nonlinearity (N) by applying a correction for detector electronic dead time (τ), dark count (Dc), and scattered light ($Sl(\lambda)$) and then dividing by the instrument integration period (Δt). The additional factor $G_{PMT}(T,V)$ accounts for changes in detector performance due to thermal and electrical system variations. $R_C(\lambda)$ is the instrument response function (sensitivity) at the center of the field of view, $A_{Entrance}$ is the area of the entrance aperture, and $\Delta\lambda$ is the spectral bandpass. $f_{FOV}(\theta,\phi)$ and

$f_{Degradation}(\lambda,\theta,\phi)$ are factors that correct for instrument sensitivity changes that are a function of viewing direction (θ,ϕ) and time-dependent degradation respectively. $Tr_{Filter1}$ and $Tr_{Filter2}$ are the transmissions of a pair of neutral density filters that attenuate the solar photon flux impinging upon the MUV detector. f_{AU} is a factor that normalizes the solar irradiance values to a mean solar distance of 1 AU and $f_{Doppler}$ is the Doppler factor that corrects for spacecraft orbital velocity.

3.1.2.3.1   Wavelength Calibration

Wavelength values for the observed detector counts, $S(\lambda)$, are computed using the standard grating equation

$$\lambda = d(\sin(\alpha) + \sin(\beta)) \qquad\qquad 3.1.2.3.3$$

where d is the grating groove separation and α and β are the angles of incidence and diffraction, respectively. Equation 3.1.2.3.3 can be applied to the SOLSTICE instrument geometry by rewriting it:

$$\lambda_{Solar} = 2d\sin(\theta_S)\cos(\phi_G/2) \qquad\qquad 3.1.2.3.4$$

$$\lambda_{Stellar} = 2d\sin(\theta_S + \varepsilon/2)\cos(\phi_G - \varepsilon/2) \qquad\qquad 3.1.2.3.5$$

$$\theta_S = \theta_S(0) + 0.00375^\circ \cdot M + \delta\theta_S(M). \qquad\qquad 3.1.2.3.6$$

In these equations, $\theta_s = (\alpha+\beta)/2$ is the grating rotation angle and $\phi_G = (\beta-\alpha)/2$ is the half angle between the diffracted and incident beams and has a constant value. ε is the pointing offset from the instrument optical axis in the plane of dispersion (the plane perpendicular to the diffraction grating grooves) measured in the same sense as α and β. The grating rotation angle, θ_s, is controlled by a precision mechanism equipped with a high-resolution angular encoder. During normal solar observations the grating rotates through 2048 discrete steps (M=0,2047) which are equal in size to 0.00375°. Step sizes for stellar observations are typically 10 – 20 times larger.

Values for the parameters in Equations 3.1.2.3.4 – 3.1.2.3.6 are determined during preflight calibration. Uncertainties in angular position arising from the grating rotation mechanism and encoder are less than 0.1 steps, that is $\delta\theta_S(M) < 0.0003°$. Uniform shifts in the preflight wavelength scale will likely occur during shipping and launch. These will be accurately determined before each instrument radiometric calibration is applied to the measurement (Section 4.1.1). Additional time-dependent changes may arise during flight from temperature-dependent distortions of the instrument optical bench (i.e. from temperature gradients across the instrument optical bench) and from a combination of defocus and pointing errors. The latter effect, which will be measured during preflight calibration, is expected to be negligible. A defocus of 0.1 mm and a pointing error of 1 arc minute results in an image displacement of 0.39 microns in the stellar focal plane. This is equivalent to a grating rotation of 0.0001° or about 0.028 steps. Wavelength shifts caused by optical bench distortion are also expected to be negligible. A 1° C lateral temperature gradient across the optical bench will introduce a grating rotation angle of 6×10^{-5} degrees or about 0.016 steps. Lateral temperature gradients, which are expected to be less than 5° C will be measured during the mission.

The SORCE SOLSTICE wavelength scale is required to be accurate to within 2.5% of a bandpass. During flight the parameters in Equations 3.1.2.3.4 –3.1.2.3.5 derived from preflight calibration will be corrected for shifts caused by launch, temperature gradients, and defocus/pointing. The resulting wavelength scale will then be compared to a standard solar wavelength scale to correct for second order effects. Each grating position of the corrected scale is expected to have an absolute accuracy of ±0.075 steps referred to the spectrometer focal plane. That is equivalent to an absolute accuracy ±0.0025 nm for the FUV configuration and ±0.005 nm for the MUV configuration. Based on models using UARS SOLSTICE observations, this accuracy will result in uncertainties no larger than 0.2% in the solar flux reported at a spectral resolution of 1 nm. An additional correction will also be applied to the wavelength scale to account for the Doppler shift introduced by spacecraft orbital motion, $\Delta\lambda_{Doppler}$. The magnitude of this correction is on the order of ±0.002 nm for the FUV and ±0.005 nm for the MUV.

3.1.2.3.2 Dark Correction

Dark signals from the photon counting photomultiplier tube detectors are expected to be relatively constant at 1-5 counts/second during most observations. This low level has negligible effect on the solar measurements, which typically produce count rates of 10^4–10^5 per second. On the other hand, for the stellar observations, even a few counts per second are important. Dark count rates will be monitored throughout the SORCE mission by looking to dark regions of space (see Table 7). Each stellar measurement is corrected with an "up-to-date" value of the appropriate dark rate. Dark counts can also rise to as much as a few thousand counts per second while the spacecraft is passing through in the South Atlantic Anomaly region (see Section 4.3.1) and data acquired during those times will be excluded from the data processing. UARS experience indicates that these can be measured in-flight with a precision of 10-15% $(\sigma_{Dc}=10.0$-$15.0)$.

3.1.2.3.3 Linearity Correction

The SOLSTICE detectors are photon-counting photomultiplier tubes. Because photon detection is a random process, which is approximated by Poisson statistics, the observed count rate from the detectors must be corrected for electronic dead time, τ. The relationship between C_O, the observed count rate, and C, the true arrival rate, is given by:

$$C = -\frac{1}{\tau}\ln(1 - C_O\tau)$$ 3.1.2.3.6

The relationship between C_O and C (for $C<<1/\tau$) can be approximated by

$$C \cong \frac{C_O}{1 - C_O\tau/2}.$$ 3.1.2.3.7

The nonlinearity correction, $N(\tau)=C/C_O$ in Equation 3.1.2.3.2, is applied to the observed signal count rate before subtracting Dark Counts and Scattered Light. τ is measured during the instrument preflight calibration. The design value for τ in the SOLSTICE instruments is 75 nanoseconds resulting in a worst-case dead time correction of $5 \times 10^{-3} = 0.5\%$ when the count rate is 1.6×10^6. UARS experience indicates that detector dead time can be characterized in the lab to 10%; therefore, the maximum uncertainty in irradiance resulting from uncertainty in the dead time correction will be 0.05%.

3.1.2.3.4 Temperature and Voltage-Dependent Gain Correction

The SOLSTICE photomultipliers operate at peak efficiency over a fairly broad range in ambient temperature T and in power supply voltage V. However, operational constraints (full sun periods, extended periods during which the instrument is off, low-battery conditions, etc.) do occasionally result in temperature or voltage extremes. The detector gain is characterized as a function of temperature and voltage both in pre-flight laboratory calibrations, and in regular (daily) in-flight fixed wavelength experiments.

Tests using engineering high voltage power supplies for SORCE show that they are stable to ±1 volt indicating that the voltage dependent term will be less that 0.1%. Photomultiplier tubes also exhibit changes in sensitivity as a function of photocathode temperature. Worst case temperature coefficients for CsTe and CsI, which occur at the long wavelength end of their operating range (320 and 190 nm respectively), are 0.5% per degree Centigrade. Thus, photocathode temperature must be measured to 0.2° C in order to correct the detector sensitivity to 0.1%.

That is, the overall voltage and temperature gain correction factor is a product:

$$G_{PMT}(V, T) = 1 - G_V(V) \cdot G_T(T)$$ 3.1.2.3.8

where $G_V(V)$ and $G_T(T)$ are polynomials or spline functions. Each of these two gain corrections is modeled as an independent polynomial or spline function in its varying parameter (temperature or voltage). These

corrections are both multiplicative, so they are not linearly independent, and care must be taken to ensure that the data used for determining the model parameters vary only in one independent variable (temperature or voltage, respectively). These gain corrections are assumed not to depend on wavelength, and in-flight calibration experiments are conducted at fixed wavelengths, in order to eliminate the spectral variability.

3.1.2.3.5   Entrance Slit Area, Spectral Bandpass, - Integration Time and Instrument Sensitivity

In principle, the derived solar and stellar irradiance (Equation 3.1.2.3.1) is inversely dependent on entrance slit area, spectral bandpass, and integration time. However, in practice, precise values for solar entrance aperture and bandpass, are not required for measuring *solar irradiance* because the instrument sensitivity is calibrated using *source irradiance standards*. In this case the solar irradiance conversion equation can be written as:

$$E_{AU}(\lambda) = \frac{C(\lambda, \tau, Dc, Sl)}{R'_C(\lambda) \cdot f_{FOV}(\theta, \phi) \cdot f_{Degradation} \cdot f_{AU}}$$
3.1.2.3.9

$$R'_C(\lambda) = \frac{C_{Std}(\lambda, \tau, Dc, Sl)}{E_{Std}(\lambda)} \cdot \Gamma(\Omega)$$
3.1.2.3.10

$R'_C(\lambda)$ is the instrument response in counts per second to an irradiance source which is aligned to the center of the instrument field of view, $(\theta, \phi) = (0,0)$, and whose output $E_{Std}(\lambda)$ is specified in units of radiant power per unit area per unit wavelength interval. $C_{Std}(\lambda, \tau, Dc, Sl)$ is the instrument count rate which has been corrected for nonlinearity, dark count, and scattered light. $\Gamma(\Omega)$ is a geometrical factor which accounts for differences in the instrument response to sources with different angular sizes:

$$\Gamma(\Omega) = \frac{\int_{\Omega Sun} f(\theta, \phi) d\Omega}{\int_{\Omega Std} f(\theta, \phi) d\Omega} \ .$$
3.1.2.3.11

Solar irradiance values derived from Equation 3.1.2.3.9 depend on the ratio $\Delta t_{Std}/\Delta t$ rather than Δt because integration time appears in both Equation 3.1.2.3.9 and Equation 3.1.2.3.10. Since both Δt_{Std} and Δt are derived from the instrument clock there is negligible uncertainty in their ratio. In any event, uncertainty in integration time depends on the design of the instrument clock and is typically less than 0.001% [Woods *et al*. 1993].

By using an irradiance standard to calibrate the SOLSTICE spectrometers, the derived solar irradiance values are independent of solar entrance aperture and bandpass. On the other hand, accurate values for the ratios of stellar to solar entrance aperture area, stellar to solar spectral bandpass, and integration times are essential for determining the ratio of stellar to solar irradiance. Techniques for measuring entrance slit areas and the ratio of solar to stellar exit slit width, which determines the bandpass ratio, are described by Woods *et al*. [1993]. Their results indicate that the solar entrance area and the ratio of the exit slit widths can be measured with an accuracy of about 0.1%

The derived solar and stellar irradiance (Equation 3.1.2.3.1) is inversely dependent upon instrument sensitivity or response, $R_C(\lambda)$. NIST irradiance sources provide the primary standards for determining instrument response. The primary standard for calibrating SOLSTICE instrument response is SURF III. FEL and Deuterium lamps provide a cross-check on the SURF results for wavelengths greater than 230 nm. All three standards allow a direct measurement of the product $R_{C-Std}(\lambda)A_{Entrance}\Delta\lambda$,

$$\frac{R'_C(\lambda)}{\Gamma(\Omega)} = R_{C-Std}(\lambda) \cdot A_{Entrance} \cdot \Delta\lambda = \frac{C_{Std}(\lambda, \tau, Dc, Sl)}{E_{Std}(\lambda)} \ .$$
3.1.2.3.12

Here, $R_{C-Std}(\lambda)$ is the response of the instrument to the specific source, measured with the source aligned to the center of the instrument field of view. $\Gamma(\Omega)$, the geometrical factor defined by Equation 3.1.2.3.11, must be computed in order to use the results from Equation 3.1.2.3.12 to derive the solar and stellar irradiance (Equations 3.1.2.3.9 and 3.1.2.3.1 respectively). For example, the Sun can be approximated as a

uniform disk with an angular diameter of 0.54° at 1 AU. On the other hand, irradiance standards developed by the National Institute for Standards and Technology (NIST) have a wide variety of angular sizes. The Synchrotron Ultraviolet Radiation Facility III (SURF III) is nearly a point source with an angular diameter of only 0.03° while the FEL and Deuterium lamps subtend angles of 0.3° x 1° and 0.3° x 0.3° respectively. In each case, the illumination factor must be measured for the irradiance source standard used to calibrate the SOLSTICE spectrometers.

There is an implicit correction factor to $\Gamma(\Omega)$ resulting from radiation that is diffracted past the SOLSTICE aperture stop by the solar entrance slit (Diffraction is negligible for the stellar entrance slit and for the F/800 SURF beam with either entrance slit.). The correction (increase) to the absolute solar irradiance varies from 1% at 115nm to 5% at 320nm.

3.1.2.3.6   Angular Response, and On-orbit Degradation

$f_{FOV}(\theta,\phi)$ is measured at SURF III by mounting the instrument on a precision rotary actuator in order to map the instrument angular response. These measurements and the known angular sizes of the Sun and irradiance standards are used to compute $\Gamma(\Omega)$. $f_{FOV}(\theta,\phi)$ is expected to be close to unity over the range of observing angles specified for the SORCE mission ($-0.05°<\theta,\phi<0.05°$). Simulations of the SORCE SOLSTICE instrument angular response indicate that $f_{FOV}(\theta,\phi)$ will change by less than 1% for a 0.1° change in instrument bore sight pointing. Experience with UARS SOLSTICE shows that shifts in the instrument bore sight as large as 0.05° may occur during launch. This will result in an uncertainty of ~0.5% in the beginning of life on-orbit values for $f_{FOV}(\theta,\phi)$. Additional uncertainty in the on orbit values for $f_{FOV}(\theta,\phi)$ will result from pointing errors. These will be smaller because SORCE SOLSTICE is equipped with real time solar and stellar position monitors that are accurate to 0.03°. The present estimate for overall uncertainty in $f_{FOV}(\theta,\phi)$ at the on-orbit beginning of life is ~0.6%. Changes in instrument angular response during flight are included in the $f_{Degradation}(\lambda,\theta,\phi)$ term in Equation 3.1.2.3.1. These are measured by rotating the spacecraft (and therefore, instrument) through narrow azimuth and elevation scans centered on the Sun. $f_{Degradation}(\lambda,\theta,\phi)$ is also verified during the SORCE mission by routine field-of-view maps using the stars and the offset pointing capability of the SORCE spacecraft. Angular scans with the UARS SOLSTICE indicate that the angular response of $f_{Degradation}(\lambda,\theta,\phi)$ should change by less than 1-2% per year and that the overall degradation should ~ 3-5% per year or less [Woods *et al* 1996]. Thus, tracking solar variability with a relative accuracy of 0.5% per year requires that $\sigma^2_{f_{Degradation}}$ (the uncertainty in $f_{Degradation}(\lambda,\theta,\phi)$) be measured with an accuracy better than 10-15%.

3.1.2.3.7   Scattered Light

Scattered light in each SOLSTICE instrument arises primarily from scattering at the diffraction grating, as well as from stray light caused by diffuse scatter from the instrument internal surfaces. Scattered light observed at wavelength λ is the difference of two terms. The first term is a convolution of the grating scattering function and diffuse scatter with the input signal and represents the energy scattered *into* wavelength λ from all other wavelengths. The second term is the fraction of light that is scattered *away from* λ into all other wavelengths.

$$Sl(\lambda) = Stray + \int S(\lambda') \cdot (G_{Scat}(\lambda - \lambda') + B)d\lambda' - S(\lambda) \cdot \int G_{Scat}(\lambda')d\lambda' \qquad 3.1.2.3.12$$

G_{Scat}, the grating scattering function, is the sum of a Lorentz profile and a constant background; B is the diffuse scattering function. The integral of G_{Scat}, represents the fraction of energy scattered away from wavelength λ into all other wavelengths.

G_{Scat}, and *B* are measured before flight for each grating using methods described by Woods *et al*. [1994]. *B* is also measured during flight by observing the instrument count rate at wavelengths below the detector window cutoffs and at the bottoms of strong absorption lines.

Scattered light corrections for UARS SOLSTICE are typically 1 to 2 % [Woods *et al* 1996]. That instrument used holographic and classically ruled gratings for the MUV and FUV channels respectively. SORCE SOLSITCE will employ holographic gratings for both wavelength ranges. Thus, conservative estimates for the SORCE scattered light corrections are 1 to 2% for the MUV and FUV wavelength ranges respectively. Based on UARS experience, the uncertainty in the scattered light correction is estimated to be 20%.

3.1.2.3.8   Solar and Stellar Signal

The SOLSTICE optical system is designed to produce detector output count rates in the range 10^3-10^5 per second for solar observations and 10-10^3 per second for bright stars. For the Sun, σ_S (Random uncertainties in signal measurements) are calculated from the square root of the number of observed counts accumulated over 4 orbits (σ_S=1% requires 10^4 counts). These are corrected for nonlinearity ($N(\tau)$) and gain ($G(V,T)$) as described in Sections 3.1.2.3.3 and 3.1.2.3.4. Corrections for $N(\tau)$ and $G(V,T)$ are typically 1-2%; therefore an uncertainty in these correction factors of 5% results in a 0.05-0.1% uncertainty in irradiance. Tests with engineering components indicate that we can determine these parameters to 10% so that the overall $\sigma_M \sim$ 0.1-0.2% (Equation 3.1.7.3.2). σ_S for the stars is also calculated from the square root of the number of counts accumulated at 18 standard stellar wavelength positions. These must be corrected for gain, but nonlinearity is negligible for stellar counts.

3.1.2.3.9   Filter Transmission

Terms for the transmissions of the filters used to attenuate the long-wavelength light for solar observations are explicitly shown in Equation 3.1.2.4.1. $Tr_{Filter1}$ and $Tr_{Filter2}$ are each measured once per day with an accuracy of 0.25% as described in Section 2.3.3.

3.1.2.4   Spectral Irradiance Conversion — XPS

The solar XUV irradiances will be derived from the set of 9 XUV photodiodes with thin film metal filters within the SORCE XPS. The XPS provides spectral coverage from 0 to 35 nm with 5 nm spectral resolution. The calibrations for the XUV photodiodes include current calibration of the detector electronics and photometric calibration of the photodiodes as a function of wavelength. The current calibration of the detector electronics is performed over a range of temperature. The detector electronics gain has very small changes with temperature, but it does have a measurable change in offset with temperature, amounting to about 1% over the range -10 °C to +50 °C.

The current output from the photodiode is a combination of dark, visible light (VIS) and soft x-ray signal (XUV) as follows:

$$I_{Total} = I_{XUV} + I_{VIS} + I_{Dark}$$
$$= \int_{XUV} S(\lambda) \cdot E(\lambda) d\lambda + \int_{VIS} S(\lambda) \cdot E(\lambda) d\lambda + I_{Dark} \qquad 3.1.2.4.1$$

where I is current, S is sensitivity, and E is solar irradiance. For the fused silica window chosen for the measurement of the visible signal, all wavelengths above 160 nm are used as the VIS region. Therefore, the XUV region actually extends up to 160 nm. However, the diode/filter combinations are most sensitive to the XUV below 35 nm and to the "true" visible light when the fused silica window is used.

When a fused silica window is in front of the photodiode to measure only the visible light contribution, the diode signal is:

$$I_{Window} = \int_{VIS} S(\lambda) \cdot E(\lambda) \cdot T(\lambda) d\lambda + I_{Dark} \qquad 3.1.2.4.2$$

where T is the transmission of the fused silica window, being about 0.96 throughout the visible region.

Because the transmission of the fused silica is essentially independent of wavelength in the visible region, equation 3.1.2.4.2 can be simplified by moving the transmission term out of the integral. Therefore, the I_{VIS} term in equation 3.1.2.4.1 can be replaced with a measurement as follows.

$$I_{Total} = \int_{XUV} S(\lambda) \cdot E(\lambda) d\lambda + \frac{I_{Window} - I_{Dark}}{T} + I_{Dark} \qquad 3.1.2.4.3$$

The transmission of the fused silica windows are tracked by a bare silicon photodiode for each solar measurement sequence. Therefore, the transmission parameter, T, is also derived from two measurements with the bare photodiode, B, as follows.

$$T = \frac{B_{Window} - B_{Dark}}{B_{Total} - B_{Dark}} \qquad 3.1.2.4.4$$

A corrected current, I_{Cor}, is defined to isolate the solar XUV irradiance information for the analysis as follows.

$$\begin{aligned} I_{Cor} &= I_{Total} - \frac{I_{Window} - I_{Dark}}{T} - I_{Dark} \\ &= \int_{XUV} S(\lambda) \cdot E(\lambda) d\lambda \end{aligned} \qquad 3.1.2.4.5$$

To invert this equation for irradiance, a weighted average sensitivity $\langle S \rangle$ is defined as

$$\langle S \rangle \equiv R \cdot A = \frac{\int_{XUV\Delta\lambda} S(\lambda) \cdot E(\lambda) d\lambda}{\int_{XUV\Delta\lambda} E(\lambda) d\lambda} \qquad 3.1.2.4.6$$

where R is the responsivity, A is the area of the diode aperture, and $XUV\Delta\lambda$ is the bandpass for the diode. Then, the irradiance is calculated as

$$E_{XUV} = \frac{I_{COR}}{R \cdot A \cdot f_{AU} \cdot f_{Degradation} \cdot f_{FOV}(\theta, \phi) \cdot f_{Doppler}} \qquad 3.1.2.4.7$$

where F_{AU} is the correction to one astronomical unit (AU) and $f_{Degradation}$ is the correction for degradation, as done for the other SORCE instruments. Note that the E_{XUV} is in units of irradiance (W/m^2) and not spectral irradiance (W/m^2/nm). $\langle S \rangle$ is determined by averaging $\langle S \rangle$ values using a variety of solar XUV irradiance models and reference spectra. The distribution of $\langle S \rangle$ with different models is about 5%; this uncertainty is acceptable because the amount of solar XUV variability is larger than a factor of two.

The wavelength scale for the XPS is determined from the pre-flight sensitivity calibrations. These calibrations establish the spectral bandpasses for each XUV photometer. Table 12 lists the thin film filters and wavelength intervals for the current design of the XPS. The sensitivity and expected solar signal for these photodiodes are shown in Figure 20.

Table 12: List of Photodiode Filters and Their Bandpasses			
Diode Filter	Filter Thickness (Å)	Solar Signal Levels nA / cm^2	XUV Bandpasses Used for Irradiance Analysis (nm)
Ti/C	2500/500	0.2-1.4	0-6
Ti/Zr/Au	200/2000/1000	0.2-0.7	6-12
Ti/Si/Zr	60/1000/2000	0.8-2.6	12-20
Al/Sc/C	2000/500/500	2.2-8.6	17-25
Al/Cr	2000/1000	0.6-2.4	25-35

The currents referenced in the preceding equations are not actually telemetered by the instrument. Rather, the XPS electronics convert the photometer current to frequency and then counts those pulses. Except for the high end of the voltage-to-frequency range, the conversion is very linear. So the current can be expressed as a simple linear equation with the count rate, C.

$$I = a + b \cdot C$$

or

$$I' = I - I_{Dark} = b \cdot (C - C_{Dark}) \qquad\qquad 3.1.2.4.8$$

The conversion factor, b, from the count rate to current is also calibrated over temperature. Because all of the measurement parameters in equation 3.1.2.4.6 already have the dark current removed, the parameter I' is introduced, which is only sensitive to the gain of the detector electronics and not to the offset of the electronics.

3.1.3   Averaging to 6-Hour Time Resolution

For each 6-hour time interval centered at time t (e.g., 0 hours UT ± 3 hours), a fixed number n of corrected calibrated irradiance/wavelength/time triples (and their uncertainties) at each instrument grating position are collected in buffers. The value of n will be the nominal number of data sets completed during a 6-hour period. For example, if 1.5 scans are normally completed in a 90-minute orbit, an appropriate value for n is 6. The n triples buffered at each grating position are those nearest in time to t. Note that not all n triples may fall in the 6-hour window--if only four measurements happened to have been made at some grating position, then two of the buffered triples for that grating position would be from prior or later scans.

These buffered data are processed to an instrument-resolution 6-hourly mean by fitting (least-squares) a cubic b-spline [de Boor, 1978; Lawson & Hanson, 1974] with a standard node spacing corresponding to the instrument wavelength resolution. Before this fit, outliers may be rejected by median filtering. If all systematic uncertainties have been identified and properly corrected the data should be normally-distributed, without outliers. However, it is possible that measurements taken, for example, at extremes of temperature or power-supply voltage regulation, may not be adequately corrected, resulting in outliers in either irradiance or wavelength. If no outliers in irradiance or wavelength are identified, then outliers in time may also be rejected, to help restrict the data to the nominal 6-hour time period. Median filtering may be more or less aggressive, but at least one data triple at each grating position will always remain (the b-spline algorithm requires this). The median filtering parameters, as well as the number of data excluded for each filter criterion, are recorded and tracked by data surveillance tools and reports.

The irradiance and wavelength uncertainties are fully propagated by the least-squares algorithm to the spline coefficients, and each spline coefficient also has a mean time and time uncertainty. Whenever the resulting spline model is later evaluated or integrated, the uncertainties (and times) of the spline coefficients are correctly propagated to the result. If some grating positions were missed during this 6-hour time period, and were "filled" by measurements from prior or later scans, the mean time (and time uncertainty) of the spline evaluation or integration will show this. An attractive feature of the b-spline function is that the coefficients have local support, so that if there are any fill data, their effect on the model is limited to a very narrow wavelength region.

The instrument-resolution 6-hourly mean consists of the spline coefficient (irradiance)/time pairs, and their uncertainties (that is, four floating-point numbers for each spline node).

Non-parametric data reduction methods such as locally-weighted smoothing functions (e.g., "LOESS" [Cleveland, 1985]) may be used by SORCE analysts to monitor and validate the spline models, but the spline model product has several distinct advantages over such non-parametric methods. First, it is produced on a standard wavelength scale at a standard wavelength resolution. (The LOESS method, as it is commonly

used, would give a variable and unpredictable wavelength scale *and* resolution.) Second, the spline model is analytic – it can be evaluated, integrated, and differentiated analytically, with uncertainties fully propagated analytically. For example, the spectral slope is required in order to propagate wavelength uncertainties; this is difficult to do with a non-parametric method.

3.1.4 Binning into Desired Spectral Resolution

Lower-resolution integrated spectra are easily obtained from the spline coefficients by either analytical or numerical integration over a given wavelength scale. In either case, the uncertainties and fill fractions are propagated to these integrated irradiances. The SOLSTICE spectrometers will be integrated to 1-nm resolution, and the SIM to three or four different resolutions — with differing wavelength coverage — at 1-nm, 2-nm, 3-nm, or 5-nm resolutions. An alternative presently under consideration is to provide the SIM integrations on one or two standard wavenumber (inverse wavelength) intervals.

3.1.5 Solar Distance And Velocity (Doppler) Corrections

The total solar irradiance and the spectral irradiances are to be reported as seen from a distance of one astronomical unit (AU) from the center of the Sun, and at zero line of sight velocity with respect to the Sun. The observed irradiance follows an inverse square law so the actual distance between the instrument and the center of the Sun must be known in astronomical units. We define an inverse square correction factor to 1 AU:

$$f_{AU} = \left(\frac{R_{AU}}{R_{Sun}} \right)^2 \qquad \text{3.1.5A}$$

where R_{AU} is one astronomical unit and R_{Sun} is the distance between the instrument and the center of the Sun. The factor f_{AU} appears in the denominator of the measurement equations and varies about ±3.4% annually.

The line of sight velocity is the rate of change of $dR_{Sun}/dt \equiv \dot{R}_{Sun}$. There are four effects on the irradiance. The observable effects are first order in the ratio of line of sight velocity to the speed of light, c.

We define the first order Doppler parameter $\beta \equiv \dot{R}_{Sun}/c$; which can be as large as ±25 ppm. The *relativistic* terms of order β^2 are < 0.7 ppb and are thus negligible. When we approach the Sun, β is negative and:

a) The incoming photons have more energy by a factor $(1-\beta)$.

b) The instrument collects photons at a rate larger by a factor $(1-\beta)$.

c) The wavelength intervals $\Delta\lambda$ of the incoming spectra are decreased by a factor $(1-\beta)$.

d) The wavelengths λ of each spectral feature are decreased by a factor $(1-\beta)$.

We define a generic Doppler correction factor

$$f_{Doppler} \equiv (1 - \beta) \equiv 1 - \dot{R}_{Sun}/c . \qquad \text{3.1.5B}$$

The total solar irradiance as measured by TIM is then corrected by the factors a) and b) to be:

$$E_0 = E_{Observed}/f_{Doppler}^2 . \qquad \text{3.1.5C}$$

The spectral irradiances per *wavelength* for SIM and SOLSTICE are corrected by the factors a-c to be:

$$E_{0\lambda} = E_{\lambda Observed}/f_{Doppler}^3 . \qquad \text{3.1.5D}$$

The spectral irradiances per *wavenumber* for SIM and SOLSTICE are corrected by the factors a-c to be:

$$E_{0\upsilon} = E_{\upsilon Observed}/f_{Doppler} . \qquad \text{3.1.5E}$$

47

The observations are interpolated and stored into standard (zero velocity) spectral bins λ_0 that are different, by effect d), from the instrument wavelength setting.

$$\lambda_0 = \lambda_{Instrument} \; f_{Doppler} \qquad\qquad 3.1.5F$$

The Earth's distance to the Sun and the velocity of the Earth relative to the Sun are both obtained from the "VSOP87" harmonic series [Bretagnon & Francou, 1988] based on the JPL Dynamic Ephemeris integrations "DE200" [Standish, 1982 and Standish, 1990]. For both position and velocity, the VSOP87 approximations have uncertainties on the order of 10 parts per billion (ppb).

The spacecraft position and velocity relative to the Earth are obtained from NORAD orbital elements, and are accurate to better than 1 km and 0.1 km/sec, respectively. The 1 km position NORAD uncertainty maps into 7 ppb uncertainty in the inverse square factor (3.1.5A). The 0.1 km/sec velocity uncertainty maps into 333 ppb uncertainty in the Doppler factor (3.1.5B).

3.1.6 Degradation Correction

3.1.6.1 General Discussion

The sensitivities of all instruments on SORCE are assumed to degrade as the mission progresses. There is a general assumption, but no guarantee, that the degradation will be small (much less than 1% per year for TIM and SIM, and perhaps up to a few percent per year for SOLSTICE and XPS) and that the sensitivity will monotonically decrease with time. There is also a basic assumption that a primary cause of the decreased sensitivity is related to the exposure to the harsh radiation environment from the Sun, although other changes that are strictly time-dependent, or aging effects, must also be considered. Changes in the instrument that may increase sensitivity can not be ruled out, and the degradation analysis does not preclude this condition. That is, the analysis is open to the possibility that aging effects improve sensitivity, or that radiation and exposure may in fact "scrub" surfaces and improve their throughput.

The science team, and in particular the instrument scientists, will examine all relevant information, including in-flight calibrations, comparisons with other observations, and alternate forms of data validation to derive appropriate degradation corrections. There will not be a preordained algorithm for determining degradation with time. The UARS SOLSTICE experience indicates that this process will take on the order to three to four months, but will then be an on-going process throughout the mission.

The SOLSTICE spectrometers rely on the stellar observation program to deduce changes in the instrument sensitivity, and this degradation analysis is discussed in section 3.1.6.2. The concept of duty-cycling is also considered in the case of the XPS, the TIM, and the SIM. One channel, the normal channel, is exposed to solar radiation on a regular basis, with the second channel held in reserve and exposed at a much lower duty cycle, say 1/100 of the exposure of the normal channel. With the assumption that exposure-dependent degradation will proceed proportionally faster for the normal channel, an exposure-dependent model of degradation is developed. This discussion follows in section 3.1.6.3.

Finally, additional insight into the instrument degradation can be attained through cross-calibration and intercomparison with other instruments. This is also related to the validation process considered in section 4.2.

3.1.6.2 Analysis Based on Stellar Observations

The SORCE SOLSTICE instruments routinely observe stars through the same optics and detectors used for the solar measurements. The selection of stars and the wavelengths observed are flexible decisions made in the "daily" experiment planning process. An observation of a single star at a given wavelength is analyzed as an independent measurement, and that "data point" may or may not be included in the analysis of the instrument degradation. The UARS SOLSTICE originally started with about thirty stars, although as the analysis proceeded the list was reduced to eighteen. Each UARS channel observed at eighteen different

wavelengths with a wavelength separation of roughly 9 to 10 nm. The on-going analysis of the UARS data has resulted in adjustments and continued improvements in the observing routines. The plan for SORCE will follow the best observing sequences and analyses established during the UARS mission.

Figure 24 provides an example of the UARS stellar observations at 153 nm for one star, α Canis Majoris. The break in the curve in June of 1992 coincides with a four-week period during which the UARS SOLSTICE was turned off while a spacecraft anomaly was resolved. The best fit to these stellar data are exponentials with finite asymptotes, fit piece-wise for the various periods. Actually, all valid stellar observations at the 153 nm wavelength are simultaneously fit to the exponential using a multivariate least-squares algorithm. Similar analyses will be conducted for the SORCE SOLSTICE data.
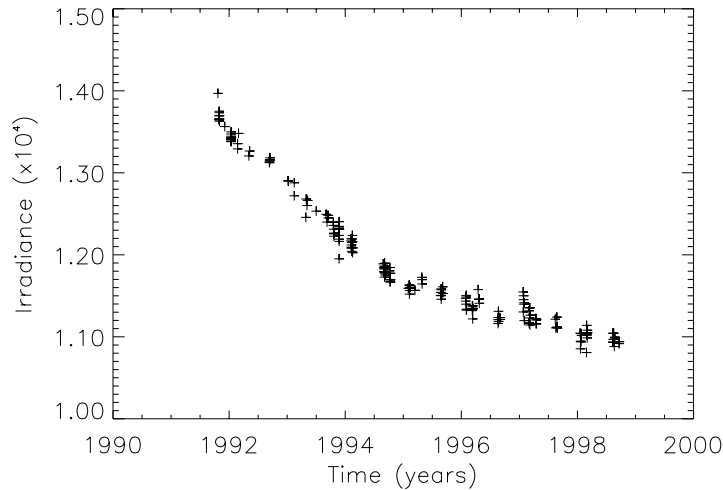
Figure 24: UARS SOLSTICE α Canis Majoris Stellar Irradiance at 153 nm

3.1.6.3 Analysis Based on Duty-Cycle

Unlike SOLSTICE, the XPS, TIM, and the SIM do not allow for direct comparison of the Sun to stars. This is true for the XPS because the stellar flux is far too low for the comparison, and the TIM and SIM because the solar/stellar comparison is only good to the 0.5% level and the requirement on measurement precision exceeds this by at least an order of magnitude. One technique used to understand instrument degradation for these three instruments is to have completely independent instrument channels, to use each channel with a varying duty cycle, and then to compare their simultaneous observations of the Sun. Similar diagnostic methods are used by the ACRIM instruments, by the UARS SUSIM, and by others.

The degradation in the instruments is assumed to be primarily dependent on the exposure of the optics and detectors to solar radiation. If the exposure times are dramatically different, say one to one hundred, the ratio of the measurements will change with time.

Unraveling details in the time-dependent degradation is a challenging problem, and will require refinements throughout the mission. The SORCE science team, particularly the XPS, TIM, and SIM instrument scientists, will devote considerable effort toward these analyses. A model of the degradation will be developed that will correct each observation. A proposed initial model for changes in signal, ΔS, due to degradations might have the form.

$$\Delta S = D_1 e^{-k t_s} - D_2 t_s - D_3 t$$

where t is time t_s is exposure time. This parameterization assumes some linear degradation with age and with use (exposure to the Sun), and would apply, for instance, to materials and coatings used on the optics.

Additionally, the proposed form allows for rapid, exponential degradations during initial use, such as might be expected as surface contaminants polymerize. We expect to keep these corrections small by paying utmost attention to contamination and by selecting materials (e.g., NiP) less sensitive to deterioration.

During the later stages of the mission, we expect the degradations to be mainly linear with exposure, and we currently plan duty cycles between the primary and diagnostic channels of about 100:1. Initially, to characterize the exponential parameters, more frequent measurements with the diagnostic channel(s) will be made.

We are aware that any correction parameterization that we use initially may need evaluation and modification during the mission. Major solar storms may affect the accuracy of the electronics or the detectors. Unexpected thermal changes may cause offsets needed in the analysis of certain data. Infrequent corrections such as these, which may take the form of discontinuous changes rather than parameterized functions, may be deemed necessary by comparing redundant ESRs.

3.1.7 Uncertainty Estimates (error analysis)

All calculations which involve physical quantities with uncertainties will incorporate the correct propagation of those uncertainties into the calculated results, on the assumption that the measurement uncertainties are independent. Moreover, the assumption of independence of measurement uncertainties will be subject to validation by separate and on-going statistical analyses, as a component of the quality assurance plan (section 4.2.5 below).

3.1.7.1 TIM Uncertainty Analysis

Since TIM is a primary radiometer, its uncertainty in measuring the Total Solar Irradiance (TSI) is estimated as the root sum square of the individual uncertainties of the components of the measurement Equation 3.1.2.1.2. We will consistently quote "relative standard uncertainties" in ppm (10^{-6}). "Relative" refers to fractional uncertainty, standard means standard deviation, σ, and uncertainty means the lack of knowledge of the parameters and hence of the determined irradiance. The uncertainty budget for the design of TIM is presented in Table 13.

Table 13: TIM Uncertainty Budget Goals		
	Size of the effect, PPM	Uncertainty, PPM
Inverse Square	+33116,-33764,188 orbit	5
Doppler	43	5
Shutter Waveform	100	10
Aperture	1,000,000	60
Optical Absorber	100	20
Equivalence ratio, Z_H/Z_R	100, AC	60
Servo Gain	3000	10
Standard Volt + DAC	2,000,000 (V^2)	10
Standard Ohm + Leads	1,000,000	10
Dark Signal	1800	10
Total RSS		**90**

For a squared factor such a V^2, the relative uncertainty in the irradiance is $2\delta V/V$. For the equivalence ratio and other factors, one must propagate the uncertainties in the parameters of each model. Table 14 summarizes in some detail the propagation of parameter and measurement uncertainties to the final uncertainty in the irradiance.

In the characterization of TIM, the equivalence ratio is the only quantity that comes from theory rather than experiment. Section 3.1.2.1.10 describes the theory of the overlap integrals need to calculate the ratio. To calculate the uncertainty in the ratio, one propagates uncertainties in the parameters of the model through equation 3.1.2.1.10; and some early examples of such calculations are shown in Figure 25.

Although the equivalence is calculated, rather than measured, we will measure some of the parameters. We will also measure the relative equivalence ratio vs. shutter frequency.

Table 14: Propagation of Uncertainties for TIM. Absolute Uncertainties in ppm					
Ephemeris Correction	Value	Uncertainty		Net ppm	Notes & Comments
1 AU, delta R, inverse square	1.50E+08	75	km	1.00	published 3 sigma
velocity: Doppler	3.00E+05	0.1	km/sec	0.67	published 3 sigma
δEphemeris				**1.20**	
Shutter waveform, Y					
Shutter frequency	0.01	0	Hz		
Rise time	7	1	msec	0.0023	
Delay	20	2	msec	0.1579	
Timing Jitter and drift	0	2	msec	0.00	
Leakage fraction		1	ppm	1	goal
Digital Timing error		1	μsec	0.00	
δShutter				**1.01**	
Aperture, Ap					
Ronchi Ruling scale error		5	ppm	10	
CCD scale transfer error		20	ppm	28.28	CCD imperfections
Aluminum Expansion coefficient	23	2	ppm/K	1	
Temperature transfer uncertainty		0.1	K	4.6	
Nonlinearity Correction	1000	50	ppm	50	coupled to halo
Point spread function, halo effect	1000	50	ppm	50	characterize better
Omission of internal baffles		10	ppm	10	estimate
δAperture				**78**	
Cavity Optical Absorption, α	999950		ppm		
Cavity Optical Reflection, 1-α	50		ppm		
Geometry overlap integrals		10	%	6	
Reflectance standard		2	%	1.2	
Diode linearity		1	%	0.6	
Amplifier scale tracking		2	%	1.2	
Scattered Light		5	%	3	
Average over solar spectrum		10	%	6	
Pointing corrections	?	20	ppm	20	estimate
δAbsorption				**22.0**	
Equivalence Ratio, Z_R/Z_H					
Monte Carlo calc on heat flow		20	ppm	20	See Figure 25
Heater length, "uncovered" end	220	0.01	cm	45.45	Cover with Au
δEquivalence Ratio				**49.66**	
Standard Volt					
Voltage	7.1		V		
HP3458A + Fluke + NIST		2	ppm	2	
5 year stability against witness		5	ppm	5	
Thermocouple voltages	1	1	μV	0.28	
MOSFET droop, DAC non-linearity	6	3	ppm	3	
Coupling, stray electronic		6	ppm	6	

δStandard Volt				**8.61**	
Standard Ohm (heater)	520		Ω		
HP 3458A + Tegam SR104		5	ppm	5	
Lead resistances	0.062	0.01	Ω	19.23	Resolution is 1 mΩ
Lead Temp. transfer from calibration		2	K	1.62	
TCR of leads	0.68		%/K		
TCR of heater	15	3	ppm/K		
Heater Temp., thermistor aging	30	0.5	deg C	1.50	Cone is regulated
Aging against witnesses		5	ppm	5	estimate
δStandard Ohm				**20.61**	
Dark Signal Correction	1800	1	ppm	1	uncertainty is noise
Temperature uncertainties, short term		0.3	deg C		
Sensitivity to shutter temperature	0.5		ppm/K		VF*4εσT^4
Uncertainty from shutter temperature			ppm	0.15	
Sensitivity to heat sink temperature	10.6		ppm/K		VF*4εσT^4
Uncertainty, heat sink temperature			ppm	3.18	
δDark Signal				**3.34**	
Open Loop Servo Gain G		200	ppm		
Gain value	30				
Matching of Feedforward signal		15	%		
δClosed Loop Gain, G/(1+G)				1.00	
Miscellaneous					
Scattered light	100	10	ppm	10	Spec to be met
Total Uncertainty				**97.39**	**ppm, 1 σ**
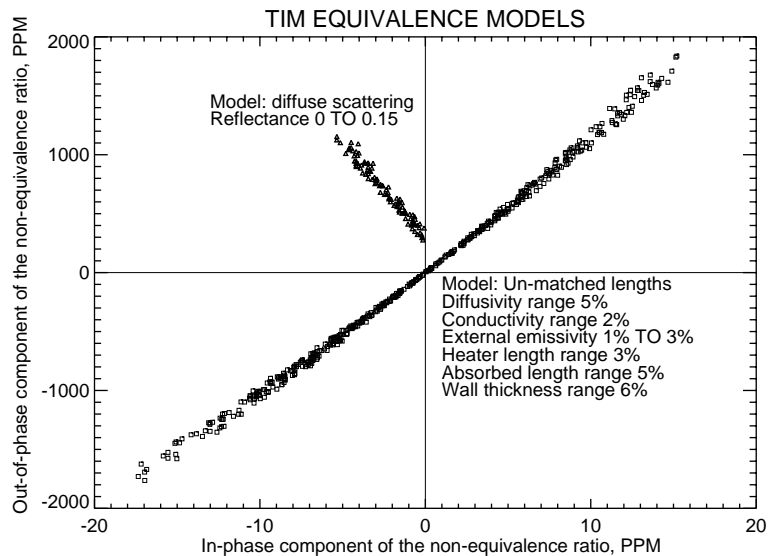
Figure 25: Typical Monte Carlo Study of the Equivalence Ratio

3.1.7.2   SIM Uncertainty Analysis

The accuracy for determining solar spectral irradiance with the SIM instrument follows from the uncertainty in the individual terms of equation 3.1.2.2.1.   The uncertainty equation can be written (assuming independence for the various terms):

$$\frac{\sigma^2_{E_\lambda}}{E^2_\lambda} = \sum_i \frac{\sigma^2_{u_i}}{u^2_i}$$

3.1.7.2.1

This equation follows the terminology of sections 3.1.2.1 and 3.1.2.2, the u_i are the 10 terms individually described in that section and the σ_u are the corresponding uncertainty estimates.   An estimate of the magnitude of the corrections and the measurement uncertainty budget are summarized in Table 15.   This table shows the correction, the subsection where it is described, the magnitude of the effect, and uncertainty that remains after the correction is made.   The uncertainty budget represents a plausible value that will be achieved during instrument calibration.

Table 15: SIM Uncertainty Budget for Absolute Accuracy				
Parameter	Subsection	Magnitude of effect(ppm)	Budget (ppm)	Method of Study
Joule heating factor	3.1.2.2.1			NIST traceable V and Ω
Standard Volt +DAC		2,000,000	10	
Standard Ohm, leads		1,000,000	10	
Solar distance correction	3.1.2.2.2	+33,116 to −33,764	5	JPL Ephemeris
Doppler correction	3.1.2.2.3	23	1	JPL Ephemeris
Shutter waveform	3.1.2.2.4	100	20	Prototype design
Prism transmission	3.1.2.2.5	22,000 to 150,000	150	Index of refraction, in-flight cal.
Entrance aperture	3.1.2.2.6			
Area		1,000,000	60	Metrology
Diffraction		22,000 to 3,000	100	Lawrence *et al*.
Spectral Bandwidth	3.1.2.2.6	1,000,000	150	Index of refraction, preflight cal, solar spectrum
Bolometer absorption	3.1.2.2.7	600 to 1,000	60	Preflight BRDF studies
Wavelength shift	3.1.2.2.8	150	150	In-flight cal, solar spectrum
Servo closed-loop gain	3.1.2.2.9	3,000	10	Design, in-flight calibration
Equivalence ratio	3.1.2.2.10	5,000	10	Theoretical studies
Total Uncertainty			**141**	

As an example of how to use this table, consider the entry for the entrance aperture.   The area term is determined in the laboratory at a fixed wavelength and is known to 60 ppm.   Its contribution to Equation 3.1.2.1.2 is of order 1 (a million parts per million).   This measured area must also be corrected for diffraction and contributes a value between 22000 and 3000 ppm; after correction the residual uncertainty is about 100 ppm.

3.1.7.3   SOLSTICE Uncertainty Analysis

The accuracy for determining solar irradiance with the SOLSTICE spectrometers follows from the uncertainty in the terms in Equations 3.1.2.3.1 and 3.1.2.3.2.   These equations are used to calculate both solar and stellar irradiance.   If the explicit dependence on wavelength is suppressed, these earlier equations can be rewritten in the form

$$E_{AU} = \frac{C}{R \cdot Tr_{Filter1} \cdot Tr_{Filter2} \cdot f_{Degradation} \cdot f_{AU} \cdot f_{Doppler}} \qquad \text{3.1.7.3.1}$$

$$C = \frac{S \cdot M - Dc - Sl'}{\Delta t} \qquad \text{3.1.7.3.2}$$

$$R = R_C \cdot f_{FOV}(\theta, \phi) \cdot A_{Entrance} \cdot \Delta\lambda$$

where $\quad M = N(\tau) \cdot G_{PMT}(V,T) + \int G_{Scat}(\lambda')d\lambda' \quad$ and $\quad Sl' = Stray + \int S(\lambda') \cdot (G_{Scat}(\lambda - \lambda') + B)d\lambda' \quad$ are the multiplicand of the observed signal S and light scattered *into* wavelength λ respectively, then the percentage uncertainty in the irradiance is given as

$$\sigma_E^2 = \sigma_C^2 + \sigma_R^2 + \sigma_{Tr_{Filter1}}^2 + \sigma_{Tr_{Filter2}}^2 + \sigma_{f_{Degradation}}^2 + \sigma_{f_{AU}}^2 + \sigma_{f_{Doppler}}^2 \qquad \text{3.1.7.3.3a}$$

$$\sigma_C^2 = \frac{S^2 M^2 \cdot (\sigma_S^2 + \sigma_M^2 + \sigma_\lambda^2) + Dc^2 \cdot \sigma_{Dc}^2 + Sl'^2 \cdot \sigma_{Sl'}^2}{(S \cdot M - Dc - Sl')^2} + \sigma_{\Delta t}^2 \qquad \text{3.1.7.3.3b}$$

$$\sigma_R^2 = \sigma_{R_C}^2 + \sigma_{f_{FOV}(\theta,\phi)}^2 + \sigma_{A_{Entrance}}^2 + \sigma_{\Delta\lambda}^2 . \qquad \text{3.1.7.3.3c}$$

Equation 3.1.2.3.9 is used to calculate the solar irradiance from irradiance standards. If it is rewritten in the form

$$E_{AU} = \frac{C_{Sun}}{R' \cdot Tr_{Filter1} \cdot Tr_{Filter2} \cdot f_{Degradation} \cdot f_{AU} \cdot f_{Doppler}} \qquad \text{3.1.7.3.4}$$

$$R' = \frac{C'_{Std}}{E_{Std}} \cdot \Gamma(\Omega) \qquad \text{3.1.7.3.5}$$

$$C_{Sun} = S_{Sun} \cdot M - Dc_{Sun} - Sl'_{Sun}$$

$$C'_{Std} = S_{Std} \cdot M - Dc_{Std} - Sl'_{Std}$$

then the percentage uncertainty in the irradiance is given as

$$\sigma_E^2 = \sigma_{C_{Sun}}^2 + \sigma_{R'}^2 + \sigma_{Tr_{Filter1}}^2 + \sigma_{Tr_{Filter2}}^2 + \sigma_{f_{Degradation}}^2 + \sigma_{f_{AU}}^2 + \sigma_{f_{Doppler}}^2 \qquad \text{3.1.7.3.6a}$$

$$\sigma_{C_{Sun}}^2 = \frac{S_{Sun}^2 M^2 \cdot (\sigma_{S_{Sun}}^2 + \sigma_M^2 + \sigma_\lambda^2) + Dc_{Sun}^2 \cdot \sigma_{D_{Sun}}^2 + Sl'_{Sun}^2 \cdot \sigma_{Sl'_{Sun}}^2}{(S_{Sun} \cdot M - Dc_{Sun} - Sl'_{Sun})^2} \qquad \text{3.1.7.3.6b}$$

$$\sigma_{R'}^2 = \frac{S_{Std}^2 M^2 \cdot (\sigma_{S_{Std}}^2 + \sigma_M^2 + \sigma_\lambda^2) + Dc_{Std}^2 \cdot \sigma_{D_{Std}}^2 + Sl'_{Std}^2 \cdot \sigma_{Sl'_{Std}}^2}{(S_{Std} \cdot M - Dc_{Std} - Sl'_{Std})^2} + \sigma_{E_{Std}}^2 + \sigma_{\Gamma(\Omega)}^2 . \qquad \text{3.1.7.3.6c}$$

Values for the estimated uncertainties in the parameters are derived from laboratory measurements of instrument components, results from calibrations performed at SURF and the UARS instrument in-flight performance, and from software simulations of expected in-flight radiometric performance. Detailed discussion of the basis for these estimates appears in Section 3.1.2.3.

There are three primary SOLSTICE measurements:

1. Measure the solar irradiance with 5% absolute accuracy at the on-orbit beginning of life
2. Compare the solar irradiance to stellar irradiance with a relative accuracy of 0.5%
3. Track changes in solar irradiance with a relative accuracy of 0.5% per year.

Each of these measurements has different dependence on the various parameters as described below.

3.1.7.3.1 Measure the Solar Irradiance with 5% Absolute Accuracy

Equation 3.1.2.3.9 provides the basis for calculating the absolute solar irradiance based on an instrument calibration performed at SURF III. The relevant uncertainty equation is 3.1.7.3.6. Values for the

54

contributions that uncertainty estimates make to the total uncertainty are summarized in Table 9. Contributions for uncertainty in scattered light and nonlinearity scale as $\sigma_D \cdot \dfrac{Dc^2}{(S \cdot M - Dc - Sl')^2}$ and $\sigma_{Sl'} \cdot \dfrac{Sl'^2}{(S \cdot M - Dc - Sl')^2}$. The other uncertainties scale nearly 1:1. Table 16 includes an entry for pointing error ($\sigma_{f(\theta,\phi)}$) that is not explicitly contained in Equation 3.1.7.3.3a. Uncertainty in the correction for diffraction (Section 3.1.2.3.5) is included in the estimate for the uncertainty in the geometric correction ($\sigma_{\Gamma(\Omega)}$).

Table 16: SOLSTICE Uncertainty Contributions to Solar Absolute Irradiance Measurements

Parameter	Symbol	FUV Estimated Average Value	MUV Estimated Average Value	FUV Required Average Value	MUV Required Average Value
Solar signal	σ_S	0.4	0.1	0.5	0.1
Multiplicand	σ_M	0.2	0.2	1.02	1.12
Wavelength Scale	σ_λ	0.2	0.2	0.5	0.5
Dark Count	σ_{Dc}	0.1	0.1	1.0	1.0
Scattered Light	$\sigma_{Sl'}$	0.2	0.1	1.0	1.0
Corrected Solar Signal	σ_C	**0.52**	**0.30**	**1.88**	**1.94**
SURF Signal	σ_{SStd}	0.2	0.4	0.5	0.5
Multiplicand	σ_{MStd}	0.1	0.1	1.0	1.0
Wavelength Scale	$\sigma_{\lambda Std}$	0.1	0.1	0.5	0.5
Dark Count	σ_{DcStd}	0.1	0.2	1.0	1.0
Scattered Light	$\sigma_{Sl'Std}$	0.1	0.1	1.0	1.0
Corrected SURF Signal	σ_{CStd}	0.35	0.49	1.87	1.87
SURF Irradiance	σ_{EStd}	1.0	1.0	2.0	2.0
Geometric Correction	$\sigma_{\Gamma(\Omega)}$	1.0	1.0	3.0	3.0
Pre-flight Response	σ_{Rc}	**1.46**	**1.50**	**4.06**	**4.06**
Corrected solar signal	σ_C	0.52	0.30	1.88	1.94
Pre-flight Response	σ_{Rc}	1.46	1.50	4.06	4.06
Filter Transmission	$\sigma_{T\,Filter}$	0.0	0.25	0.0	1.0
Correction to 1AU	$\sigma_{f\,1AU}$	0.01	0.01	0.01	0.01
Degradation	$\sigma_{f\,Degrade}$	0.0	0.0	0.0	0.0
Doppler Shift	$\sigma_{f\,Doppler}$	0.01	0.01	0.01	0.01
Pointing Error	$\sigma_{f(\theta,\phi)}$	**0.6**	**0.6**	**1.0**	**1.0**
Total Uncertainty		**1.66**	**1.68**	**4.59**	**4.82**

3.1.7.3.2   Compare the Solar Irradiance to Stellar Irradiance with 0.5% Relative Accuracy

Equations 3.1.2.3.1 and 3.1.2.3.2 provide the basis for comparing solar and stellar irradiance:

$$\frac{E_{AU}}{E_{Star}} = \frac{C_{Sun}}{C_{Star}} \cdot \frac{A_{Star} \cdot \Delta\lambda_{Star}}{A_{Sun} \cdot \Delta\lambda_{Sun} \cdot f_{AU} \cdot f_{Doppler}} \cdot \Gamma'(\Omega) \cdot \Gamma_{Degradation}(\Omega) \qquad 3.1.7.3.7$$

$$C_{Sun} = S_{Sun} \cdot M - Dc_{Sun} - Sl'_{Sun} \qquad 3.1.7.3.8$$

$$C_{Star} = S_{Star} \cdot M - Dc_{Star} - Sl'_{Star}$$

$$\Gamma'(\Omega) = \frac{\int_{\Omega Star} f(\theta,\phi) d\Omega}{\int_{\Omega Sun} f(\theta,\phi) d\Omega}$$

$$\Gamma_{Degradation}(\Omega) = \frac{\int_{\Omega Star} f_{Degradation}(\theta,\phi)d\Omega}{\int_{\Omega Sun} f_{Degradation}(\theta,\phi)d\Omega}$$

Γ'(Ω) and *Γ_{Degradation}(Ω)* are geometrical factors that account for differences in instrument response to sources of different angular size at launch and changes in that response during the mission. The percentage uncertainty in this ratio is given by:

$$\sigma_E^2 = \sigma_{Csun}^2 + \sigma_{Cstar}^2 + \sigma_{A_{Star}/A_{Sun}}^2 + \sigma_{\Delta\lambda_{Star}/\Delta\lambda_{Sun}}^2 + \sigma_{\Gamma'(\Omega)}^2 + \sigma_{\Gamma_{Degradation}(\Omega)}^2 + \sigma_{f_{AU}}^2 + \sigma_{f_{Doppler}}^2 \qquad 3.1.7.3.9a$$

$$\sigma_{C_{Sun}}^2 = \frac{S_{Sun}^2 M^2 \cdot (\sigma_{S_{Sun}}^2 + \sigma_M^2 + \sigma_\lambda^2) + Dc_{Sun}^2 \cdot \sigma_{D Sun}^2 + Sl'_{Sun}^2 \cdot \sigma_{Sl'_{Sun}}^2}{(S_{Sun} \cdot M - Dc_{Sun} - Sl'_{Sun})^2} \qquad 3.1.7.3.9b$$

$$\sigma_{C_{Star}}^2 = \frac{S_{Star}^2 M^2 \cdot (\sigma_{S_{Star}}^2 + \sigma_M^2 + \sigma_\lambda^2) + Dc_{Std}^2 \cdot \sigma_{D Std}^2 + Sl'_{Star}^2 \cdot \sigma_{Sl'_{Star}}^2}{(S_{Star} \cdot M - Dc_{Star} - Sl'_{Star})^2} . \qquad 3.1.7.3.9c$$

Values for the contributions that uncertainty estimates make to the total uncertainty are summarized in Table 17.

Parameter	Symbol	FUV Estimated Average Value	MUV Estimated Average Value	FUV Required Average Value	MUV Required Average Value
			Table 17: SOLSTICE Uncertainty Contributions to Solar Stellar Irradiance Comparison		
Solar signal	σ_S	0.1	0.05	0.1	0.1
Multiplicand	σ_M	0.2	0.2	0.2	0.2
Wavelength Scale	σ_λ	0.1	0.1	0.2	0.2
Dark Count	σ_{Dc}	0.1	0.1	1.0	1.0
Scattered Light'	$\sigma_{Sl'}$	0.2	0.1	1.0	1.0
Corrected Solar Signal	σ_{CSun}	**0.25**	**0.23**	**0.3**	**0.3**
Stellar Signal	σ_{SS}	0.1	0.2	0.1	0.1
Multiplicand	σ_{MS}	0.2	0.2	0.2	0.2
Wavelength Scale	$\sigma_{\lambda S}$	0.1	0.1	0.2	0.2
Dark Count	σ_{Dc}	0.1	0.2	1.0	1.0
Scattered Light	$\sigma_{Sl'}$	0.1	0.1	1.0	1.0
Corrected Stellar Signal	$\sigma_{C Star}$	**0.25**	**0.30**	**0.3**	**0.3**
Corrected Solar Signal	σ_C	0.25	0.23	0.3	0.3
Corrected Stellar Signal	σ_{Rc}	0.25	0.30	0.3	0.3
Entrance Area Ratios	$\sigma_{Astar/Asun}$	0.1	0.1	0.1	0.1
Wavelength Bandpass Ratios	$\sigma_{\Delta\lambda star/\Delta\lambda sun}$	0.1	0.1	0.1	0.1
Solar/Stellar Γ Factor	$\sigma_{\Gamma'(\Omega)}$	0.1	0.1	0.15	0.15
Degradation Γ Factor	$\sigma_{\Gamma Degra(\Omega)}$	0.1	0.1	0.15	0.15
Correction to 1AU	$\sigma_{f 1AU}$	0.01	0.01	0.01	0.01
Doppler Shift	$\sigma_{f Doppler}$	**0.01**	**0.01**	**0.01**	**0.01**
Total Uncertainty		**0.41**	**0.43**	**0.50**	**0.50**

Contributions for uncertainty in scattered light and nonlinearity scale as $\sigma_D \cdot \dfrac{Dc^2}{(S \cdot M - Dc - Sl')^2}$ and

$\sigma_{Sl'} \cdot \dfrac{Sl'^2}{(S \cdot M - Dc - Sl')^2}$. The other uncertainties scale nearly 1:1. Uncertainty in the correction for diffraction (Section 3.1.2.3.5) is included in the estimate for the uncertainty in the geometric correction ($\sigma_{\Gamma(\Omega)}$)

3.1.7.3.3 Track Changes in Solar Irradiance with 0.5% Per Year Relative Accuracy

Repeated solar/stellar comparisons track changes in solar irradiance. The relevant equation is 3.1.7.3.7 with the area and bandwidth terms removed.

$$\Delta \frac{E_{AU}}{E_{Star}} = \frac{C_{Sun}}{C_{Star} \cdot f_{AU} \cdot f_{Doppler}} \cdot \Gamma'(\Omega) \cdot \Gamma_{Degradation}(\Omega) \qquad 3.1.7.3.10$$

The remaining terms and uncertainty estimates are identical to those described by equations 3.1.7.3.7 to 3.1.7.3.9. Table 18 summarizes the uncertainties in the terms in Equation 3.1.7.3.10.

Table 18: SOLSTICE Uncertainty Contributions to Tracking Changes in Solar Irradiance

Parameter	Symbol	FUV Estimated Average Value	MUV Estimated Average Value	FUV Required Average Value	MUV Required Average Value
Corrected Solar Signal	σ_C	0.25	0.23	0.3	0.3
Corrected Stellar Signal	σ_{Rc}	0.25	0.30	0.3	0.3
Solar/Stellar G Factor	$\sigma_{\Gamma'(\Omega)}$	0.1	0.1	0.15	0.15
Degradation G Factor	$\sigma_{\Gamma Degra(\Omega)}$	0.1	0.1	0.15	0.15
Correction to 1AU	$\sigma_{f\,1AU}$	0.01	0.01	0.01	0.01
Doppler Shift	$\sigma_{f\,Doppler}$	0.01	0.01	0.01	0.01
Total Uncertainty		**0.38**	**0.40**	**0.48**	**0.48**

3.1.7.4 XPS Uncertainty Analysis

The uncertainty for the XPS irradiance, σ_E, is derived from the uncertainty analysis of equation 3.1.2.4.7 to be

$$\sigma_E = \sqrt{\sigma_{Cor}^2 + \sigma_R^2 + \sigma_A^2 + \sigma_{\Delta\lambda}^2 + \sigma_{AU}^2 + \sigma_{Deg}^2 + \sigma_{FOV}^2 + \sigma_{Doppler}^2} \qquad 3.1.7.3.1$$

where the uncertainties, σ, are in percentage, and the subscripts Cor, R, A, AU, Deg, FOV, Doppler, and $\Delta\lambda$ are for the I_{Cor}, R, A, f_{AU}, $f_{Degradation}$, f_{FOV}, $f_{Doppler}$, and wavelength uncertainties, respectively.

The σ_{Cor} includes the uncertainty of the measurement and the conversion to current for the I_{Cor} as follows.

$$\sigma_{Cor} = \frac{I'_{Total} \cdot \sigma_{I'_{Total}} + \frac{I'_{Window} B'_{Total}}{B'_{Window}} \cdot \sqrt{\sigma_{I'_{Window}}^2 + \sigma_{B'_{Window}}^2 + \sigma_{B'_{Total}}^2}}{I'_{Total} - \frac{I'_{Window} B'_{Total}}{B'_{Window}}} \qquad 3.1.7.3.2$$

The uncertainty propagation for each I' or B' parameter in equation 3.1.2.4.8 is given by:

$$\sigma_{I'} = \sqrt{\sigma_b^2 + \left(\frac{\sqrt{\frac{C}{\Delta t}} + \sqrt{\frac{C_{Dark}}{\Delta t}}}{C - C_{Dark}} \right)^2} \qquad 3.1.7.3.3$$

Because the count rate is 10^4 to 10^6 cps, dark count rate is about 100 cps, and the integration time, Δt, for XPS is 10 seconds, the uncertainty in the measurements in the second term will range from 0.3% to 0.03%. The ability to calibrate the conversion from counts to current has a 0.5% uncertainty. The worst case value for each $\sigma_{I'}$ is 0.5%. With this 0.5% for each $\sigma_{I'}$ and the typical ratio of the total signal to the visible current being 2, the typical σ_{cor} will be 1.5%.

The σ_R has two contributions, one being the uncertainty of the calibration done at NIST SURF and the other being the uncertainty in deriving the weighted average sensitivity ($\langle S \rangle$ in equation 3.1.2.4.6). The calibration uncertainty is typically 10% based on previous calibrations of photodiodes above 5 nm by Randy Canfield at NIST [Bailey, *et al.*, 1999]. Below 5 nm, a model of the photodiode sensitivity and transmission of the thin film filters is used that agrees with the NIST calibrations above 5 nm. This model has been validated with radioactive calibrations of the photodiodes at the shorter wavelengths below 1 nm, but to be conservative, the calibration uncertainty is estimated to be about 20% for below 5 nm. The uncertainty of the $\langle S \rangle$ determination is tracked separately as the change in wavelength distribution in the irradiance, and this uncertainty is called $\sigma_{\Delta\lambda}$. This variation of $\langle S \rangle$ over the solar cycle is typically 5% but can be as high as 10% for the shorter wavelength bandpass.

The σ_A is the uncertainty of the diode aperture area. The size of a diode aperture is typically a 0.2 inch circle, and is measured with a precision of 0.0005 inches. Therefore, the typical σ_A is 0.4%.

Combining all of these uncertainties as shown in Table 19, the absolute accuracy for the irradiance, σ_E, is estimated to be 12% above 5 nm and 21% below 5 nm. The majority of this uncertainty arises from the sensitivity. Therefore, improvement in the NIST calibrations of the photodiodes' sensitivity will make the largest improvement in the irradiance scaling factors for the XUV Photometers. Considering the significant improvements in the NIST SURF absolute uncertainties by more than a factor of 5 from their renovation to SURF-III, it seems realistic to reduce the uncertainty of the NIST calibrations by a factor of 2. If so, the uncertainty for the XPS irradiance would then range from 9% to 12%.

Table 19: XPS Absolute Accuracy		
Parameter	Required Value	Estimated Value
σ_b	1 %	0.5 %
Total / Dark Ratio	> 10	200
Total / Visible Ratio	> 1.3	2
Δt	> 1 sec	10 sec
σ_{cor}	10 %	1.5 %
σ_R	20 %	10 %
σ_{Deg}	15 %	3 %
σ_A	2 %	0.4 %
$\sigma_{\Delta\lambda}$	10 %	5 %
σ_{AU}	0.03 %	0.002 %
Total Uncertainty, σ_E	**30 %**	**12 %**

The relative accuracy, that is the accuracy for comparing irradiance on one day to another day, is a reduced from the absolute accuracy because only the measurement precision and degradation function are critical for the relative accuracy. Table 20 shows the combination of those two parameters for the relative accuracy. The derivation of the degradation function is the most important component of the relative accuracy.

Table 20: XPS Relative Accuracy		
Parameter	Required Value	Estimated Value
σ_{meas}	1 %	0.3 %
σ_{Deg}	15 %	3 %
Total Uncertainty $\sigma_{E\_relative}$	**15 %**	**3 %**

The measurement precision for XPS is primarily the counting uncertainty associated with the conversion of current to frequency by the XPS photodiode electronics. The XPS measurement precision is therefore calculated as one over the square root of the total counts measured during an integration period. There are three different components for each XUV photometer measurement: XUV, visible, and dark signals. The measurement precision of each is different because of the different signal levels, thus these three precisions are listed separately in Table 21. These measurement precisions are based on a single 10 second integration, so the daily measurement precision is significantly better by a factor of about 20.

Table 21: XPS Measurement Precision		
Parameter	Required Value	Estimated Value
XUV Signal	1 %	0.1 %
Visible Signal	1 %	0.2 %
Dark Signal	2 %	1 %

3.2   Practical Algorithm Considerations

3.2.1   Numerical Computation Considerations

The SORCE reduction algorithms are all mathematically simple and computationally straightforward. There are no difficult non-linear inversions (such as required, for example, to recover an atmospheric density profile of a chemical species from a limb radiance profile). The most computationally intensive activities include the frequent re-computation of a (linear) least-squares spline model of the current solar spectrum, and of (non-linear) least-squares Gaussian models of selected Solar UV emission lines. These are "forward" computations and, with careful coding and safeguards, are not problematic.

3.2.2   Programming / Procedural Considerations

The SORCE data processing system is designed around a central data store and an object-oriented system of data insertion and access services. The production of science products commences upon the receipt of science and engineering telemetry, orbital elements, and ephemeris for a given processing period (6-hourly or daily). The higher-level products do not depend on all lower-level or intermediate products, and these independent chains may be exploited by a multi-threaded processing design. SORCE will use a modern commercial relational database management system (RDBMS), and exploit the capabilities of such a system to automatically trigger events (such as science processing) based upon state criteria. The science processing system is described in more detail in Appendix C (Data Processing Plan)

3.2.3   Exception Handling

Production processing modules (programs) will be designed to handle every conceivable processing event, so that the likelihood of un-planned terminations is reduced to an absolute minimum. Moreover, many such

failures are locally restricted in time (e.g., a few missing data), and for daily or 6-hourly means, these missing data may be handled simply by omitting (skipping) the failing data.

In general, the *design-by-contract* principle will be strictly enforced in the design of module (object) interfaces. Historically, the failure to enforce this principle has been the major cause of unforeseen, un-handled processing errors.

4 Calibration, Validation, and Constraints

4.1 Calibration

4.1.1 Absolute (pre-flight) Calibration Plan

The SORCE pre-flight calibrations include unit level calibrations in the LASP/CU calibration laboratory and system level calibrations primarily at the NIST Synchrotron Ultraviolet Radiation Facility (SURF). Many of the calibration techniques for the SORCE are similar to those used for the UARS SOLSTICE calibration program [Woods *et al.*, 1993] and for LASP's TIMED and suborbital solar EUV irradiance program [Woods and Rottman, 1990].

4.1.1.1 Unit Level Calibrations

A number of critical unit level tests must be performed for the SIM and/or TIM sub-systems. 1) A telecentric metrological camera system is used to compare the entrance slit against a precision grid to obtain an effective slit area at several wavelengths. A theoretical analysis is then used to calculate the effective slit narrowing as a function of λ for SIM. 2) Broadband and laser BDRF (bidirectional reflectance function) studies determine the properties of the nickel phosphorous black. 3) The ESR detector sensitivity will be compared against a trap diode system that serves as a transfer standard to the NIST cryogenic radiometer. 4) The refractive index of the SIM prism material will be experimentally validated prior to launch using the method outlined in the paper of Tropf and Thomas [1998]. 5) Transmission tests will be performed at LASP. 6) Critical electronic components will be compared and tracked against NIST traceable standards, including standard voltage and resistance values. 7) Samples of all critical components will be kept as ground witnesses. As metrological equipment improves the measured standards can be re-evaluated. This is particularly true for the apertures and the components used to produce the standard watt. Protecting and preserving samples of the prism glass will be important to study long-term changes in the material.

For SOLSTICE unit level calibrations include measurements and characterization of individual optical and instrument elements, such as gratings, detectors, and apertures. The LASP/CU Calibration and Test Equipment 2 (CTE-2) is primarily used for the characterization of mirrors, gratings, and detectors in order to select the best element. The radiometric calibration for the CTE-2 uses photodiodes that are calibrated at NIST. Many of the CTE-2 characterization tests, including the reflection and grating efficiency measurements, only require relative calibrations using two detectors, usually photon-counting photomultiplier tubes (PMTs). The calibration uncertainties for the CTE-2 measurements typically range from 10-20%. The scattered light properties of the diffraction gratings will also be analyzed using the equipment and procedures described by Woods *et al.* [1994].

The photodiodes in the XPS are first calibrated at NIST by collaborators Randall Canfield and Rob Vest. These calibrations are a standard NIST service using the NIST SURF and yield a detector responsivity calibration with a typical uncertainty of about 10%. These SURF calibrations are extended down to 0.1 nm using a calibrated radioactive source (Fe-55 at 0.21 nm) and a model that matches the SURF calibrations using the most recent transmission coefficients for the thin film materials, including oxide layers, and the response of the silicon photodiode [Bailey *et al*., 1999].

The calibrations of the sun sensor and analog monitors are also considered part of the unit level calibrations. The sun sensor will be calibrated by the manufacturer with a precision of 10 arc-seconds and will be verified again during the SORCE instrument-level calibrations. The analog temperature and voltage monitors will be calibrated with a precision better than 0.1 °C and 20 millivolts.

4.1.1.2   System Level Calibrations

The system level calibrations for SOLSTICE and SIM include detailed wavelength and photometric calibrations of the fully assembled instruments. For the SIM instrument, critical information found in the unit level tests will be combined with the ray trace analysis to define a theoretical response function for the instrument and tested against measurements with amplitude stabilized lasers. Additional broadband data will be acquired by comparison against FEL lamps. Deviations from ideal behavior will be studied to determine the cause of the discrepancy and corrective action, or additional second order corrections will be applied to the radiometric measurement equation. The wavelength scale of the instrument will be established by calibration with selected atomic emission line spectra as produced from hollow cathode lamps. Additional tests with structured, broadband molecular absorbers such as SO_2 and NO_2 will also be performed. Critical wavelength tests will be performed in vacuum, but routine tests conducted in air will be corrected by application of Edlen's formula [Edlen 1953]. The Kitt Peak atlas [Kurucz, *et al*. 1984] of the Sun will be convolved with the SIM instrument function and used as a wavelength diagnostic during the course of the mission.

For SOLSTICE the wavelength calibration involves the use of platinum and mercury lamps that provides many lines above 115 nm. The primary photometric calibration for the UV instruments occur at the NIST SURF. The SURF BL-2 is dedicated for NASA instrumentation and provides a large vacuum tank and gimbal system that can easily accommodate the SORCE SOLSTICE instruments. The photometric calibrations at SURF include mapping each instrument responsivity over its field of view (a 7 x 7 gridded map over its 1.5° x 1.5° FOV along with a more detailed cruciform along two measurement strips through the center for the FOV with 0.1° resolution). Both the SOLSTICE instruments and calibration equipment at SURF are controlled by computers; therefore, the calibration tasks and analysis are largely automated, and all calibration data are archived.

4.1.2   Relative (In-flight) Calibrations

The in-flight calibration plan for the SORCE includes 1) on-board reference detectors for all four instruments, 2) bright, blue stars for SOLSTICE, 3) redundant channel capability for all instruments, and 4) underflight calibrations by almost identical instruments on sounding rockets, or the Space Shuttle, most importantly for the XPS. The wavelength calibration for the in-flight data uses the many well-known solar emission features to determine the wavelength scale.

4.1.2.1   TIM

TIM is a primary solar radiometer of higher accuracy than any known irradiance source or transfer radiometer. As a primary radiometer, its accuracy depends on accurate characterization before and during flight, rather than on an instrument calibration. In addition, under-flights with a nominally identical instrument on the Shuttle Hitchhiker will further validate the measurements.

The characterization of TIM includes the calibration of the terms and factors of the TIM measurement equation 3.1.2.1.2. Table 22 summarizes the methods and traceability of the pre-flight calibrations. Table 23 summarizes the on-orbit re-calibration methods.

4.1.2.1.1   TIM Pre-Flight Component Calibrations

Each factor of the measurement equation requires attention. In addition, parasitic effects not in the measurement equation require characterization.

4.1.2.1.1.1   Shutter Waveform Factor Ψ

The shutter is operated from the crystal-controlled clock in the DSP. The mechanical delay on opening is 20-25 msec, and the rise time is 6-9 msec. These departures are so short compared to the 100 sec period that measurements of the transmitted light with a digital oscilloscope suffice to determine Ψ.

4.1.2.1.1.2   Aperture A_p

We measure each aperture ourselves, and also compare against two NIST-calibrated apertures of nearly the same size. Our technique measures the effective aperture in the context of the actual baffles in TIM, while the NIST apertures (Joel Fowler) are calibrated as an actual geometrical area. The comparison, then, will have transfer uncertainty on the order of 40 ppm in addition to the 60 ppm uncertainty in the NIST calibration.

Our in-house calibration images the apertures with a simulated solar beam, through the same baffle restrictions as TIM, onto a 16-bit CCD. The lens system has very low scatter and distortion; and is telecentric. The "standard square meter" is laser-intereferometrically produced Ronchi ruling which is imaged horizontally and vertically to calibrate the CCD pixel scale. The basic algorithm normalizes the center of the aperture image to one, and integrates over the pixel area to give the transmission-area product. Parasitic effects that must be corrected include CCD non-linearity, stray light, point-spread function, temperature changes, ghost images, pixel and lamp variations, dark field, and bad-pixel rejection. This aperture characterization (calibration) will be published.

4.1.2.1.1.3   Cavity Absorption α

Each cavity (cone) is laser scanned on a ½ mm grid about its axis. The reflected light is measured with a large detector covering the mouth of the cone. To calibrate the laser intensity and the detector sensitivity, a diffuse scatterer is mapped in the same run to provide the absolute normalization of the scattering efficiency. Analysis of the experiment includes scattered light, stray signals, detector linearity, and the geometrical distributions and view factors. Several laser wavelengths are required so that the reflectivity can be averaged over the solar spectrum. The laser wavelengths available are 355, 457, 532, 623.8, 1523, 1570, 1064, 3392, and 10600 nm.

4.1.2.1.1.4   Loop Gain

The servo loop gain is best calibrated in flight and on the ground with a special program of the DSP that injects a test square wave into the closed loop; and observes the response. The result is the ratio of two complex digital numbers. This test signal is the programmable "Feed Forward" signal, also used to anticipate the change in solar radiation as the shutter is activated. If the feed forward signal is matched to the radiation signal within say, 1%, then the stability of TIM's gain is improved yet another factor of 100.

4.1.2.1.1.5   Equivalence Ratio

The equivalence ratio is calculated from experimentally determined parameters. The dominant task is to measure the distribution of absorbed radiation. This is done by measuring the temperature jump at absorption of a pulsed laser beam. The temperature measurements are made with a row of micro-thermistors, clamped to the exterior of a test cone. The moments of these measured distributions must be accurate to about 10%. See the uncertainty analysis for TIM, Section 3.1.7.1 for a summary of the required accuracy.

4.1.2.1.1.6   Standard Volt

The standard voltage is measured at various times during test and qualification of TIM through a test connector. It is assumed that the two flight standard voltages will track the ground witnesses (at least six), although we expect a 1-2 ppm change per year in the flight voltages. We calibrate the absolute value of the voltage with an HP3458A DVM, which is calibrated at Hewlett Packard and against our in-house Fluke 723B.

4.1.2.1.1.7 Standard Resistance

The standard resistance (standard ohm) on TIM is the replacement heater on the back of the cones. It is wound under controlled tension with "Evanohm" wire. The definitive measurements are made with the HP3458A DVM through a four-wire test connector. The HP3458A is periodically re-calibrated by Hewlett Packard and in house against a TEGAM SR104 standard resistor. It is assumed that changes in the cone resistor track changes in the ground witness resistors.

4.1.2.1.1.8 Dark Signal

The dark offset signal due to IR radiation within TIM will be calibrated on the ground with a vacuum LN2-cooled black cavity. This provides the offset dependence on the temperatures of the heat sink, cavity, and shutters. The definitive measurements are made in flight.

4.1.2.1.1.9 Miscellaneous Effects

TIM has a basic noise level of <1 ppm. Hence we will be able to see miscellaneous effects due to scattered light, shutter leakage, channel cross talk, thermal gradients, etc. Table 22 lists some of these measurements. Others will be made as the effects are discovered.

Table 22: TIM Pre-flight Component Calibrations

Quantity	Methods	Standard	Check Method
Shutter waveform Ψ	Transmission(time)	Digital scope	Mechanical model
Aperture A_p	CCD camera vs. Ronchi ruling	Laser Interferometer / Ronchi ruling	NIST Aperture, diffraction calc
Cavity Absorption α	Laser scans, reflection ratio at several wavelengths	Spectralon, diode linearity	Scatter theory, NIST check on one cone.
Loop Gain G	Feed forward Calibration	Ratio measurement	Calc. from model
Equivalence ratio: distributions	Measure distributions with pulsed laser excitation	Ratio measurement	Calc. from model and reflectance meas.
Equivalence ratio, Green function	Calculate from first principles. Parameters from tables	Timing measurements,	Frequency variation. Pointing variation
Standard Volt V	Measure at test connector, keep ground witnesses.	HP3458A, Josephson Junction	Fluke 723B, carry to NIST
Standard R, R	Measure 4-wire at test connector, keep ground witnesses.	HP3458A, Quantum Hall	Tegam SR104
Full Scale count	Electronic counter		Ab initio design check
DAC Linearity	Sample hold, HP3458A	Ratio measurement	
Off axis rejection	Solar simulator + goniometer	Ratio measurement	
Shutter leakage	Solar simulator + silicon diode	Ratio measurement	
Dark signal D_K	LN2 cryo-target	TIM, ratio	Model & theory

Cavity monitor diodes	Solar simulator, collimated	Lab radiometer	
Electrical cross talk	Analyze bridge signals	Volt/ratio measure	
Thermal cross talk	Solar Simulator, un-used pair	Ratio measure	Thermistor gradients
Temperature differences	Housekeeping thermistors	Hart 1521/5611T	NIST trace
Resistor TCRs	HP3458A, table values		

Table 23: TIM In-flight Re-Calibrations

Quantity	Methods
Shutter waveform Ψ	High speed DN time series. Look for timing changes.
Aperture A_p	Correct for housekeeping temperature. Ground witnesses.
Cavity Absorption α	Watch changes in cavity diode monitors.
Equivalence ratio	Second guess ground witness.
Equivalence ratio * Cavity Absorption α	Pointing variation from cruciform scans. Degradation from duty cycle of cavities.
Loop Gain G	Use Feed Forward. Calibration with feedforward
Standard Volt V	Ground witnesses.
Standard R, R	Assumed constant. Temperature correct. Ground witnesses.
Off axis rejection	Sunrise, sunset excess irradiance.
Dark signal D_K	Dark space observations. Correct for temperature
Cavity monitor diodes	Get initial signals, watch for changes.
Thermal cross talk	Watch thermistors at fundamental. Watch closed-shutter pair.

4.1.2.2   SIM

Two in-flight calibration operation modes track long-term degradation of the instrument. The first is a direct prism transmission calibration and the second is a two-spectrometer comparison.

The long-term effects of ionizing radiation (hv > 3eV) on the prism glass itself and the thin film ($<5\times10^{-10}$ m) of organic material that likely contaminates the surface will induce transmission changes of <0.5% over the course of the mission. This degradation mechanism is expected to directly effect the first-order prism transmission term $Tr(\lambda, f_{Degradation})$ (see section 3.1.2.2.2), and must be tracked over the course of the mission.

Prism transmission is defined as the ratio of the intensity of radiation after passage through an optical medium (I) to the intensity of the incident light beam (I_o). In the case of the Fèry prisms used in this

experiment, transmission losses include the Fresnel losses at the air-glass and glass-air interface, bulk loss in the fused silica, absorption in the aluminum coating, and scattering on both the front and rear surfaces. To obtain a true transmission measurement, it is necessary to account for effects related to the uniformity of prism material, non-symmetric light losses in the I and I_o measurement paths, and the spatial radiant sensitivity of the detector. These factors will be determined in the preflight characterization process.

The following instrument sequence will be executed initially on a 1% duty cycle basis to measure the transmission changes as a function of wavelength and time, $f_{Degradation}$. Assume that the transmission of prism A is to be measured and this is shown in Figure 26. Because channels A and B are identical, the prism B transmission can be calibrated by an analogous procedure. 1) The entrance shutter to spectrometer A is closed and the shutter to spectrometer B is opened. In the prism transmission calibration mode the hard radiation trap is located in the optical train to minimize exposure during this step. Sun light through entrance slit B is dispersed by prism B and a selected wavelength λ_{cal} illuminates the periscope (to be described below). 2) After monochromatic light passes through the periscope it is directed by a flat mirror on a bi-stable turntable mechanism to a focusing beam splitter that feeds two detectors for the UV/Visible and IR wavelength bands; this term gives I_o. 3) The turntable mechanism is rotated by 88.4° and is now out of the beam but still aligned with the optical axis of the detectors; the monochromatic light of wavelength λ_{cal} passes through prism A and travels back to the flat mirror where it directs light to the detector a second time to give the term I. Ratio of I to I_o gives the prism transmission factor at λ_{cal}. This procedure is repeated at 32 different wavelengths in the 300 to 1700 nm wavelength-region and a spline fit to the data is generated. The time-dependent prism transmission function is written:

$$Tr(\lambda, f_{Degradation}) = Tr_o(\lambda) \frac{\dfrac{I(\lambda)}{I_o(\lambda)}(t = t_{cal})}{\dfrac{I(\lambda)}{I_o(\lambda)}(t = t_o)}$$

In this equation, $Tr_o(\lambda)$ is the preflight prism transmission, and the I/I_o terms are the in-flight and preflight transmission ratios.

The periscope system that couples the two instruments consist of two 45° spherical mirrors (1038 mm focal length) separated by an intermediate slit that matches the spectrometer's entrance and exit slits (0.3×7 mm); the spherical mirrors are on-center and convex toward the prisms. There are two requirements on this periscope system: 1) the periscope focuses prism A onto prism B (and visa-versa), 2) the periscope images the entrance slit onto the intermediate slit.

The second in-flight calibration operation mode is a comparison of spectrometers A and B. Spectrometer B is exposed to ionizing radiation on a much lower duty cycle. The two spectrometers are operated simultaneously in the absolute irradiance mode so the instrument comparison excludes possible spacecraft pointing and thermal differences that would affect the comparison if the measurements were conducted in a serial format. The spectral irradiance for the A and B channels are calculated independently using the prism transmission function for each instrument $Tr_{AorB}(\lambda, f_{Degradation})$. The resultant irradiance measurements from spectrometers A and B can now be used as input for the long-term degradation models for the SIM instrument.
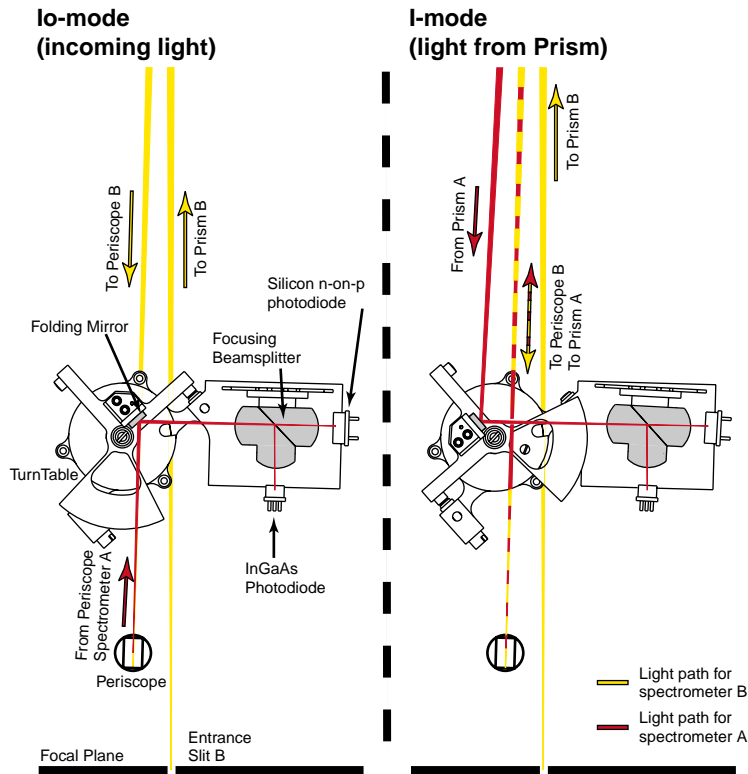
Figure 26: SIM Prism Calibration Mode

4.1.2.3   SOLSTICE

Retrieval of solar irradiance requires detailed knowledge of long term sensitivity changes in the SOLSTICE instruments. These changes, which result primarily from exposure to solar radiation, are measured by observing an ensemble of bright O-B stars. Table 6 lists the stars used to track changes in the in the UARS SOLSTICE instrument. See Section 2.3.3 for more discussion.

In Equation 3.1.7.3.1, $R_C(\lambda)$ is the preflight instrument response and $R_C(\lambda)/f_{Degradation}$ is the exposure dependent instrument response. $f_{Degradation}$ is determined by fitting time-dependent exponential functions to the instrument response measured at 36 discrete wavelengths. These results are interpolated in wavelength to produce the values of $f_{Degradation}$ required for Equation 3.1.7.3.1.

4.1.2.4   XPS

The XUV Photometers (XPs) are silicon XUV photodiodes with thin film filters to measure the integrated solar UV irradiance from 0.1 to 35 nm with a typical bandpass of 5 nm. These silicon XUV photodiodes are reference detectors for NIST in the XUV spectral region because they are extremely stable. The XPs are not expected to degrade by more than a couple of percent over the SORCE mission based on the stability tests that NIST and others have performed on these photodiodes as a function of exposure level to photons and high energy particles. Because the solar variability below 35 nm is expected to be a factor of 2 to 1000 (wavelength-dependent), the XPs can serve as an on-board reference detector. The estimated uncertainty for this assumption of detector stability is about 2%, as proven for the SNOE XPs.

The XPS has redundant XPs in order to have a working photometer for daily measurements and a lower duty cycle (reference) photometer for degradation analysis of the working photometer. The reference photometer will be used for a solar measurement every week; therefore, the cadence of the reference photometer is once per 105 measurements by the daily channel assuming 15 orbits per day.

The degradation between these reference photometer measurements will be derived using a model of degradation (exponential functions) as done by UARS SOLSTICE [Rottman and Woods, 1995]. The estimated uncertainty for this transfer of calibration is 5%. The XPS, being inherently stable, is expected to have a low degradation rate of a couple of percent per year.

As a validation of the reference XPS photometers, an underflight calibration experiment will be flown about once a year. The cadence of the underflight experiment is once per 52 measurements by the reference photometers, which is similar to the cadence of the reference photometers relative to the daily photometers. The underflight calibration experiment could be the prototype TIMED SEE instruments that were built in 1997-1998. This transfer of calibration includes both the relative change uncertainty (about 5%) plus the absolute irradiance uncertainty (10%); consequently, its uncertainty is larger at about 11%. Additional support for these SORCE underflight calibration experiments is assumed from the NASA suborbital program if the EOS SORCE program does not overlap with the TIMED SEE program.

Any other solar XUV irradiance measurements, such as from SNOE and TIMED SEE, will also be included in the XPS validation program.

There are no in-flight wavelength scale calibrations for the XPS because they are simply photometers. Therefore, the pre-flight wavelength calibrations are applied for the flight XPS data.

4.2   Validation

4.2.1   General Discussion

The validation process is a subset of the both the science analysis and the data quality assurance. The SORCE Science Team oversees this process which involves a careful examination of all solar data and judges the reasonableness and quality of the data to be released. The validation takes several different forms: 1) based on the confidence in the calibration and performance of the instruments, 2) based on comparison with previous and simultaneous measurements from other instruments, 3) based on our understanding of the Sun and its variability — an understanding based on solar models and on solar observations at other wavelengths.

4.2.2   Confidence in Measurements

Through the SORCE pre-flight calibrations and characterization, coupled with in-flight characterizations and verification, the instrument scientists will establish a precision and uncertainty to be ascribed to each observation. This evaluation differs with each instrument and may be a function of wavelength as well. Solar measurements should vary in a consistent manner from day to day, and from wavelength to wavelength. If an anomalous observation is detected, it will be evaluated against other observations. For example: does an overlapping channel observe the same anomaly? Does another instrument — looking at either the same or at a different wavelength — see a similar behavior? In the case of the SOLSTICE instruments is there normal variation in the stellar observations?

4.2.3   Comparison With Other Solar Measurements

When two (or more) independent measurements of the same source are compared they may agree or disagree. The agreement provides a strong confirmation that both measuring devices are probably operating within their stated uncertainties. If they disagree, it should be concluded that either one or both are incorrect. Nevertheless, the magnitude and sign (and for the spectral measurements — the wavelength dependence) of the disagreement provides some guidance as to possible sources of uncertainty. For example, for TSI the instrument delivering lower values might examine the aperture characterization paying special attention to possible sources of error that would lead to a smaller aperture than previously assumed.

There is no easy corrective action that should be taken, and it will require a close working relationship between the two instrument teams to reconcile the results and to find the solution. Whatever the outcome, a closer examination of the SORCE uncertainty budget and possible sources of uncertainties is warranted.

For SOLSTICE a major validation will compare the brightness of stars seen with the SORCE instrument to those seen by the UARS SOLSTICE. Whether or not the two missions overlap, the basic assumption is that the stars do not vary and therefore the two measurement programs should agree. Differences must be reconciled within the uncertainty budgets of the two respective programs, and agreement of the two sets of stellar observations provides great confidence that the calibrations of the two instruments are accurate. Differences within the uncertainty budgets of the two programs, on the order of ± 5%, will be deemed acceptable.

The SORCE data will be compared to other solar measurements. The UARS program may still be returning solar data, and the SORCE SOLSTICE data would then be compared to both SUSIM and UARS SOLSTICE. The GOME instrument on ERS-II may still be operating and those data would be compared to the SOLSTICE long-wavelength and SIM data as well. The TIMED SEE should still be operational and results would be compared to the SORCE XPS and SOLSTICE short-wavelength data. The SORCE SIM data will be related to measurements of total solar irradiance (TSI) as provided by UARS ACRIM and ACRIM-II on ACRIMSAT. The full integral of the SIM data over all wavelengths ($300 < \lambda < 2000$ nm) should correspond to 94% of TSI. Details of these types of validation and intercomparison program are provided in Woods *et al*. [1996]

4.2.4   Validation of SORCE Data Against Models of Solar Irradiance

Considerable effort is devoted to modeling solar variability through both "first-principal" physical models and through "semi-empirical" models. The semi-empirical models are based on a limited understanding of the physics of the solar emission coupled with another observation; for example, irradiance measurements taken at another wavelength — perhaps one easily seen from the ground — or from imaging data to synthesize contributions from contrasting regions on the solar disk.

SORCE data will be compared with all reasonable model calculations and results. The question arises as to how discrepancies will be handled, and once again, any deviations and differences would call for a close examination of the SORCE data and/or characterizations. Once again, the residual between the SORCE observation and the model calculation may provide insight to help identify a deficiency in the SORCE data. If the residual is found to correspond to a spacecraft or instrument function (e.g., a voltage, pointing offset, temperature or event), a causal relationship may be deduced, and thereby an additional or improved correction to the SORCE data may be called for. Because the models are based on many variables and assumptions, their reliability relative to the observations will be judged to be low, and they will not, of and by themselves, alter or influence the SORCE data. The SORCE observations together with their combined standard uncertainty will serve as constraints on present day models.

4.2.5   Quality Control and Diagnostics

The science production system supports both automatic and manual diagnostic statistical analyses of all science products. Deviations from expected or predicted values, flagging of anomalous values, and trends of many parameters and intermediate values, as well as final science values, are all incorporated into final or ancillary science data products. Quality flags in the final science products will be set both automatically and manually, via browse and other visualization tools. The highest quality level, indicating validated, definitive scientific results, must be set manually.

4.3   Constraints, Limitations, Assumptions

4.3.1   South Atlantic Anomaly

The SORCE SOLSTICE photomultiplier detectors are sensitive to energetic electrons in the lower layer of the Van Allen radiation belts, which reach down to the height of low-earth orbits in a few fairly well defined geographic regions (the largest is over the South Atlantic Ocean off the coast of Brazil). Measurements taken in these regions are excluded from our science products. This is accomplished by defining two-dimensional closed polygons in geographic coordinates, and using efficient computational geometry algorithms to test whether the spacecraft position (latitude, longitude) is in any of these regions.

The sizes and shapes of these regions depend on the height above the earth, and also upon instrument sensitivity and the geometry of the spacecraft and shielding. For a circular orbit each region is simply the intersection of the sphere in which the orbit lies with the 3-dimensional radiation belt. For a highly elliptical orbit a 3-dimensional region would need to be defined and tested for each such intersection. The SORCE orbit is presumed to be nearly circular, so that the method of two-dimensional polygons is sufficient.

Each interfering energetic electron region is defined as a list of polygon vertices (latitude, longitude) as "calibration data" which is used by the processing software. That is, the regions are not hard-coded in the software and may be readily changed. Indeed, it is expected that the pre-launch definitions will need to be modified, based on regular, in-flight dark current measurements (shutter closed), which serve to map the SAA regions.

4.3.2   Atmospheric Contributions

4.3.2.1   Atmospheric Absorption

The solar radiation and especially the solar ultraviolet component is absorbed by the Earth's atmosphere. Therefore if the line-of-sight from the SORCE to the Sun passes through the atmosphere, some radiation will be lost.

The *solar zenith angle* (SZA) is the angle from the spacecraft zenith to the sun line. The concept of the *tangent ray height*, TRH, which is the shortest distance from the surface of the Earth to the ray from the spacecraft to the Sun, is used. For an orbit altitude of 600 km, a TRH of zero km corresponds to a SZA of about 115°. This is a sunrise/sunset condition at the spacecraft and significant absorption (and refraction) would affect the data. A 90° solar zenith angle would correspond to a TRH equal to the spacecraft altitude, and likewise any SZA less than 90° corresponds to a TRH equal to the spacecraft altitude.

The atmospheric absorption is a strong function of wavelength and for the spectral measurements of SORCE — SOLSTICE and SIM — the maximum absorption occurs near 140 nm. Significant absorption of the solar irradiance at 140 nm would result if the TRH dipped below about 250 km, that is, if the SZA exceeded 109°. However, even at this SZA but at another wavelength, say 280 nm, the absorption would be negligible.

Although the amount of absorption could be calculated knowing the path of the radiation together with a model atmosphere, uncertainties in the calculation would result. For SORCE there is always ample solar observing time, and data that may be degraded by atmospheric absorption are excluded. The solar zenith angle is calculated for each measurement, and if for that wavelength the SZA exceeds the mask value, the observation is simply not included in the average for that six-hour period.

The XPS data are even more actively absorbed by upper atmosphere atoms and molecules, so the SZA mask is even tighter for these wavelengths. However, these data are also oversampled so it is easy to exclude affected observations from the average data sets. Two atmospheric species are present up to and above the

altitude of the SORCE spacecraft, atomic hydrogen and helium (to a much lesser extent). There is always atomic hydrogen between the spacecraft and the Sun, but for the wavelengths observed by SORCE SOLSTICE it only influences the Lyman-α line at 121.67 nm. The Sun emits a strong emission line at Lyman-α, and it has a half-width of about 0.1 nm. The geocoronal hydrogen is quite cool and has a very narrow absorption feature right in the center of the solar line. The processing algorithms correct for this absorption, but for SZA's less than 90°, the correction is less than 1%.

4.3.2.2   Atmospheric Emission

Corrections should also be made for radiation emitted by the atmosphere. If the instrument field of view intercepts a portion of the atmosphere that emits radiation (airglow or scattering) at the wavelength being recorded, it will contribute an unwanted signal. In general, the solar radiation is so intense that the atmospheric contribution is negligible even when the solar zenith angle of the observation exceeds 110°. This is not the case for the stellar observations of the SOLSTICE spectrometers. Similar to the above considerations of atmospheric absorption, stellar observations are excluded if the SZA exceeds 100°. This eliminates airglow at SOLSTICE short wavelengths, primarily from N_2 and O_2, emitted from the atmosphere below 300 km, and is a very conservative limit for excluding Rayleigh scattering in the atmosphere for the longer SOLSTICE wavelengths.

For Lyman−α the problem of atmospheric emission is much more severe. Because atomic hydrogen surrounds the spacecraft and extends into space in all directions, there is an unavoidable Lyman-α emission no matter the observation direction. Once again this contaminant signal is negligible (one part in 10^5) for observations of solar Lyman-α, but it is a major obstacle to observing the stars. In order to make stellar observations at the very short SOLSTICE wavelengths (between 115 and 130 nm) a special observation plan is conducted. This special stellar observation is referred to as a "companion experiment" and, in addition to observing the selected star, two additional observations are made of the dark sky in close proximity to the target star. The "airglow" Lyman-α is present in all three observations and the two adjacent "dark" observations are used to subtract the Lyman-α from the target star observation. Figure 27 provides an example of this type of observation and illustrates the background removal.
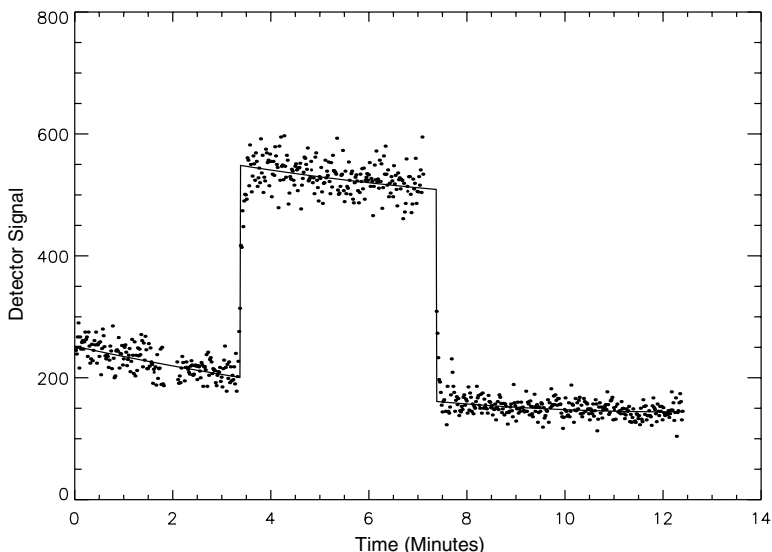
Figure 27: Stellar Companion Experiment observing η Ursa Majoris at 125 nm.

Appendix A   Scientific Overview and Background

A.1 Solar Variability

A.1.1   Recent Observations

Solar cycle 22 extends from a minimum solar activity period occurring roughly in 1986, through solar maximum spanning the period 1990 to early 1992, and descending to solar minimum that likely occurred in mid-1996. There have been a number of solar observations during this period of time, both brief Shuttle missions and long-duration satellite missions. Nevertheless, no single experiment covered the entire time interval nor the complete ultraviolet spectral range. Clearly the most valuable observation would have been provided by such a single instrument. Since this was not available, the second most valuable observation could have been provided by multiple instruments covering the same spectral range, and with their observations overlapping in time. This criterion of complete spectral coverage and overlap was in fact realized throughout most of solar cycle 22 for the spectral region 200 to 300 nm by a combination of Solar Backscatter Ultraviolet (SBUV) instruments. The shorter wavelength range (100 to 200 nm) was observed by a single instrument, the Solar Mesosphere Explorer (SME) from 1981 until April 1989, followed by a period of no observations until the launch of the Upper Atmosphere Research Satellite (UARS) in September 1991. Unfortunately this left a 28-month gap in this important spectral region spanning the very peak of solar cycle 22.

There have been four ultraviolet instruments that operated for extended periods during solar cycle 22. These four instruments are the Ultraviolet Spectrometer on SME [Rottman *et al*., 1982], the Solar Backscatter Ultraviolet (SBUV) on Nimbus-7 and also on the NOAA-9, -11, and -14 satellites [Cebula *et al*., 1994], the Solar Stellar Irradiance Comparison Experiment (SOLSTICE) [Rottman *et al*., 1993; Woods *et al*., 1993] and the Solar Ultraviolet Spectral Irradiance Monitor (SUSIM) [Brueckner *et al*., 1993] on the UARS. In addition, a Shuttle version of the SBUV (S-SBUV) [Cebula and Hilsenrath, 1996], a Shuttle version of the SUSIM [VanHoosier *et al*., 1988], and the Solar Spectrum Instrument (SOLSPEC) [Thuillier *et al*., 1997] have all flown on a number of Shuttle missions each lasting a few days. The time range and spectral coverage of these instruments are listed in Table 24.

Table 24: Recent Solar Measurements		
Instrument	**Wavelength Range**	**Time Interval**
SME	115 to 300 nm	Oct. 1981 to April 1989
SBUV:		
Nimbus-7	160 to 400 nm	Nov. 1978 to Feb. 1987
NOAA-9	160 to 405 nm	March 1985 to present
NOAA-11	160 to 405 nm	Feb. 1989 to Oct. 1994
NOAA-14	160 to 405 nm	Feb. 1995 to Oct. 1995
UARS SOLSTICE	119 to 420 nm	Oct. 1991 to present
UARS SUSIM	115 to 410 nm	Oct. 1991 to present
ATLAS:		Mar. 1992, April 1993,
S-SBUV	160 to 405 nm	and Nov. 1994
SUSIM	115 to 410 nm	
SOLSPEC	200 to 3200 nm	
Other Shuttle:		five calibration flights
S-SBUV	160 to 405 nm	Oct. 1989 - Jan 1996

The satellite observations of solar irradiance, some lasting only a few years and some much longer, provide time series of solar variability. Figure 28 provides an example of irradiance changes observed by the UARS SOLSTICE at Lyman-α (121.6 nm) between 1992 and 1998. Two dominant types of variation are evident, one is relatively rapid with a period of a few weeks, and the other is a long and gradual change with a period of several years. The changes in the instrument response are convolved in this time series and in similar time series at other ultraviolet wavelengths and from other instruments. In order to unambiguously extract the true solar variations the instrumental effects must first be evaluated and removed. All of the satellite instruments considered here, SME, the SBUV's and the UARS SOLSTICE and SUSIM, have experienced some degradation, typically small over short time periods but significant over periods of several years. With the exception of certain isolated and well-defined episodes when dramatic change in an instrument's response may occur (perhaps due to an instrument or spacecraft anomaly), the general norm is that instrument degradation is relatively slow and monotonic.
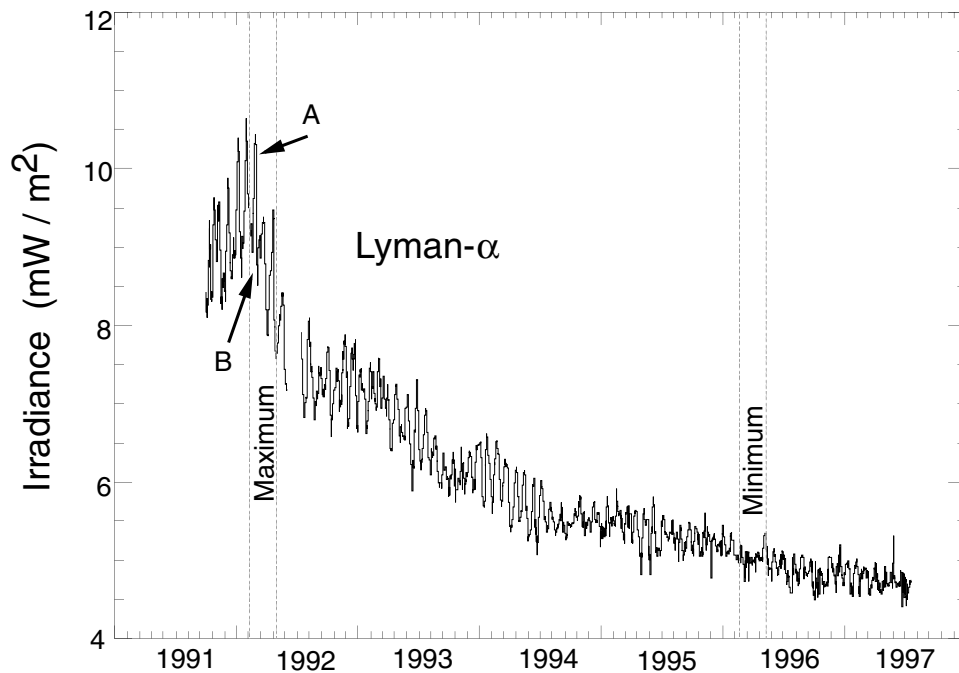
Figure 28: Time series of Lyman α solar irradiance; October 1991 through June 1997. Periods of maximum and minimum as discussed in section A.1.2 and A.1.3 are indicated.

A.1.2 27-day variations

The intermediate frequencies apparent in the time series of Figure 28 often have a period near 27-days, the solar rotation period. As areas of enhanced magnetic activity appear and disappear on the solar disk, they serve as "search lights" beamed by the slow rotation of the Sun. The observed 27-day variation therefore arises from two factors, first the rotation of the Sun and second, the non-uniform distribution of activity on the solar disk. For if activity is uniformly distributed, the mean irradiance level may be high, but the 27-day signal will be small. The amplitude of the 27-day signal therefore varies considerably throughout the solar cycle, and in fact there can be no single measure of its magnitude. Figure 29 provides as a function of wavelength a typical measure of the percent variation, (maximum / minimum -1), where the maximum and minimum are identified as "A" and "B" in Figure 28.

The wavelength-dependence of the 27-day variation seen in Figure 28 is fairly characteristic, strongest at the shortest wavelengths near 120 nm where the emission originates at the higher layers of the solar atmosphere and steadily decreasing toward longer wavelengths as the emission levels move lower and lower

down to the photosphere. Certain emission features, for example the Mg II (singly ionized magnesium) emission near 280 nm, have a source region higher in the chromosphere and display a variation consistent with these higher levels of the solar atmosphere. The variation in the core of this line is especially noticeable when compared to the variation of the nearby photospheric emission, at say 275 nm.

Selecting a solar rotation other than "A - B" in Figure 28 may have provided a similar variation, with the same general shape as Figure 29 but with a larger or smaller amplitude. Subtle differences in the spectral shape of such curves are being studied, for they would indicate differences in the behavior of the emission from the various layers of the solar atmosphere. Note the fact that the variation drops precipitously moving from short to long wavelength across the absorption edge of neutral aluminum at 208 nm. The details of how the amplitude of this variation relates to the variation at other wavelengths, for example to the Mg II lines at 280 nm, are paramount to the development of proxy models for solar activity.
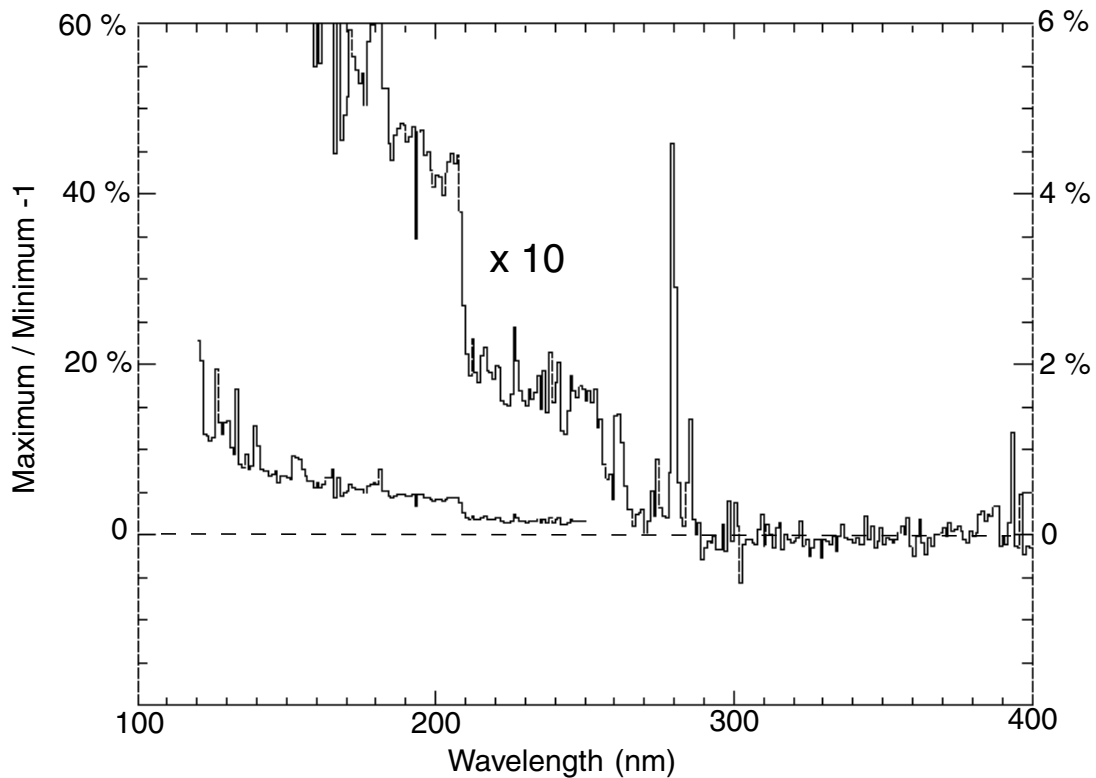
Figure 29: Intermediate term solar variations: The ratio of the solar spectrum for active day "A" in Figure 28 divided by the spectrum for less active day "B". This ratio illustrates the spectral shape for the 27-day variation, but only for this particular solar rotation. The scale at the left applies to the shorter wavelengths and the scale at the right applies to the longer wavelengths where the ratio has been amplified by a factor of 10.

A.1.3 Solar Cycle Variation

The two UARS instruments have made daily observations of the Sun from late in 1991 through the present time. To the extent that the early UARS measurements were representative of solar maximum conditions, the two instruments now provide independent records of the decrease from solar maximum to solar minimum. The Sun displayed little activity from the middle of 1996 through the end of that year, and values of ultraviolet irradiance taken from this quiet period satisfy the requirements of a "solar minimum" value. Likewise the UARS measurements early in the mission, especially in early 1992, are probably adequate to represent "solar maximum" conditions [White *et al.*, 1994]. These high values could be extrapolated back through the years 1990 and 1991 using one of the proxies of solar activity, for example

the Mg II index or the He 1083 nm emission, in order to achieve somewhat higher "solar maximum" values [Floyd *et al.* 1998].

The ratio presented in Figure 30 is obtained from the UARS SOLSTICE data and is the time average of 81 days (three solar rotations) spanning the period marked "maximum" in Figure 29 to a similar average over the period marked "minimum". During this four year period the relative accuracy of the UARS SOLSTICE data set is presently no better than ± 2%, although on-going refinements to the data processing and calibration algorithms may eventually improve the ratio uncertainty to ± 1%. Additionally, the ratios of Figure 30 have been smoothed to an effective spectral resolution of 5 nm in order to remove wavelength anomalies in this preliminary UARS SOLSTICE data analysis.
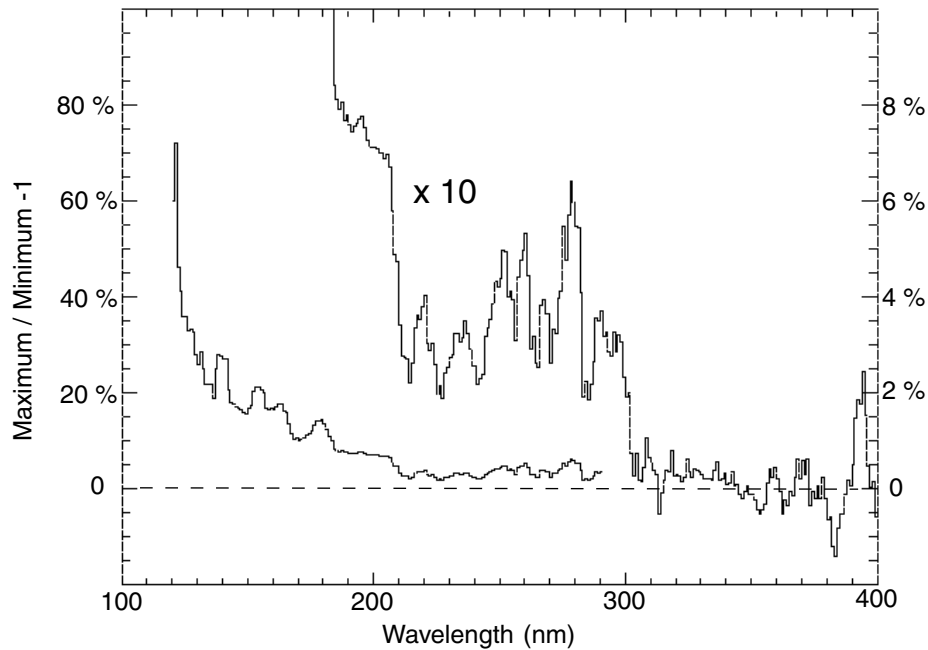
Figure 30: Solar cycle variation: The ratio of the solar spectrum from the "maximum" period of Figure 29 divided by the spectrum for the minimum period. These are preliminary estimates of the solar cycle variation and the noise in the ratio together with the measurement uncertainty is on the order of ±2%. Similar to Figure 29, the scale at the left applies to the short wavelengths and the scale at the right applies to ratio at longer wavelengths that have been amplified by a factor of 10.

These preliminary estimates from UARS SOLSTICE are in basic agreement with corresponding SUSIM values [Floyd *et al.*, 1997]. Likewise the four SSBUV observations [Cebula and Hilsenrath, 1996] deployed during the UARS mission provide an additional and independent set of measurements of solar cycle variation. In fact, three additional SSBUV flights (1989,1990, and 1991) extend this important data set back earlier into the maximum of solar cycle 22. The two UARS observations together with the SSBUV observations are presently being verified and a validation of all three will soon be completed. The measurement of the solar cycle variation from three independent instruments will increase confidence and understanding of longer-term solar variations.

Taking Figure 30 at face value, certain similarities with the 27-day rotational variation of Figure 29 are quite apparent. The solar cycle variation is strongest at the shortest wavelengths — just as it is with the rotational modulation, decreasing toward longer wavelengths and showing generally greater variation in the chromospheric emission lines. Once again a striking decrease in variability is seen moving from shorter to longer wavelengths across the aluminum edge at 208 nm. Because of the inherent uncertainty in the relative accuracy of the UARS SOLSTICE measurements (± 2% for the present analysis), there is questionable value in the data of Figure 30 longward of 300 nm.

Appendix B   Data Product Requirements and Descriptions

B.1 Overview

The SORCE program will produce two principal science data products for delivery to ECS: Total Solar Irradiance (TSI) data and Solar Spectral Irradiance data. Each of these two science data types will be delivered in both a daily average and a 6-hourly average version. The Spectral Solar Irradiance product will consist of daily and 6-hourly values for each mission day on which data are collected, resulting in two data files per mission day. Delivery will occur daily and the size of each delivered data granule will remain constant throughout the mission. The Total Solar Irradiance (TSI) data will similarly be delivered as daily and 6-hourly averages; however, due to the exceedingly small size of the daily data and to maximize ease of use of end users, each delivered TSI product will contain science results for the entire mission. Updates to TSI data will occur monthly in order to reduce repeated delivery of data. For TSI data, reprocessing will produce a single file that contains data for the entire mission and will be delivered once at the completion of a reprocessing activity. Each SORCE data deliverable and estimated data volumes are presented in Table 25.

In addition to the science products and their metadata, the SORCE project will also deliver mission level 0 data since LASP also serves as the operations center and data capture facility for the SORCE spacecraft. Metadata for the level 0 data will also be delivered, as will quality metadata for the science products.

Table 25: SORCE Standard Data Products

Description	Transfer Frequency
Total Solar Irradiance data (daily averages)	Monthly
Total Solar Irradiance data (6-hourly averages)	Monthly
Solar Spectral Irradiance Data (daily averages)	Daily
Solar Spectral Irradiance Data (6-hourly averages)	Daily

Level 0 data transfer will commence shortly after launch and will take place once per calendar day. Level 0 data for any given mission day will be transferred to the GSFC DAAC nominally only once during the mission as new versions need not be produced. Reprocessing efforts at LASP will not result in re-transmission of Level 0 data. Roughly 10-20 Level 0 and metadata files will be transferred each mission day, following all spacecraft contacts. More frequent transfers will be required during the early-orbit checkout and activation period, but should not exceed the estimated daily volume of 120MB. Spacecraft and Instrument Level 0 data and metadata will be prepared for delivery in a format described in the ESDIS to SORCE ICD.

Transfer of the Standard Science Data Products will commence after the NASA-approved post-launch measurement calibration and algorithm testing period, after which deliveries will take place daily. As discussed in Appendix C, delivered data will lag the actual observation times by perhaps three months while in-flight measurement calibration data are gathered and processed. The first science data delivery will occur approximately four months into the mission, after instrument activation, with subsequent daily transfers. Data reprocessing will be required from time to time which will generate new versions of the standard science data product for delivery to EOSDIS.

Data will be distributed to local users directly from the SORCE project database, and to general users via the DAAC and a locally maintained WWW interface.

B.1.1 SORCE Data Level Definitions

The SORCE science data system will generate data that conform to the following classifications. Level 3 products will be made available to the public via a WWW interface maintained at LASP and via the NASA GSFC DAAC. As part of the routine daily production processing, a preliminary degradation correction based upon extrapolation of historical degradation analysis is applied to Level 3 data. Although released daily, these Level 3 data will be considered provisional until time-dependent corrections and calibrations are derived from in-flight measurements and applied to the data.

Level 0   Reconstructed, unprocessed instrument/payload data at full resolution; any and all communications artifacts, e.g., synchronization frames, communications headers, duplicate data removed.

Level 1A   Unprocessed instrument data at full resolution, time-referenced, sorted by experiment and/or data type.

Level 1B   All processed ancillary information required for conversion into physical units, including calibration coefficients, georeferencing parameters (e.g., platform ephemeris)

Level 2   Sorted instrument data (level 1A) processed into physical units with all applicable conversions and calibrations (level 1B) applied.

Level 3A   Processed instrument data, time-averaged and spectrally resampled onto a uniform wavelength scale; time-dependent corrections that require empirical models are not applied.

Level 3B   Processed instrument data, time-averaged and spectrally resampled onto a uniform wavelength scale; with time-dependent corrections that require empirical models applied.

B.2 Level 2 Products

B.2.1 Solar Irradiance

The solar product produced by the production software at Level 2 represents the lowest level of scientifically useful data. All calibration parameters and other factors are applied to the data at this step, providing irradiances at full time and instrument spectral resolution.

B.2.2 Stellar Irradiance

In the case of SOLSTICE instruments, the stellar data provide the primary mechanism for monitoring changes in instrument sensitivity vs. time during flight. Each stellar observation will be perhaps a few minutes in length to provide adequate counting statistics for precise degradation monitoring. Nominally, each stellar observation will consist of up to several hundred samples for a single wavelength and target, timetagged individually. Each of these individual samples is calibrated to irradiance units and associated

with its appropriate wavelength. These stellar data are distinguished from the solar data and stored along with relevant pointing, housekeeping, and geographical information.

B.3   Level 3 Products

The standard data product produced by the SORCE project consists of full-disk solar irradiances reported on a standard wavelength scale and averaged to one spectrum every 6 hours. In addition to this product, however, several lower-level products are produced by the processing software as research and validation items, but are not generally released to the public.

B.3.1   Solar Irradiance at standard resolution (4/day)

This is the standard data product that will be available to the general public on the project WWW site and distributed to a NASA DAAC. It consists of four solar spectra per calendar day and integrated to a standard wavelength scale. The standard wavelength scale will range in resolution from 1 nm bins to 10 nm or more over the entire solar spectrum, depending upon the baseline resolution of the instrument used to construct that spectral interval. In addition to spectral data, this product will also include total solar irradiance measurements given on 6-hourly averages (4/day).

B.3.2   Solar Irradiance at full instrument resolution (4/day)

In order to construct the standard data product, two basic steps must occur: averaging the multiple daily measurements in time and combining them in the spectral dimension. Prior to resampling the spectral data onto a lower-resolution wavelength scale, the multiple daily measurements are first averaged in time to produce four high-resolution spectra per day. These data are preserved in the project database - in addition to the standard data product - for further analysis and to provide further insight into the data.

B.3.3   Fixed-Wavelength Stellar Irradiances

For use in constructing models of instrument degradation, the multi-sample data from each stellar experiment are time-averaged to give a single representative irradiance value at the observed wavelength. These averaged data points provide a more manageable long-term data volume for use in subsequent degradation analyses.

B.3.4   Stellar Spectral Irradiances

Full spectral measurements of selected stars will be performed. Although on-orbit observing constraints and instrument performance characteristics will inevitably limit the counting statistics and spectral resolution of such measurements, they will nevertheless be observed for analysis purposes and comparison with other astronomical measurements.

B.3.5   Solar Emission Lines

Selected UV spectral (emission) lines are extracted, either by fitting a Gaussian multiplet plus a background (continuum) model to the appropriate ensemble of Level 2 data, or by integrating the Level 3 spectral b-spline model under the emission. For the non-linear Gaussian fits a robust implementation [Moré *et al*., 1980] of the Levenberg-Marquardt non-linear least-squares algorithm is used. The b-spline spectral model follows the data better than a Gaussian does when there are blends from other species, but requires a somewhat more sophisticated background (continuum) model. In either case, the emission line product consists of fitting parameters and uncertainties (for perhaps multiple Gaussians per line), line centers and widths, and integrated intensities of both the line emissions and the background. The number of selected lines is small (< 20), as is the total amount of data per line.

B.3.6 Solar Absorption Line Core/Wing Ratios

The Mg-II (279.6 nm) and Ca-II (393.4, 396.8) Fraunhofer K- and H-self-absorption lines are analyzed to form core/wing ratios which are measures of chromospheric activity which are relatively free of systematic uncertainty such as the instrument degradation function [White and Livingston, 1978; Heath and Schlesinger, 1986]. These core/wing ratios are computed from the daily (or 6-hourly) b-spline spectral model, by integrating under the core emission and under neighboring background points over a bandwidth comparable to the SORCE SOLSTICE slit function width, then dividing the core integral by the wing integral, resulting in a dimensionless ratio. These core/wing ratios, as well as positions, widths, and amplitudes and uncertainties and fill fractions are all stored in the core/wing ratio product. Like the emission line extractions, this is a small product.

Appendix C   Science Data Production

C.1 Overview

All science data production and management activities are provided by the LASP SORCE Science Data System, which resides at LASP in Boulder, Colorado.   The SORCE Science Data System consists of both the hardware and software components necessary to capture, manage, process, analyze, validate, and distribute all science data products.

At the core of the system resides a commercial relational database system, in which all telemetry, calibration data, scientific data products, and ancillary information are stored. All data are stored in the database as individual time-referenced points to provide direct and rapid access to each datum received from the spacecraft or instruments or subsequently processed.   Certain file cataloging and archiving activities are also required to manage these data, for instance, design documentation and raw telemetry data as received from the ground stations following spacecraft contacts. However, file cataloging will generally not be employed for data management.

The data processing and calibration data management software are tightly coupled with the SORCE project database, in which all data sources and products are stored. The data processing component of the system interacts directly with the time-referenced data as stored in the database in order to provide efficient data utilization. With this technique employed, processing steps will not produce science product data *files*, but rather store each science datum in one or more normalized database tables, along with all metadata necessary to provide complete traceability to any dependent data sources and software versions.

C.2 Data Management

All project data will be managed within a commercial relational database management system (DBMS). This system will maintain, under configuration control, all software, raw instrument and spacecraft data, engineering data products, science data products, calibration data, operations plans, ancillary data, instrument loads, etc. This system will also establish and maintain audit trails making all data products traceable to the original source code, operation plans, calibration data, and other relevant information. Data security will be maintained using standard firewall and system security techniques, while integrity will be guaranteed by employing backup/recovery capabilities and utilizing automated sweep systems that are built into modern commercial DBMS products.

C.3 Data Processing

The SORCE Science Operations Center has full responsibility for all science data production activities. Data processing is performed automatically with the production of data through Level 3 occurring in less than 24 hours from the time of data reception and a *preview* release available to the public within 48 hours following preliminary data inspection. Appropriate corrections for some time-dependent processes (such as instrument degradation correction) will require in-flight calibration data several months into the future, so that the daily production of science products beyond preview quality will lag by a period of several months. This will result in two streams of data being created on a daily basis: the provisional stream of preview data that are available within 48 hours, and a second stream of data that supercede the preview data a few months after the preview release.   Provisional data will not be released to EOSDIS, as recommended by the SORCE Algorithm Theoretical Basis Document (ATBD) review panel, since they are not fully calibrated and provide limited use to the scientific community.   These data will, however, be made available informally from the SORCE mission web page. Approximately three months after SORCE launch, following the instrument checkout period, sufficient data will have been obtained to begin generating higher-quality data products.   These data will be used to generate products in HDF format that are distributed to EOSDIS, therefore the DAAC will not receive SORCE data products until several months

after initial data reception. The quality level of the data, as well as other associated metadata, will be attached to all data.

Note that the lead time required for time-dependent gain and degradation corrections will in each case be sufficient so that re-fittings of the model parameters at appropriate time intervals (using the same model algorithm version) will not result in significant changes to existing model coefficients or previously-released non-preview data values.

For example, a time-dependent model might be implemented by a spline, with a node spacing of 3 months. At three-month intervals an additional node is added and the spline coefficients are re-fit, but the values of the existing coefficients (and model evaluations) do not change. During the three months since the last model was fit, the model is extrapolated to get values with which to compute corrections for the *preview* data product, and the only data values which change after a new node is added and the model re-calculated are these *preview* values.

Other functional types may be employed (exponentials, polynomials) but in each case the model is only recalculated (re-fit) when there is sufficient lead time so that the model values used for previously-released data do not change significantly (the differences, if any, are guaranteed to be in the noise).

During the first year or two of the mission, SORCE project personnel will work to define these models, and it is likely that model *definitions* (versions) will be changed during this time, and each such change will require reprocessing and a revised (new) version of the released data, but this only occurs with a changed model definition, not with every fitting of model parameters.

Science data processing software is tightly coupled with the SORCE project database at LASP and implemented in a variety of programming languages, including FORTRAN, Java, C, and csh and Perl scripts. Software developed for the SORCE mission will conform to accepted software coding standards and best practices. All software will be configuration managed at the SORCE SOC using a commercial configuration management system and versions and configurations will be traceable to each produced datum. Processing and management of data will take place on a multiprocessor Solaris-based server provided by Sun Microsystems using science data processing algorithms described in this Algorithm Theoretical Basis Document (ATBD).

The SORCE data production system will execute in an event-driven fashion by which state changes of selected data products in the data management system will initiate subsequent processing steps. Software objects will be developed using the Java programming language with many Java methods implemented in other languages, such as C or FORTRAN. This permits reuse of legacy code from other projects and improves overall system performance by utilizing the appropriate programming language for each particular task. Java's inherent multi-threaded capabilities will provide support for multi-processor machines.

The Science Data System provides full and partial mission reprocessing capability, supporting the SORCE mission requirement to complete full mission reprocessing in less than one calendar month. Reprocessed data will therefore be generated at up to a 100x rate, will be inspected and released to EOSDIS, superceding previous data versions.

Targets of opportunity, such as comets, occultations, lunar, and planetary observations, will not be included as part of the SORCE data products delivered to the DAAC.

C.4 Quality Assurance

The SORCE scientific data processing system employs modern object oriented design technology, following an incremental and evolutionary development lifecycle. SORCE utilizes various software development tools to minimize risk from programming errors, bugs, or other anomalies. In particular, object modeling standards and tools as well as code analyzers are used to inspect code for problems that may otherwise remain undiscovered. Defect tracking and configuration management tools are also used.

Preliminary data quality assessment will be accomplished by building high-level trend and limit checking into the data production software. Long- and short-term trends will undergo comparison with predicted values, and data will be identified in processing logs if any limits are violated. These trends and processing logs are reported automatically to data production staff for inspection. Such inspection will result in data either being released or investigated further prior to release. During subsequent and more rigorous validation, applied calibrations are scrutinized, data are compared with other instruments (when possible) and theoretical predictions, and changes in instrument sensitivity are analyzed. Once validated, quality metadata are updated or data are re-released and distributed to EOSDIS for archival.

C.5 Data Flow

Deliveries of Level 0 data to the SOC will occur at arbitrary times and consist of arbitrary numbers of un-ordered telemetry packets. The Level 0 ingest process will be triggered by these deliveries, and will consist of unpacking and decommutating telemetry frames, quality and limits checking, and population of Level 0 data tables.

It is expected that the delivery and ingest of all definitive Level 0 data (science, engineering, orbit, attitude, ephemeris) for a given calendar day will have been completed within 6 hours after the end of that day.

At regular intervals (6 hours or 24 hours), the processing of all Level 1 through Level 3 science products from recently completed intervals of Level 0 ingests will take place. Science processing is fully parameterized and configurable (to specify data versions, calibration set versions, operational acceptance criteria, etc.), and these science processing metadata configuration specifications are themselves inserted into the central data store.

It is anticipated that full science processing for one 6-hour or 24-hour interval will require just a few minutes (1 to 10) of CPU time, so that all science products, with provisional corrections for time-dependent systematic uncertainties, will be available almost as soon as all of the Level 0 data have been received. Definitive corrections for some time-dependent processes (such as the stellar-derived detector degradation correction) may require in-flight calibration data several months into the future, so that the daily production of definitive science products may lag behind the current date by a period of several months.

A mission requirement is that a full mission reprocessing from Level 0 to Level 3 should require less than one calendar month. For example, when the mission is 3000 days old, this requirement says that science processing must run at a rate of 100 days per day, or better. This is essentially a hardware requirement, and presently available (1998) hardware (let alone that which will be available when the mission is 3000 days old) should easily meet this requirement.

C.6 Storage Considerations

A mission requirement is that all data of current or active versions for the entire mission be kept "on-line" for rapid access (e.g., on magnetic as opposed to optical disk media). It is expected that the COTS RDBMS will support automatic demotion to "off-line" media (e.g., optical disk) of non-current or superseded data versions. The daily data volume of all science and engineering products is in the neighborhood of 200 MB, so the on-line requirement implies a magnetic disk storage capacity of about 600 GB for a 3000-day mission.

C.7 Data Structure

The SORCE data management and distribution philosophy distinguishes between the internal ("private") fully-normalized database table structure and the external ("public") views of the science data supported by the access services. These need not be the same. The internal database tables will be fully normalized and the structures designed for ease of maintenance, maximum data integrity, and optimal performance. The

public data structures and the data services interfaces will be standardized and as stable as possible, and designed for appropriate scientific "views".

C.8 Software Configuration Management

A software configuration (version) control system (e.g., RCS, ECS, or the COTS product "Razor") will be used for all production software (that is, software which inserts data into the data store). Also, the configuration management system will be used to create a manifest of the software versions that comprise each software build. These manifests will be stored in the database and will be used in the establishment of science product "pedigrees" (next item).

C.9 Data Configuration Management

All data (calibration data, production parameters, intermediate data, and final science data) will be under configuration control. That is, each "row" of data in the data store will be linked (e.g., by foreign keys) to other data on which it depends or from which it is derived. For example, each production "job" will have all of its parameters stored (e.g., in a "production job" table) with a unique identifier (key), and each row of data produced by this production job will refer to this production job, so that the production parameters for those data are known.

Moreover, the software algorithms themselves are under the same configuration control. That is, for each software "build" there will be an entry in a database table storing the relevant attributes of the software build (version, algorithm configuration, compiler settings, etc.) along with the source code manifest supplied by the software CMS.

The intent of this configuration management design is that the data store contain all of the relevant "metadata" about any row of data, so that, at least in theory, any row of data could be reproduced at any time in the future, using the same algorithm versions, production parameters, and input data as were originally used.

Appendix D   Acronyms

ADC	Analog to Digital Converter
API	Application Programming Interface
ATBD	Algorithm Theoretical Basis Document
BDRF	Bidirectional Reflectance Function
CCD	Charge Coupled Device
COTS	Commercial off-the-shelf
CU	University of Colorado, Boulder
DAAC	Distributed Active Archive Center
DAC	Digital to Analog Converter
DBMS	Database Management System
DSP	Digital Signal Processor
EOS	Earth Observing System
ESR	Electrical Substitution Radiometer
EUV	Extreme Ultraviolet
FUV	Far Ultraviolet
HRT	Hard Radiation Trap (SIM instrument)
LASP	Laboratory for Atmospheric and Space Physics
LOWTRAN	Low Resolution Transmission Model
MOC	Mission Operations Center
MUV	Middle Ultraviolet
NIST	National Institute for Standards and Technology
ppb	Parts per Billion
ppm	Parts per Million (10,000ppm = 1%, 0.01%=100ppm)
PWM	Pulse-width Modulation
RDBMS	Relational DBMS
SEE	Solar EUV Experiment
SIM	Spectral Irradiance Monitor
SNOE	Student Nitric Oxide Explorer
SOC	Science Operations Center
SOLSTICE	Solar Stellar Irradiance Comparison Experiment
SORCE	Solar Radiation and Climate Experiment
SQL	Structured Query Language
SURF	Synchrotron Ultraviolet Radiation Facility
SZA	Solar Zenith Angle
TIM	Total Irradiance Monitor
TIMED	Thermosphere Ionosphere Mesosphere Energetics and Dynamics
UARS	Upper Atmosphere Research Satellite
UV	Ultraviolet
XPS	XUV Photometer System
XUV	X-Ray Ultraviolet (Soft X-rays)

References

Bailey, S. M., T. N. Woods, L. R. Canfield, R. Korde, C. A. Barth, S. C. Solomon, and G. J. Rottman, Sounding rocket measurements of the solar soft x-ray irradiance, *Solar Physics*, 186, 243-257, 1999.

Bless, R. C., A. D. Code, and E. T. Fairchild, Ultraviolet photometry from the Orbiting Astronomical Observatory. XXI. Absolute energy distribution of stars in the ultraviolet, *Ap. J.* 203, 410-416, 1976.

Bohlin, R. C., A. V. Holm, B. D. Savage, M. A. J. Snijders, and W. M. Sparks, Photometric calibration of the International Ultraviolet Explorer (IUE): Low Dispersion, *Astr. Ap.* 85, 1-13, 1980.

Bohlin, R. C., D. Frimout, and C. F. Lillie, Absolute flux measurements in the rocket ultraviolet, *Astr. Ap.* 30, 127-134, 1974.

Bretagnon, P & Francou, G. Planetary theories in rectangular and spherical variables. VSOP87 solutions. *Astron. Astrophys.* v. 202, pp. 309-315, 1988.

Brueckner, G.E., K.L. Edlow, L.E. Floyd, J.L. Lean, and M.E. VanHoosier, The Solar Ultraviolet Spectral Irradiance Monitor (SUSIM) Experiment on Board the Upper Atmospheric Research Satellite (UARS), *J. Geophys. Res.*, 98, 10695-10711, 1993.

Brune, W. H., G. H. Mount, and P. D. Feldman, Vacuum ultraviolet spectrophotometry and effective temperatures of hot stars, *Ap. J.* 227, 884-899, 1979.

Canfield, L. R., J. Kerner and R. Korde, "Stability and quantum efficiency performance of silicon photodiode detectors in the far ultraviolet", *Applied Optics*, 28, 3940, 1989.

Canfield, L. R., R. Vest, T. N. Woods, and R. Korde, "Silicon photodiodes with integrated thin film filters for selective bandpasses in the extreme ultraviolet", SPIE Proceedings, 2282, 1994.

Carruthers, G. R., H. M. Heckathorn, and C. B. Opal, Far-ultraviolet spectra and flux distributions of some orion stars, *Ap. J.* 243, 855-873, 1981.

Cebula, R. P. and E. Hilsenrath, SSBUV Measurements of Solar Spectral Irradiance Variations, 1989 - 1996, *EOS Trans. Amer. Geophys. Union,* 77(46), Fall Meet. Suppl., 579, 1996.

Cebula, R.P., E. Hilsenrath, and M.T. DeLand, Middle ultraviolet solar spectral irradiance measurements, 1985-1992, from the SBUV/2 and the SSBUV instruments, in The Sun as a Variable Star, J.M. Pap, C. Fröhlich, H.S. Hudson, and S.K. Solanki, eds., Cambridge University Press, pp. 81-88, 1994.

Chapman, G.A., A.M. Cookson, and J.J. Dobias, 1996, "Variations in the Total Solar Irradiance During Solar Cycle 22", *JGR*, **101**,A6, 13541-13548.

Cleveland, William S., The Elements of Graphing Data, Wadsworth Advanced Books, Monterey, CA, 1985

de Boor, Carl. A Practical Guide to Splines. Springer-Verlag, New York, 1978.

Edlen, B., J. Opt. Soc. Amer.43, 339, 1953

Féry, C, *Comptes Rendus*, 150, 216, 1910

Floyd, L.E., P.A. Reiser, P.C. Crane, L.C. Herring, D.K. Prinz, and G.E. Brueckner, SUSIM UARS measurements of solar cycle 22 UV irradiance variability, *Solar Physics*, 177, 79-87, 1998.

Fröhlich, C., and the VIRGO team: 1996, "First Results from the VIRGO Experiment, *Transactions AGU*, Spring Meeting.

Fröhlich, C., 1994, *The Sun as a Variable Star*, eds.: J. Pap, C. Fröhlich, H. Hudson, and S. Solanki, Cambridge Univ. Press, New York, pp, 28-36.

Fröhlich, C. and J. Lean, "The Sun's Total Irradiance: Cycles, Trends and Related Climate Change Uncertainties since 1976", *J. Geophys. Res.*, 25, 23, 4377-4380,1998

Hansen, J.E., A. Lacis, D. Rind, G. Russell, P. Stone, I. Fung, R. Ruedy, and J. Lerner, 1994, "Climate Sensitivity: analysis of feedback mechanisms" in Climate Processes and Climate Sensitivity, J. Hansen and T. Takahashi (eds.), American Geophysical Union, Wash., D.C.

Harder, J.W., G. Lawrence, G. Rottman, and T. Woods, The Solar Spectral Irradiance Monitor: SIM, *Metrologia*, in press 2000

Harvey, K., A. Mustico, and J. Vallimont, *Proc. SPIE*, 1761, 2-13, 1992

Heath, D.F. and B.M. Schlesinger, JGR 91, 8672-8682, 1986.

Hengstberger, F., in Absolute Radiometry: Electrically Calibrated Thermal Detectors of Optical Radiation, Edited by F. Hengstberger, Academic Press Inc., San Diego, CA, 1989

Henry, R. C., A. Weinstein, P. D. Feldman, W. G. Fastie, and H. W. Moos, Low-resolution ultraviolet spectroscopy of several hot stars observed from Apollo 17, Ap. J. 201, 613-623, 1975.

Hickey, J., B. Alton, H. Kyle, and E. Major, Solar Irradiance Measurement by Nimbus-7 ERB Experiment: an Update of 100 Months, in *Solar Radiative Output Variation*, P. Foukal, ed., p. 189, 1987

Holberg, J. B., W. T. Forrester, and D. E. Shemansky, Voyager absolute far-ultraviolet spectrophotometry of hot stars, Ap. J. 257, 656-671, 1982.

Jamar, C., D. Macau-Hercot, A. Monfils, G. I. Thompson, L. Houziaux, and R. Wilson, Ultraviolet Bright Star Spectrophotometric Catalogue, ESA SR-27, 1976.

Johnson, C. E., "Ultra-Black Coating Due to Surface Morphology", U.S. Patent No. 4233107, Nov 11, 1980

Kiehl, J., and K. Trenberth, 1997, "Earth's Annual Global Mean Energy Budget", *Bull. Amer Meteor. Soc.,* **78**, 197-208.

Korde, R. and L. R. Canfield, "Silicon photodiodes with stable, near theoretical quantum efficiency in the soft x-ray region", SPIE Proceeding, 1140, 126, 1989.

Korde, R., L. R. Canfield, and B Wallis, "Stable high quantum efficiency silicon photodiodes for vacuum ultraviolet applications, SPIE Proceeding, 932, 153, 1988.

Korde, R. and J. Geist, "Quantum efficiency stability of silicon photodiodes", Applied Optics, 26, 5284, 1987.

Kurucz, R. L., I. Furenlid, J. Brault, L. Testerman, Solar Flux Atlas from 296 to 1300 nm, National Solar Observatory Atlas, Sunspot, New Mexico: National Solar Observatory, 1984

Kyle, H.L., D.V. Hoyt, J.R. Hickey, R.H. Maschoff, and G.J. Vallette, 1993, "Nimbus-7 Earth Radiation Budget Calibration History - Part 1: The solar channels", *NASA Reference Publication 1316.*

Lawrence, G. M., G. Rottman , J. Harder, T. Woods, The solar Total Irradiance Monitor: TIM, Metrologia, 2000, in press.

Lawrence, G. M., J. Harder, G. Rottman, T. Woods, J. Richardson, G. Mount, "Stability considerations for a solar Spectral Intensity Monitor (SIM)", SPIE Conference on Long-Term Degradation of Optical Systems, San Diego, CA, SPIE Vol. 3427, 1998

Lawson, Charles L., and Hanson, Richard J. Solving Least Squares Problems (esp. chap. 27). Prentice-Hall, Englewood Cliffs, NJ, 1974

Lee, R.B., M.A. Gibson, R.S. Wilson, and S. Thimas, 1995, "Long-term total solar irradiance variability during sunspot cycle 22", *J. Geophys. Res.,* **100**, 1667-1675.

Macau-Hercot, D., C. Jamar, A. Monfils, G. I. Thompson, L. Houziaux, and R. Wilson, Supplement to the Ultraviolet Bright Star Spectrophotometric Catalogue, ESA SR-28, 1978.

Malitson, I. H., J. Opt. Soc. Amer., 55, 1205-1209, 1965

Mihalas, d., and J. Binney, Galactic Astronomy Structure and Kinematics, pp. 135-139, W. H. Freeman, New York, 1981

Moré, Jorge J., Gabow, Burton S., Hillstrom, Kenneth E., User Guide For Minpack-1, Argonne National Laboratory, Argonne, Ill., August 1980.

Powell, F. R., P. W. Vedder, J. F. Lindblom, S. F. Powell, "Thin film filter performance for extreme ultraviolet and x-ray applications", Optical Eng., 26, 614, 1990.

Rottman, G., G. Mount, G. Lawrence, T. Woods, J. Harder, S. Tournois, *Metrologia*, 35, 707-712, 1998

Rottman, G. J., T. N. Woods, "SOLSTICE technique for measuring long-term solar variability", Proc. SPIE Vol. 2583, p. 347-355, Advanced and Next-Generation Satellites, Hiroyuki Fujisada; Martin N. Sweeting; Eds., 1995

Rottman, G. J., T. N. Woods, and T. P. Sparn, SOLar STellar Irradiance Comparison Experiment I : 1. instrument design and operation, J. Geophys. Res., 98, 10,667-10,677, 1993.

Rottman, G.J., C.A. Barth, R.J. Thomas, G.H. Mount, G.M. Lawrence, D.W. Rusch, R.W. Sanders, G.E. Thomas and J. London, Solar Spectral Irradiance, 1200 to 1900Å, October 13, 1981 to January 3, 1982, *Geophys. Res. Letters*, 9, 587, 1982.

Solomon, S. C., C. A. Barth, P. Axelrad, S. M. Bailey, R. Brown, R. L. Davis, T. E. Holden, R. A. Kohnert, F. W. Lacy, M. T. McGrath, D. C. O'Connor, J. P. Perich, H. L. Reed, M. A. Salada, J. Simpson, J. M. Srinivasan, G. A. Stafford, S. R. Steg, G. A. Tate, J. C. Westfall, N. R. White, P. R. Withnell, and T. N. Woods, The Student Nitric Oxide Explorer, SPIE Proceedings, 2810, 121-132, 1996.

Standish, E.M., "Orientation of the JPL Ephemerides, DE200/LE200, to the Dynamical Equinox of J2000", Astronomy & Astrophysics, vol. 114, pp. 297-302, 1982

Standish, E.M., "The Observational Basis for JPL's DE200, the planetary ephemeris of the Astronomical Almanac", Astronomy & Astrophysics, vol. 233, pp. 252-271, 1990

Stronglyis, G. J. and R. C. Bohlin, Absolute calibration in the 1750 Å - 3350 Å region, Publ. Astron. Soc. of Pacific, 205-213, April 1979.

Tennyson, P.D., P. D. Feldman, and R. C. Henry, Search for ultraviolet shuttle glow, Adv. Space Res., 7, 207-210, 1987.

Thuillier, G., M. Herse, P. Simon, D. Labs, H. Mandel, and D. Gillotay, Observation of the UV Solar Spectral Irradiance between 200 and 360 nm during the ATLAS-1 Mission by the SOLSPEC Spectrometer, *Solar Physics,* 177, 41-61, 1998.

Tropf, W. J. and Thomas M. E., "Infared Refractive Index and Thermo-optic Coefficient Measurement at APL", APL Technical Digest, vol.19, number 3, 1998

VanHoosier, M, J. Bartoe, G. Brueckner, and D. Prinz, Absolute Solar Spectral Irradiance 120 nm – 400 nm (Results from the Solar Ultraviolet Spectral Irradiance Monitor –SUSIM-Experiment on Spacelab 2), *Astro. Lett. and Communications,* 27,, pp. 163-168, 1988.

Warren, D.W., J.A. Hackwell, and D.J. Gutierrez, Optical Engineering, 36, 1174-1182, 1997

White, O.R. and W. Livingston, ApJ, 226, 679-686, 1978.

White, O.R., G.J. Rottman, T.N. Woods, S.I. Keil, W.C. Livingston, K.F. Tapping, R.F. Donnelly, and L. Puga, Change in the UV Output of the Sun in 1992 and its Effect in the Thermosphere, *J.Geophys. Res.*, 99, 369-372, 1994.

Willson, R. C., 1997, "Total Solar Irradiance Trend in Solar Cycles 21 and 22", Science 277, 1963 - 1965.

Willson, R.C. , 1994, "Irradiance observations of SMM, Spacelab-1, UARS, and ATLAS Experiments", *The Sun as a Variable Star*, eds.: J. Pap, C. Fröhlich, H. Hudson, and S. Solanki, Cambridge Univ. Press, New York, pp, 54-62.

Willson, R C., Measurement of Solar Total Irradiance and its Variability, Space Sci. Rev., 38, 203-242, 1984

Woods, T. N., G. J. Rottman, S. M. Bailey, S. C. Solomon, and J. Worden, Solar extreme ultraviolet irradiance measurements during solar cycle 22, Solar Physics, 177, 133-146, 1998a.

Woods, T. N., F. G. Eparvier, S. M. Bailey, S. C. Solomon, G. J. Rottman, G. M. Lawrence, R. G. Roble, O. R. White, J. Lean, and W. K. Tobiska, TIMED Solar EUV Experiment, SPIE Proceedings, 3442, 180-191, 1998b.

Woods, T. N., D. K. Prinz, J. London, G. J. Rottman, P. C. Crane, R. P. Cebula, E. Hilsenrath, G. E. Brueckner, M. D. Andrews, O. R. White, M. E. VanHoosier, L. E. Floyd, L. C. Herring, B. G. Knapp, C. K. Pankratz, and P. A. Reiser, Validation of the UARS solar ultraviolet irradiances: Comparison with the ATLAS 1 and 2 measurements, J. Geophys. Res., 101, 9541-9569, 1996.

Woods, T. N., R. T. Wrigley, G. J. Rottman and R. E. Haring, "Scattered light properties of diffraction gratings", Applied Optics, 33, 4273-4285, 1994.

Woods, T.N., G.J. Rottman, and G. Ucker, Solar Stellar Irradiance Comparison Experiment I: 2 Instrument Calibration, *J. Geophys. Res*., 98, 10,679-10,694,1993.

Woods, T. N. and G. J. Rottman, Solar EUV irradiance derived from a sounding rocket experiment on 10 November 1988, J. Geophys. Res. 95, 6227-6236, 1990.

Woods, T. N., P. D. Feldman, and G. H. Bruner, The absolute flux of six hot stars in the ultraviolet (912-1600 Å), Ap. J. 292, 676-686, 1985.